

REDUCTION OF NOISE DUE TO TASK CORRELATED MOTION IN EVENT
RELATED OVERT WORD GENERATION FUNCTIONAL MAGNETIC
RESONANCE IMAGING PARADIGMS

By

KAUNDINYA S. GOPINATH

A DISSERTATION PRESENTED TO THE GRADUATE SCHOOL
OF THE UNIVERSITY OF FLORIDA IN PARTIAL FULFILLMENT
OF THE REQUIREMENTS FOR THE DEGREE OF
DOCTOR OF PHILOSOPHY

UNIVERSITY OF FLORIDA

2003

Copyright 2003

by

Kaundinya S. Gopinath

There are more things in heaven and earth Horatio, Than are dreamt of in your philosophy.

-William Shakespeare, in Hamlet: Act 1, Scene 5

ACKNOWLEDGMENTS

This work would not have been possible without the active help and blessings of a number of people. Firstly, I would like to acknowledge my advisor, Dr. Richard Briggs, for his constant support and encouragement throughout the duration of my Ph.D. Dr. Briggs introduced me to the concepts of magnetic resonance imaging and functional MRI. I remember, like it was just yesterday, how he explained the concepts of relaxation and MR signal detection in the lab on the tenth floor of the dental sciences building. Dr. Briggs has always impressed me by his tremendous insights into MR physics. He has the ability to explain recondite concepts in concise layman's terms, which helped me greatly in my learning process. Dr. Briggs gave me freedom to go explore the world of MR, a field that amazes me with its scope and potential everyday. I remember, early in my first years with the group, how I used to come back from the library or some other place flush with excitement at some "new" idea I had or some "new" application of MR I had just encountered in some journal, and when I told Dr. Briggs he would give me more insight into the "new" idea or application, give me a few papers on it and even sometimes have some stories about some of the early MR personnel who had worked on it. I realized quickly that it was not easy to surprise him with a MR "discovery." Apart from his academic influences, Dr. Briggs and Mrs. Dorothy Briggs have always been warm and generous and I enjoyed all the times when I had the occasion to mingle with them socially.

I would like to acknowledge Dr. Bruce Crosson's help in my education in FMRI. Dr. Crosson has an encyclopedic knowledge of brain function and anatomy and it always amazes me how he is able to describe the name and function of any obscure (to me) gyrus or sulcus one points to in the brain. Dr. Crosson always impressed me by his 'problem-solving' approach of attacking FMRI issues. Whenever I have a discussion with him regarding data analysis and FMRI, I seem to come away with a new insight into the issue I have been discussing with him. Dr. Crosson has always been generous with his support and encouragement for my work. Dr. Crosson constantly impresses me with his energy and drive. It seems just as easy to come upon him at work at 1am at night or 8am in the morning. Also I have always enjoyed the parties at Dr. Crosson's place. There is always something interesting happening when we have a function at his place.

I would like to acknowledge the help Dr. Wesley Bolch provided in advancing my academic future. He took me into the department when my academic career was floundering after some lackluster years in the uninspiring Physics Department. I will eternally be indebted to him for giving me a second chance. In the future, I hope to live up to the trust he put in me. I enjoyed all the classes I took with Dr. Bolch. I was very impressed by his energy and attention to detail. I remember the marathon sessions he used to hold over the weekends going over the presentations of the whole class. At the end of these sessions, when everybody else seemed tired, he looked like he could go for a couple of sessions more. Dr. Bolch always has time for the students and his commitment to students' well-being is unstinting. I consider myself fortunate to be in his department.

I would also like to acknowledge my advisors Dr. David Hintenlang and Dr. John Harris. I have had the fortune to take some classes under Dr. Hintenlang and he always

impressed by the ease with which he taught. I remember sitting through his lectures and wondering at the easy pace only to look down at my work and see five or six pages of notes. And I always thought I did not take much notes. Dr. Hintenlang has the knack of relating recondite concepts (in say radiation shielding) to everyday events, which makes it easy to understand the subject.

Dr. Harris has been very accommodating in sparing time for me at short notice. His academic engagements seem numerous and I appreciate him taking time off from his exciting pursuits at CNEL for me. The work conducted at his hybrid computation group seems very exciting. The advances being made in DSP will surely be of use in MRI/fMRI soon. I still marvel as how he and his collaborators can make a monkey move an artificial limb by just thinking about it.

I would also like to acknowledge the help of my MR physics colleagues Dr. Kyung Peck and Dr. David Soltysik for useful discussions in physics. Also, I would like to thank our neuropsychologists Dr. Anna Moore, Dr. Keith White, Dr. Tim Conway, Dr. Allison Cato, Christina Wierenga, Megan Gaiefsky, Christy Milsted and Ashley Wabnitz for useful discussions, subject coding and neuro-psychological input. This work was conducted with the help of NIH grants P50-DCO388 and RO1-DCO3455, Department of Nuclear and Radiological Engineering and the Brain Rehabilitation Research Center, VA RR &D, Gainesville, FL.

Lastly, I would like to thank my family members: my parents who stand by me though I have not been always there for them, my sisters Radha and Kalli who have been a guiding force in my life and God for blessing me with a life I am happy to lead.

TABLE OF CONTENTS

	<u>page</u>
ACKNOWLEDGMENTS	iv
LIST OF FIGURES	x
ABSTRACT	xv
CHAPTER	
1 BASICS OF MAGNETIC RESONANCE IMAGING	1
Origins of Magnetic Resonance Imaging	1
Concepts of Magnetic Resonance Imaging	1
Spin Physics and Magnetization	2
Resonance	3
Electro-Magnetic Induction	3
Relaxation	4
Longitudinal Relaxation, T_1	4
Transverse Relaxation, T_2	5
Gradients, Spatial Encoding and K-Space	6
Basic MR Pulse Sequences	7
Spin-Echo Pulse Sequence	7
Gradient-Echo Pulse Sequence	9
Contrast and Resolution	10
Fast Imaging Sequences	10
Echo-Planar Imaging	11
Spiral Imaging	12
2 FUNCTIONAL MAGNETIC RESONANCE IMAGING	14
Origins of Functional Magnetic Resonance Imaging	14
Principles of BOLD Functional MRI	15
BOLD Hemodynamic Response	16
Spatio-Temporal Characteristics of BOLD FMRI	18
Spatial Specificity	18
Temporal Resolution	18
Linearity of BOLD Response	19
FMRI Experiment Design	20
Blocked Paradigms	21

Event-Related Paradigms	21
FMRI Data Analysis	22
Overview	22
Image Registration.....	23
FMRI Noise Characteristics	24
Parametric Methods and General Linear Model	26
Inference	29
ROC Analysis.....	31
3 MOTION AND FMRI.....	32
Introduction.....	32
Major Sources of Motion Artifacts and Deterministic Solutions	33
Static Magnetic Field Effects	34
Spin History Effects	37
Inter-Shot Motion	38
Remarks	41
Mechanistic Solutions.....	41
Motion Parameter Regression	42
Stimulus-Correlated Motion.....	43
SCM-Ignoring Images	45
SCM-Detrending	46
Other Mechanistic Methods	46
4 TASK CORRELATED MOTION NOISE REDUCTION METHODS	48
Selective Detrending.....	48
Selective Detrending: Methods.....	50
Subjects and Task.....	51
Image Acquisition	51
Data Analysis.....	52
Deconvolution and Regression.....	53
Estimation of the TCM Signal Changes.....	53
Choosing Representative BOLD HRFs.....	55
Selective Detrending Algorithm.....	55
Analysis of Detrended Time-Series.....	60
Implementation of Motion Parameter Regression.....	61
Implementation of the Screening Images Method.....	62
Implementation of Non-Selective Detrending.....	62
Receiver Operating Characteristics	63
Reduction of False Positives	63
Retention of True Positives	64
5 RESULTS AND DISCUSSION.....	68
Results.....	68
Patient 1 (Pre-Treatment)	70

Patient 1 (Post-Treatment).....	75
Patient 2 (Pre-Treatment).....	80
Patient 2 (Post-Treatment).....	84
Control Subject 1.....	90
Control Subject 2.....	93
Control Subject 3.....	97
Control Subject 4.....	102
Discussion.....	106
6 CONCLUSION AND FUTURE WORK.....	112
Conclusion.....	112
Future Work.....	115
APPENDIX	
SELECTED PUBLICATIONS.....	117
Conference Abstracts.....	117
ISMRM Proceedings: Oral Sessions.....	117
ISMRM Proceedings: Poster Sessions.....	117
Full Papers.....	119
LIST OF REFERENCES.....	122
BIOGRAPHICAL SKETCH.....	132

LIST OF FIGURES

<u>Figure</u>	<u>page</u>
1.1 Timing diagram of a 2-D Spin Echo Sequence.....	8
1.2 K-space diagram of a 2-D Spin Echo Sequence.....	9
1.3 Timing diagram of an Echo-Planar Imaging Sequence.....	11
1.4 K-Space diagram of an Echo-Planar Imaging sequence	12
1.5 Timing diagram (left) and k-space diagram (right) of a 1-shot spiral EPI sequence.	13
2.1 Schematic representation of a BOLD hemodynamic response.....	17
2.2 The estimated impulse responses for a auditory cortex voxel activated at $F(16,470) = 30$, $p\text{-val} \approx 0$ (left) and a voxel with $F(16,470) = 2.5$ (right). The signal has been normalized to a unit maximum.	31
3.1 Two-shot spiral FMRI time series image of a mid sagittal slice showing swirl-like patterns arising from inter-shot motion. The image has been detrended of its time-series mean to better portray the effects of motion.....	39
4.1 Activation map overlaid on a low-resolution spiral FMR image. The red voxels correspond to $R^2 > 0.2$ and the yellow voxels denote $R^2 > 0.3$. The yellow arrow points to the voxel IRFs. The central voxel in the grid shows a selected TCM IRF.	54
4.2 Activation map of the maximal absolute cross-correlation coefficient with TCM CC_{TCM} , thresholded by $R^2 > 0.1$. The yellow voxels correspond to $\max(CC_{TCM}) >$ 0.7 and the red denotes $\max(CC_{TCM}) > 0.5$	58
4.3 Distribution of number of voxels undergoing non-selective detrending for a given $\max(CC_{BOLD})$ as a fraction of the number of voxels at that $\max(CC_{BOLD})$ for three different levels of separability, 0.2 (blue), 0.1 (green) and 0.0 (magenta) (a). Similar distributions for $\max(abs(CC_{TCM}))$ (b).	60
4.4 Estimated hemodynamic response of a true positive right medial frontal voxel of patient 1 (pre-therapy) dataset (blue) and the corresponding fit to a generic hemodynamic response (green).	66

5.1	Activation maps thresholded at $R^2 > 0.2$ for patient-1 (pre-scan) with no TCM noise-reduction (a), with selective detrending (b), with motion parameter regression (c), with ignoring 2 images after speech (d) and with non-selective detrending (e). The blue arrows indicate TCM voxel IRFs and the green arrows BOLD voxel IRFs.	69
5.2	Fraction of voxels detected as a function threshold R^2 for (a) the false-positives test-bed and (b) the true-positives test-bed for aphasia patient 1 (pre-therapy scan). The blue curve (ML0) represents the case of no motion correction, the black curve (ML2) represents the method of ignoring the first 2 images after speech, the green curve (MPR) represents the motion-parameter regression method, the magenta curve (dtsel) represents the selective detrending method and the red curve (dt) represents the non-selective detrending method.	72
5.3	Some representative TCM-related voxel IRFs (a); Some representative BOLD HRFs (b) from aphasia patient 1 (pre-therapy scan) data.....	73
5.4	The effect of the methods of noise correction on a right medial-frontal voxel BOLD HRF exhibiting an ‘early’ response for patient 1 pre-therapy scan (a). The effect of the methods of noise correction on a right inferior sulcus voxel, exhibiting both BOLD and TCM signal changes (b) for the same scan. The no-correction curve is hidden by the selective detrending curve in both figures.....	73
5.5	Activation maps thresholded at $R^2 > 0.2$ for patient 1 (post-therapy scan) with no TCM noise-reduction (a), with selective detrending (b), with motion parameter regression (c), with ignoring 2 images after speech (d) and with non-selective detrending (e). The blue arrows indicate TCM voxel IRFs and the green arrows BOLD voxel IRFs.	76
5.6	Some representative TCM-related voxel IRFs from patient 1 post-therapy scan (a). The effect of the methods of noise correction on a right medial-frontal voxel BOLD HRF exhibiting an ‘early’ response for the same dataset (b). The no-correction curve is hidden by the selective detrending curve.	78
5.7	Fraction of voxels detected as a function threshold R^2 for (a) the false-positives test-bed and (b) the true-positives test-bed for aphasia patient 1 (post-therapy scan). The blue curve (ML0) represents the case of no motion correction, the black curve (ML2) represents the method of ignoring first 2 images after speech, the green curve (MPR) represents the motion-parameter regression method, the magenta curve (dtsel) represents the selective detrending method and the red curve (dt) represents the non-selective detrending method.	78

5.8	Activation maps thresholded at $R^2 > 0.2$ for patient-2 (pre-therapy scan) with no TCM noise-reduction (a), with selective detrending (b), with motion parameter regression (c), with ignoring 2 images after speech (d) and with non-selective detrending (e). The blue arrows indicate TCM voxel IRFs and the green arrows BOLD voxel IRFs.....	81
5.9	Some representative TCM-related voxel IRFs from patient 2 pre-therapy scan (a). The effect of the methods of noise correction on a right medial-frontal voxel BOLD HRF exhibiting an ‘early’ response for the same dataset (b). The no-correction curve is hidden by the selective detrending curve.	83
5.10	Fraction of voxels detected as a function threshold R^2 for (a) the false-positives test-bed and (b) the true-positives test-bed for aphasia patient 2 (pre-therapy scan). The blue curve (ML0) represents the case of no motion correction, the black curve (ML2) represents the method of ignoring first 2 images after speech, the green curve (MPR) represents the motion-parameter regression method, the magenta curve (dtsel) represents the selective detrending method and the red curve (dt) represents the non-selective detrending method.	83
5.11	Activation maps thresholded at $R^2 > 0.2$ for patient 2 (post-therapy scan) with no TCM noise-reduction (a), with selective detrending (b), with motion parameter regression (c), with ignoring 2 images after speech (d) and with non-selective detrending (e). The blue arrows indicate TCM voxel IRFs and the green arrows BOLD voxel IRFs.....	85
5.12	Some representative TCM-related voxel IRFs from patient 2 post-therapy scan (a). The effect of the methods of noise correction on a right medial-frontal voxel BOLD HRF exhibiting an ‘early’ response for the same dataset (b). The no-correction curve is hidden by the selective detrending curve.	87
5.13	Fraction of voxels detected as a function threshold R^2 for (a) the false-positives test-bed and (b) the true-positives test-bed for aphasia patient 2 (post-therapy scan). The blue curve (ML0) represents the case of no motion correction, the black curve (ML2) represents the method of ignoring first 2 images after speech, the green curve (MPR) represents the motion-parameter regression method, the magenta curve (dtsel) represents the selective detrending method and the red curve (dt) represents the non-selective detrending method.	87
5.14	Activation maps thresholded at $R^2 > 0.2$ for control subject 1 with no TCM noise-reduction (a), with selective detrending (b), with motion parameter regression (c), with ignoring 2 images after speech (d) and with non-selective detrending (e). The blue arrows indicate TCM voxel IRFs and the green arrows BOLD voxel IRFs.....	89

5.15	Some representative TCM-related voxel IRFs from control subject 1. The effect of the methods of noise correction on a right medial-frontal voxel BOLD HRF exhibiting an ‘early’ response for the same dataset (b). The no-correction curve is hidden by the selective detrending curve.	91
5.16	Fraction of voxels detected as a function threshold R^2 for (a) the false-positives test-bed and (b) the true-positives test-bed for control subject 1. The blue curve (ML0) represents the case of no motion correction, the black curve (ML2) represents the method of ignoring first 2 images after speech, the green curve (MPR) represents the motion-parameter regression method, the magenta curve (dtsel) represents the selective detrending method and the red curve (dt) represents the non-selective detrending method.	91
5.17	Activation maps thresholded at $R^2 > 0.2$ for control subject-2 with no TCM noise-reduction (a), with selective detrending (b), with motion parameter regression (c), with ignoring 2 images after speech (d) and with non-selective detrending (e). The blue arrows indicate TCM voxel IRFs and the green arrows BOLD voxel IRFs.....	94
5.18	Some representative TCM-related voxel IRFs from control subject 2 (a). The effect of the methods of noise correction on a right medial-frontal voxel BOLD HRF exhibiting an ‘early’ response for the same dataset (b). The no-correction curve is hidden by the selective detrending curve.	96
5.19	Fraction of voxels detected as a function threshold R^2 for (a) the false-positives test-bed and (b) the true-positives test-bed for control subject 2. The blue curve (ML0) represents the case of no motion correction, the black curve (ML2) represents the method of ignoring first 2 images after speech, the green curve (MPR) represents the motion-parameter regression method, the magenta curve (dtsel) represents the selective detrending method and the red curve (dt) represents the non-selective detrending method.....	96
5.20	Activation maps thresholded at $R^2 > 0.2$ for control subject 3 with no TCM noise-reduction (a), with selective detrending (b), with motion parameter regression (c), with ignoring 2 images after speech (d) and with non-selective detrending (e). The blue arrows indicate TCM voxel IRFs and the green arrows BOLD voxel IRFs.	98
5.21	Some representative TCM-related voxel IRFs from control subject 3 (a). The effect of the methods of noise correction on a right medial-frontal voxel BOLD HRF exhibiting an ‘early’ response for the same dataset (b). The no-correction curve is hidden by the selective detrending curve.	100

5.22	Fraction of voxels detected as a function threshold R^2 for (a) the false-positives test-bed and (b) the true-positives test-bed for control subject 3. The blue curve (ML0) represents the case of no motion correction, the black curve (ML2) represents the method of ignoring first 2 images after speech, the green curve (MPR) represents the motion-parameter regression method, the magenta curve (dtsel) represents the selective detrending method and the red curve (dt) represents the non-selective detrending method.	100
5.23	Activation maps thresholded at $R^2 > 0.2$ for control subject 4 with no TCM noise-reduction (a), with selective detrending (b), with motion parameter regression (c), with ignoring 2 images after speech (d) and with non-selective detrending (e). The blue arrows indicate TCM voxel IRFs and the green arrows BOLD voxel IRFs.	103
5.24	Some representative TCM-related voxel IRFs from control subject 4 (a). The effect of the methods of noise correction on a right medial-frontal voxel BOLD HRF exhibiting an ‘early’ response for the same dataset. The no-correction curve is hidden by the selective detrending curve.	105
5.25	Fraction of voxels detected as a function threshold R^2 for (a) the false-positives test-bed and (b) the true-positives test-bed for control subject 4. The blue curve (ML0) represents the case of no motion correction, the black curve (ML2) represents the method of ignoring first 2 images after speech, the green curve (MPR) represents the motion-parameter regression method, the magenta curve (dtsel) represents the selective detrending method and the red curve (dt) represents the non-selective detrending method.	105

Abstract of Dissertation Presented to the Graduate School
of the University of Florida in Partial Fulfillment of the
Requirements for the Degree of Doctor of Philosophy

REDUCTION OF NOISE DUE TO TASK CORRELATED MOTION IN EVENT
RELATED OVERT WORD GENERATION FUNCTIONAL MAGNETIC
RESONANCE IMAGING PARADIGMS

By

Kaundinya S. Gopinath

December, 2003

Chair: Wesley Bolch

Cochair: Richard W. Briggs

Major Department: Nuclear and Radiological Engineering

Event-related overt word generation functional magnetic resonance imaging paradigms play an important role in the understanding of brain function. The necessity for monitoring the subject responses in functional magnetic resonance imaging of patients requires use of overt word generation paradigms. Speech-related task-correlated motion acts as a major confound in the analysis of overt word-generation paradigms. Task-correlated motion artifacts in event-related overt word generation paradigms have been treated with three main methods: motion parameter regression, ignoring/screening signal changes during speech and detrending functional magnetic resonance imaging datasets of components proportional to the task-correlated motion time-series chosen from false-positive task-correlated motion voxels. In this work a new selective detrending method for reduction of noise associated with task-correlated motion in event-related overt word generation functional magnetic resonance imaging paradigms is introduced.

The performance of this method is compared with the other three methods of task-correlated motion noise reduction. The selective detrending method outperforms the other three methods in terms of reduction of task-correlated motion false-positives as well as retention of blood oxygenation level dependent signal true-positives.

CHAPTER 1 BASICS OF MAGNETIC RESONANCE IMAGING

Chapter 1 discusses the basic concepts of magnetic resonance imaging (MRI). The origins of nuclear magnetic resonance (NMR), principles of magnetic resonance imaging, and development of fast imaging sequences are discussed.

Origins of Magnetic Resonance Imaging

The idea of nuclear magnetic resonance owed its birth to the discovery of the proton spin by Stern and Gerlach (1) in 1933, through an extension of methods which helped them discover electron spin in 1921. Rabi and colleagues were the first to predict and observe nuclear magnetic resonance in 1937 (2). Bloch and Purcell extended these concepts to measure the proton spin precessional signal from samples, using radiofrequency methods (3, 4). All of the above-mentioned luminaries were awarded Nobel Prizes for their work.

MRI had its beginnings in the seminal work of Mansfield and Grannell and Lauterbur in the 1970s (5, 6). They discovered that if a known spatially varying magnetic field is introduced across a sample, the precession of spins within the sample will depend on their spatial locations.

Concepts of Magnetic Resonance Imaging

The NMR or MRI signal has its basis in quantum mechanics. The quantity spin angular momentum has no exact analog in classical mechanics. The signal observed at the imaging end, however, can be visualized in terms of aggregate magnetization of a population of spins and is a classical regime manifestation. Thus, depending on the

physical quantity examined, the concepts of magnetic resonance imaging are most easily elucidated by taking recourse to quantum mechanics, classical mechanics or semi-classical approximations.

Spin Physics and Magnetization

The nuclei of atoms consist of fermions, protons and neutrons, with half integer spins. The nuclide as a whole has a spin quantum number, I . The spin of the nucleus is an inherently quantum mechanical entity. The energy states that the nucleus can have, called energy levels, are quantized. In the presence of a static D.C. magnetic field, B_0 , the nuclide can inhabit $2I+1$ energy levels given by (7)

$$E = S_z g \frac{e\hbar}{2mc} B_0 \quad [1]$$

where S_z can take values from $-I$ to $+I$, e is the electronic charge, \hbar is the Planck's constant, m is the mass of the nucleus and c is the velocity of light in gauss-ergian units and g is the Lande g-factor. A hydrogen nuclide (which consists of a proton) has spin $I = 1/2$ and can occupy two states, aligned either with or against the field.

$$E_{\pm} = \pm \frac{1}{2} \hbar \omega_0 \quad [2]$$

where

$$\omega_0 = \gamma B_0 \quad [3]$$

is the expression for angular frequency in which the constant γ , termed the gyro-magnetic ratio, can be evaluated from equation [1] and is equal to 42 MHz/Tesla for a proton.

In an ensemble of water protons in a magnetic field, the relative population of nuclear spins in the two states is given by

$$\frac{N_+}{N_-} \propto \exp\left(-\frac{E_+ - E_-}{kT}\right) \quad [4]$$

where N_+ and N_- are the number of nuclear spins in E_+ and E_- energy levels respectively, k is the Boltzmann's constant and T is the temperature. Thus there is a net magnetization M_0 in the B_0 direction. The magnetization vector M_0 precesses around the applied magnetic field B_0 with an angular frequency ω_0 , called the Larmor frequency, which is the same as the one obtained in equation [3].

Resonance

If a magnetic field B_0 is applied to a population of nuclear spins in a laboratory, they precess around the applied field. The reference frame in which the spins are stationary is rotating with respect to the laboratory frame with the angular frequency of the spins. Now, if a magnetic field, B_1 , is applied in this rotating frame at right angles to the spins, they can be tipped, i.e., start precessing around the field B_1 . It can be shown (8) and is intuitively obvious that the applied magnetic field B_1 should oscillate with an angular frequency equal to the Larmor frequency of precession of the spins in the laboratory frame. This desired "resonance" condition between the oscillation frequency of the B_1 field and the precession frequency supplies the "R" in the acronym MRI. For water protons and all other MR imaging nuclides this frequency is in the radio range, hence the term radio-frequency (RF) magnetic field.

Electro-Magnetic Induction

When the RF magnetic field B_1 is switched off, the will start precessing about the permanent field, B_0 . Thus, the magnetic flux through a coil, with axis aligned perpendicular to B_0 , will change resulting in an electro-motive force (e.m.f) induced in the coil according to Faraday's law of electro-magnetic induction.

$$\varepsilon = -\frac{d}{dt}\Phi_M \quad [5]$$

where Φ_M is flux associated with the changing magnetization field passing through the coil after removal of the RF transmit field B_1 . This is the basis of MRI signal generation.

Relaxation

The e.m.f and hence the MR signal derived in the last section depend on the rate of change of the magnetization in the plane transverse to the B_0 field. This evolution of the magnetization of the sample depends on two types of interactions involving the nuclear spins in the sample. Both these interactions tend to the virialization of the system and are hence termed relaxations.

Longitudinal Relaxation, T_1

A spin = 1/2 system has two allowed energy states. In the absence of an applied magnetic field, the two states are more or less equally populated. The transition from equi-population of states, in the absence of a field, to a preferential occupation of the lower energy state in the presence of an applied field, described in equation [4], is caused by the relaxation mechanism called longitudinal relaxation (9). The transition in states for a given spin is achieved by resonant absorption of a quantum of energy by the spin from the molecular environment (lattice). Thus, the term “resonant” is the operative word here. Only energy transactions (e.g., arising from rotation/translation of nuclear moments within the molecule) which lead to the transfer of energy $E = \hbar\omega_0$ from the lattice to the nuclear spin or vice-versa lead to longitudinal relaxation. If B_0 is applied along the z-direction, the time evolution of longitudinal magnetization, i.e., magnetization parallel to the z-direction, after the removal of the 90° spin flipping field, B_1 , is given by (10)

$$M_z(t) = M_0(1 - \exp(-t/T_1)) \quad [10]$$

where, M_z is the magnetization at time t , M_0 is the equilibrium magnetization and T_1 is called the longitudinal relaxation time. The value of T_1 for proton imaging will depend on the molecular environment of the sample. For water (H_2O) protons, T_1 is about 1000 msec. T_1 increases with the strength of the B_0 field in liquid samples at typical NMR field strengths.

Transverse Relaxation, T_2

In a physical MR sample the local magnetic field experienced by a given spin is a combination of the B_0 field and the fields generated by its neighbors. After a 90° tip of a set of spins, the net transverse magnetization decays with time. This is because the different spins constituting the net transverse magnetization fan out or dephase as they experience different time-dependent local magnetic fields. Thus, the MR signal which depends on the transverse magnetization goes to zero. The evolution of the transverse magnetization is given by (10)

$$M_{\perp}(t) = M_{\perp}(0) \exp(-t/T_2) \quad [11]$$

where M_{\perp} is the transverse magnetization and T_2 is called the transverse relaxation time. T_2 relaxation is caused by both slow and fast molecular motions, in contrast with T_1 relaxation, which can be caused only by fast molecular motions at the Larmor frequency. Hence T_2 is always lesser than or equal to T_1 . In practical situations, there are inhomogeneities in the permanent magnetic field B_0 , which cause increased dephasing of the spins leading to a shortening of the transverse relaxation time. This leads to an effective transverse relaxation time T_2^* given by

$$1/T_2^* = 1/T_2 + 1/T_2' \quad [12]$$

where the second term in equation [12] refers to the T_2 shortening due to the B_0 inhomogeneities.

Gradients, Spatial Encoding and K-Space

The ability to spatially separate the signal comes from a simple, yet brilliant extension of the Larmor relation, equation [3], first discovered by Lauterbur (6). If the z-component of the magnetic field is varied along the x-direction, the spins in the x-y plane will precess at different frequencies depending on their x-coordinates.

$$\omega(x) = \gamma G_x x + \omega_0 \quad [13]$$

where G_x is the applied linear x-gradient to the z-component of the magnetic field. Thus by demodulating the signal at different frequencies, $\omega(x)$, a representation of MR spin density at different points along the x-axis can be obtained. The signal along the y and z-axes can be spatially encoded in an analogous fashion.

For an isochromat of spins seeing a constant background field over which a linear x-gradient field is superimposed, after demodulation of the signal, the phase is given by

$$\begin{aligned} \varphi &= \gamma x \int G_x(t) dt \\ &= 2\pi k_x x \end{aligned} \quad [14]$$

where

$$k_x = \int G_x(t) dt \quad [15]$$

is the spatial frequency component of the phase.

The MR signal can be considered to be the sum of all isochromat signals, each weighted by the local spin density $\rho(x)$ and the phase term from equation [14].

$$s(k_x) = \int \rho(x) \exp(-i2\pi k_x x) dx \quad [16]$$

Hence, the effective spin density $\rho(x)$ can be estimated from an inverse Fourier transform of the signal $s(k_x)$. In three dimensions

$$\rho'(x, y, z) = \iiint s(k_x, k_y, k_z) \exp(i2\pi(k_x x + k_y y + k_z z)) dk_x dk_y dk_z \quad [17]$$

where ρ' is an estimation of the effective spin density which becomes equal to the exact value when the reconstruction is perfect.

In equation [17], the Fourier inverse of the reconstructed image space is the k-space, which is obtained after demodulating the signal. The k-space contains all the information regarding the manner in which the magnetic field gradients were played out to spatially encode the image. All MRI sequences can be succinctly represented by their acquisition k-space diagrams. Since the MR image is obtained as an inverse Fourier transform estimate of the demodulated signal k-space, the latter, in principle, contains more information about the image.

Basic MR Pulse Sequences

The vast majority of MRI pulse sequences are a variation on two basic image acquisition methods, the spin-echo sequence and the gradient echo sequence. The most popular rapid image acquisition sequences in conventional use, the echo-planar imaging (EPI) sequences, are variations on the gradient echo sequence. EPI as well as spiral-EPI sequences have the capability of acquiring the whole image in one acquisition.

Spin-Echo Pulse Sequence

Figure 1.1 shows a timing diagram of a simple spin echo sequence (11). A 90° RF pulse is first applied (period 1) in conjunction with a slice selective gradient G_z to create a transverse magnetization in the slice encoded by G_z . During period 2, spins which dephase as a result of the slice selective gradient are rephased by a negative

compensating gradient. Also a programmable phase encoding gradient G_y is applied which encodes spins in the y -direction. In addition, a readout direction gradient G_x is applied which serves the purpose of compensating for phase that will be accrued due to the readout gradient in period 4. In period 3 a slice-selective 180° RF pulse is applied. The purpose of this pulse is to generate a “spin-echo” in period 4, when all the spins which have been dispersed by the applied and background gradients will come back in phase. The readout gradient G_x is played out during collection of the echo in period 4, to encode spins in the x -direction. The above sequence is repeated for different values of the phase encoding gradient, G_y to encode the y -axis. The time interval between the application of the RF pulse and the acquisition of the center of the echo is called the echo time (TE). The time-interval between two successive phase-encoding steps is called repetition time (TR).

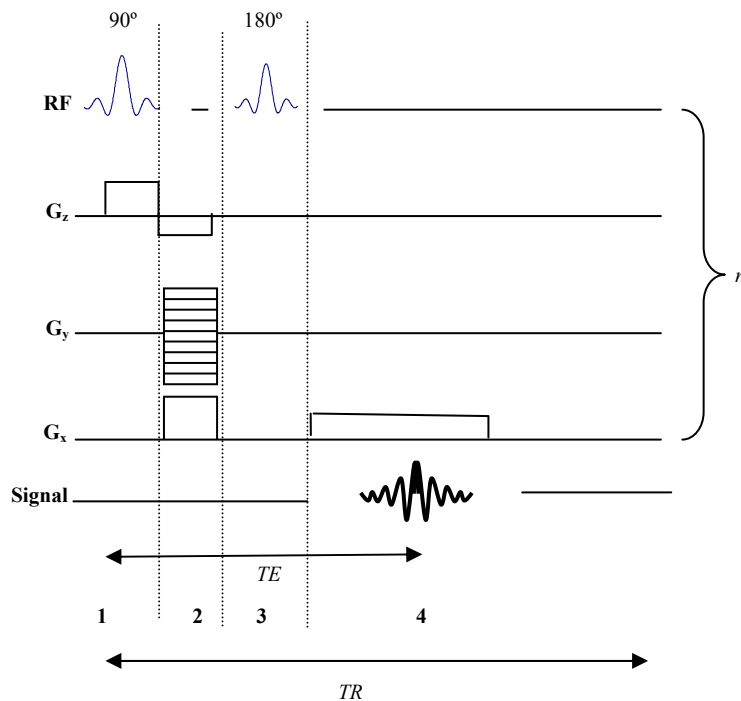


Figure 1.1: Timing diagram of a 2-D Spin Echo Sequence

In terms of k-space (Figure 1.2) each repetition (echo) of the sequence generates one line of the k-space. After acquisition of all the echoes a two-dimensional k-space image is generated, which upon inverse Fourier transformation generates a 2-D image of the slice.

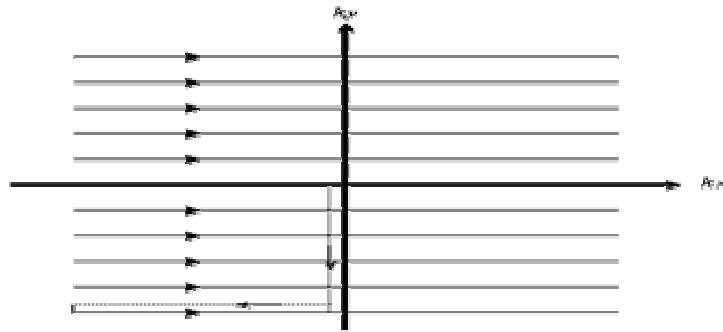


Figure 1.2: K-space diagram of a 2-D Spin Echo Sequence

Gradient-Echo Pulse Sequence

The gradient echo sequence differs from the spin echo sequence in the manner in which the echo is generated during readout. While the spin echo sequence generates the echo by the use of a 180° refocusing pulse, in the gradient echo sequence, the echo is generated by the gradient reversal in going from the refocusing G_x gradient to the readout G_x gradient. Thus, the echo is created when the spins dispersed by the initial negative G_x are brought back in phase during readout by the positive G_x . This form of echo generation can not compensate for the phase dispersal due to background gradients. Thus the signal decays faster (through T_2^* decay) in a gradient echo sequence when compared to a spin echo sequence (through T_2 decay). Both the gradient echo sequence and the spin echo sequence are examples of 2-D FT spin warp imaging.

Contrast and Resolution

The MR signal for a 2-D FT spin warp sequence is given by

$$S(TR, TE, \rho_0, \theta) = \rho_0 \frac{(1 - \exp(-TR/T_1)) \sin \theta}{1 - \exp(-TR/T_1) \exp(-TR/T_2) - \exp(-TR/T_1) \cos \theta} \cdot \exp(-TE/T_2^*)$$

[18]

where S is the signal as a function of repetition time (TR), echo time (TE), effective spin density ρ_0 and RF flip angle θ . By judicious choice of the parameters of the scan, image contrast can be achieved by enhancing the differences in T_1 , T_2 (T_2^*) or spin density between different constituents in the sample. These three constitute the most basic contrast generating mechanisms. Other contrast parameters in vogue include flow, magnetic susceptibility difference and diffusion (to name just a few).

The image resolution is dictated by the number of phase-encoding steps N_y , the number of acquisition samples in the readout N_x and the field of view (FOV) in the x and y -directions. For brain imaging applications the FOV ranges from 20-24 cm and the image matrix is 256 by 256, giving an in-plane resolution of about 1mm by 1mm.

Fast Imaging Sequences

The scanning time required for the 2D-FT spin warp sequences mentioned above can be quite long. Roughly, the scanning time will be given by TR times N_y , the number of phase encode steps. For TR = 1sec, a 64 x 64 matrix image will take 64 seconds. For many MR applications faster acquisition times are required. One major advance in shortening acquisition times was performed by Mansfield's group (12) in Nottingham when they invented the Echo-Planar Imaging (EPI) sequence. Mansfield himself had introduced the concepts of EPI a decade or so back (13). The Stanford group (14-15)

subsequently devised a different version of EPI called the spiral-EPI (or just spiral) sequence.

Echo-Planar Imaging

Figure 1.3 shows a timing diagram of a conventional single-shot EPI sequence. The whole of k-space (Figure 1.4) is acquired in a single application of the RF pulse. An oscillatory gradient G_x is applied along the frequency encoding direction and a train of gradient echoes is collected. Each echo is then phase encoded independently by blipped G_y gradient and the whole k-space matrix is covered. The blips in G_y gradient occur at during each zero crossing of the G_x gradient.

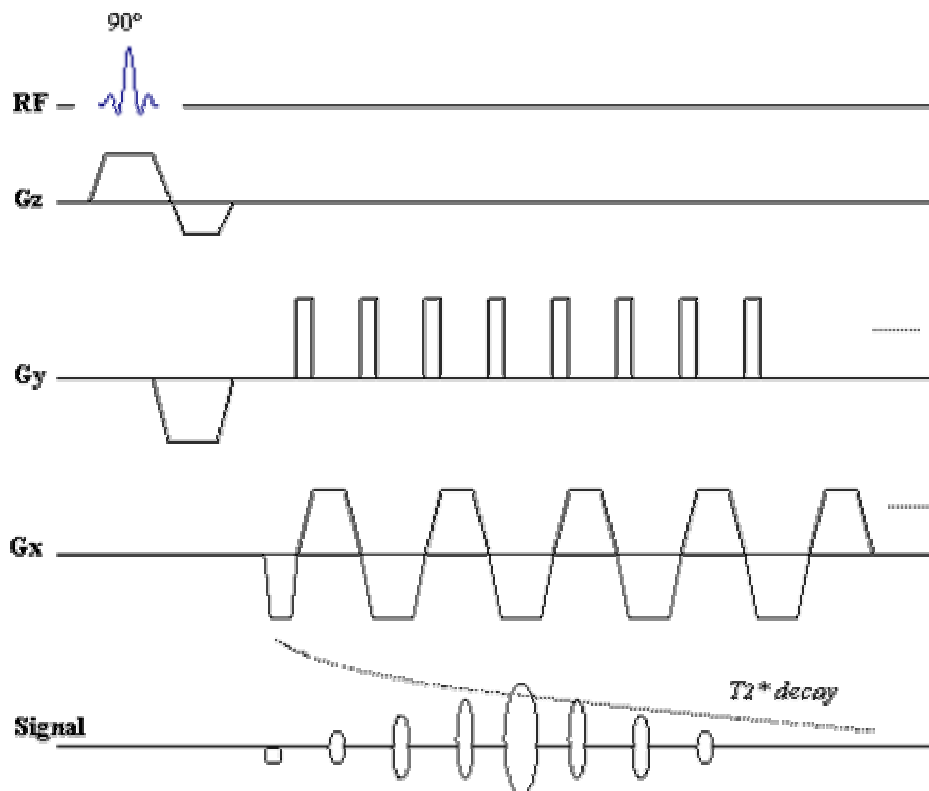


Figure 1.3: Timing diagram of an Echo-Planar Imaging Sequence

Thus each echo corresponds to one line of k-space as in Figure 1.2. While each k-space line in Figure 1.2 was acquired in one TR, all the k-space lines in Figure 1.4 are

acquired in a single TR. Modern EPI sequences can acquire one slice in as low as 30 milli-seconds (16).

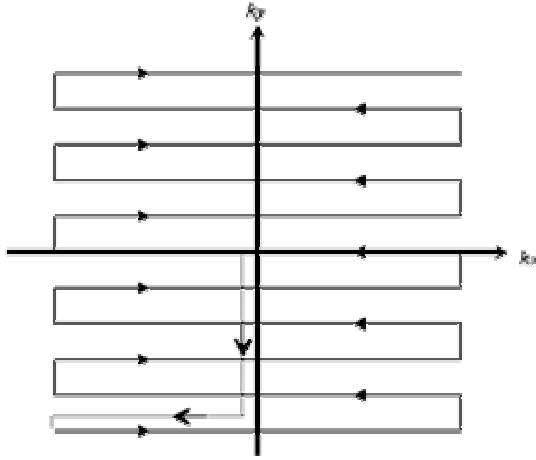


Figure 1.4: K-Space diagram of an Echo-Planar Imaging sequence

Spiral Imaging

An extension of the conventional EPI sequence is the spiral sequence (17-19).

Figure 1.5 shows the timing diagram and corresponding k-space diagram of a spiral fast imaging sequence. In a spiral sequence, both the G_x and G_y gradients oscillate with increasing amplitude as a function of time during readout. There is no phase-encoding gradient. The k-space is acquired in a spiral-fashion, hence the name. The gradient slew rate (the maximal rate of change of the gradients in the pulse sequence) requirements for spiral imaging are not as high as for conventional EPI sequences (18, 19). Scan times per slice are comparable to that of standard EPI sequences. Spiral sequences are inherently self-refocussed and do not have geometric distortions that plague EPI sequences. However, they require off-line reconstruction which can take much longer than EPI sequences.

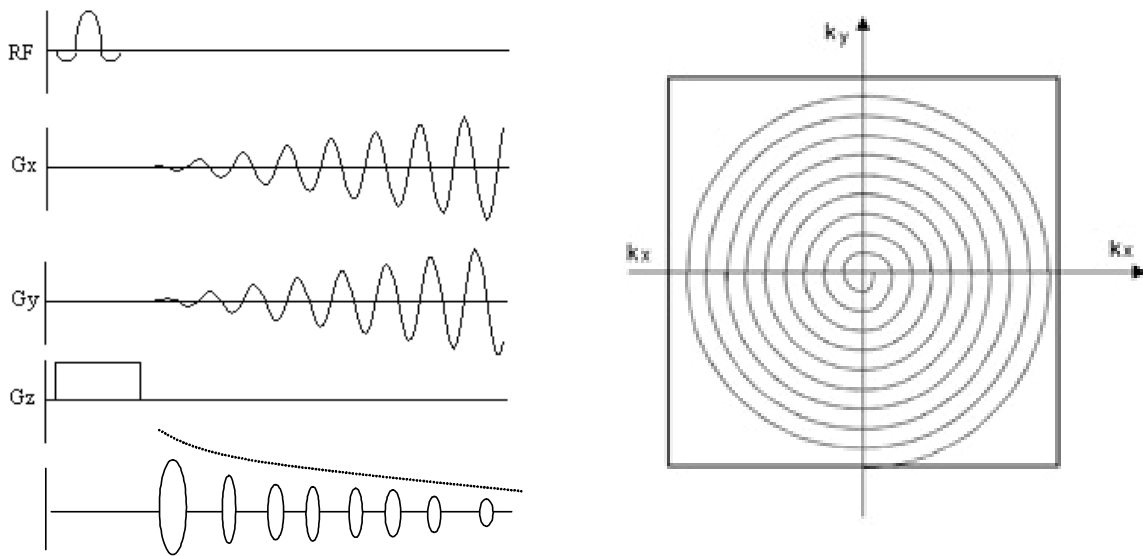


Figure 1.5: Timing diagram (left) and k-space diagram (right) of a 1-shot spiral EPI sequence.

CHAPTER 2 FUNCTIONAL MAGNETIC RESONANCE IMAGING

Chapter 2 discusses concepts of functional magnetic resonance imaging (fMRI). The origins of this functional imaging modality, the principles of blood oxygenation level dependent (BOLD) fMRI and the spatio-temporal properties of the BOLD fMRI signal are discussed. Finally, salient features in fMRI experiment design and data analysis are reviewed.

Origins of Functional Magnetic Resonance Imaging

Until the late 1980's, the decay of signal due to local magnetic field inhomogeneities due to T_2^* relaxation was considered a nuisance and sought to be minimized. Among the first to realize that the presence of a paramagnetic substance in the blood stream acts as a vascular marker, giving useful contrast, were researchers of the MGH group (20), who pioneered the application of contrast agents to study brain perfusion in animals. In the early 1990's, Belliveau and collaborators (21) first extended these principles to image functional brain activation in humans with MR contrast agents. Subsequently Ogawa, working with laboratory animals, in a seminal paper (22), demonstrated that similar changes of MR image contrast can be obtained by changing the oxygenation state of blood. This observation was rooted in the fact [first measured by Pauling in 1936 (23)] that deoxyhemoglobin is more paramagnetic than oxyhemoglobin, which itself has a very similar magnetic susceptibility to that of brain tissue. Brain activation leads to creation of imbalances between the oxygen uptake and blood flow leading to blood oxygenation level dependent (BOLD) MRI signal contrast around

cortical vessels, which can be mapped non-invasively with MR sequences optimizing T_2^* contrast. The first human subject BOLD FMRI was performed in 1992 by Kwong (24) and Ogawa (25), using gradient-echo MR images. BOLD FMRI accounts for most functional imaging studies of the brain with MRI, though another method involving the labeling of arterial spins with a preparatory RF pulse, first advocated by the Pittsburgh group (26), is fast gaining currency. This is a cerebral blood flow monitoring technique for functional MRI.

Principles of BOLD Functional MRI

BOLD FMRI, like other functional neuroimaging methods such as positron emission tomography (27) and optical imaging (28) is based on physiological responses related to brain activation. Brain function is spatially segmented and compartmentalized. This can be mapped through measuring secondary changes in metabolism and hemodynamics in response to neuronal activity.

The MRI signal acquired with a single pulse sequence is given by

$$S = M(T_1^*) \cdot A(T_2^*) \quad [2.1]$$

where M is the sampled magnetization, determined by T_1^* (T_1 with inflow) and A is the signal attenuation, governed by the T_2^* decay of the in-plane magnetization. The

activation-induced MRI signal change in the capillary bed is given by

$$\Delta S / S = \Delta M / M + \Delta A / A \quad [2.2]$$

The first term in equation [2.2] is the change in signal due to inflow and is (at steady state attained after repetitive pulsing) very small (29), $\Delta M / M \sim 0.0035$.

The second term in equation [2.2], when described by a simple T_2^* decay is given by

$$\Delta A / A = -TE\Delta(1/T_2^*) \quad [2.3]$$

for echo-time TE and activation induced change in transverse relaxation, $\Delta(1/T_2^*)$. BOLD contrast is solely due to the susceptibility difference of red cells with paramagnetic deoxyhemoglobin relative to their surrounding. The bulk susceptibility of red cells, which is due to the hemoglobin deoxygenation level, changes the field shift inside and outside the red cells. The change in T_2^* due to brain activation can be written in terms of the blood oxygenation level Y , change in cerebral blood flow, ΔCBF , magnetic field, B_0 and echo-time, TE (23).

$$\Delta A / A = a \cdot TE \cdot \Delta(vB_0(1 - Y)) \quad [2.4]$$

where a is a constant and v is the blood volume fraction. Equation [2.4] is actually a simplification. The exact dependence of the MRI signal change due to activation on the hemodynamic and MRI parameters is still a subject of research.

BOLD Hemodynamic Response

Figure 2.1 shows a schematic representation of a BOLD hemodynamic response to an applied neuronal stimulus. The response can be characterized by segmenting it into four epochs. First, there is a delay which could range from 2 to 4 seconds (30) between the application of the stimulus and the onset of hemodynamic response. This delay could be both due to delay in neuronal firing in response to the stimulus or sluggishness associated with the neurovascular coupling.

The second feature, shown as a dotted curve is often called the “initial dip”. This event, which can last up to 2 seconds (31) is the result of a local increase in cerebral metabolic rate of oxygen consumption (CMRO₂) at the site of neuronal firing, leading to an increase in the local deoxyhemoglobin concentration, which results in decrease in MR signal intensity. This phenomenon is not often observed (for instance initial dip is seen

only $B_0 \geq 3T$ and at temporal resolutions around or less than 1 second), and hence designated by the dashed curve.

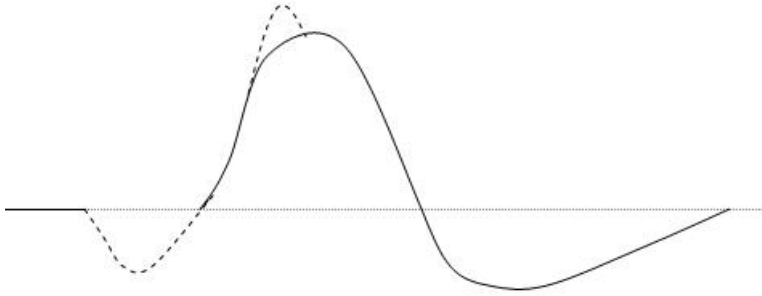


Figure 2.1: Schematic representation of a BOLD hemodynamic response

The next epoch is the positive BOLD response. This happens due to an increase in cerebral blood flow (CBF) which occurs after neuronal firing. This results in hyperoxygenation of the neural tissue which leads to a decrease in the deoxyhemoglobin concentration and thus an increase in MR signal. The positive BOLD response to a neuronal impulse consists of a relatively sharp increase (about 4-6 seconds) to maximum and a slower decrease characterized by fall-times of about 7 seconds or more (32). This epoch is the classical BOLD response, which is utilized to quantify brain activation in most instances of fMRI analysis.

Sometimes a positive overshoot (dashed curve) is seen at the start of the positive BOLD response. One plausible reason for the overshoot is the mismatch in the rates of adjustment of CBF and the cerebral blood volume (CBV) (33) during changes in stimulation state. Soon after neuronal stimulation, the CBF exhibits an abrupt jump to its elevated level while the CBV adjustment is more gradual. This results in a hump in the BOLD response when there is an short-lived increase in the oxygenation of the tissue due to the mismatch between CBF and CBV. The reverse happens at the end of the positive BOLD response, when elevated CBV levels persist even as CBF and hence the

oxygenation decreases leading to a decrease in MR signal. This incompletely understood post-stimulus undershoot can take up to tens of seconds to recover (34).

Spatio-Temporal Characteristics of BOLD FMRI

It is profitable to explore the relationship between brain activation and the corresponding BOLD hemodynamic response. In particular, it would be remunerative to examine in detail how the BOLD response is related to the underlying brain activation in time and space.

Spatial Specificity

Apart from the BOLD response changes originating in the capillaries embedded within the cortex and localized to site of neural activity, the hemodynamics that give rise to observed FMRI signal changes originate from a number of sources on both the supply (arterial) and draining (venous) side which can be as much as a centimeter away from site of neural activity (35-36). To get around the loss of specificity due to the draining vein effect, which is a by-product of the hyperoxic phase of the BOLD response, some authors (37) have hypothesized that use be made of the “initial dip” part of the BOLD response which is a corollary of the early hypoxic phase. This is thought to be more localized to the site of neural activity. But as mentioned before, the initial dip can be elusive to image and requires high temporal resolution too. Methods involving MR phase images (38-39) show more promise in discriminating large vessel effects.

Temporal Resolution

The neuronal processes associated with brain function range do not extend over a few hundred milliseconds even for the more complex cognitive tasks (40). In contrast, the BOLD hemodynamic response to a neural stimulus could extend over tens of seconds. To answer the question of how separated in time, neuronal events have to be, in order to be

resolved with BOLD FMRI, it is necessary to understand the exact mechanism of coupling between brain activity and the vascular response. At present the nature of neurovascular coupling is not well understood. Studies involving measurements of evoked potentials and BOLD MR signals (41) have claimed that temporal dynamics of brain can be measured indirectly by observed correlations between the BOLD response signal parameters and dynamics of underlying brain function. But the observations are open to interpretation in terms of their generalization to all brain functions and locations as well as how consistently the measured electrical activity reflects brain function (42).

Linearity of BOLD Response

Optimal design of FMRI experiments requires knowledge of the nature of the relationship between stimulus presentation and evoked BOLD hemodynamic response. Early ventures into FMRI signal analysis assumed a linear relationship between stimulus duration and evoked BOLD FMRI signal change (43). Subsequent studies have demonstrated significant departures from linearity for stimulus durations less than 4-6 seconds (45, 46). Another manifestation of this nonlinearity is the dependence in the amplitude and latency of the hemodynamic response to a neural stimulus on the timing of preceding stimuli. At inter-stimulus-intervals (ISI) of 5-6 seconds or greater, the hemodynamic responses of multiple stimuli sum in a roughly linear fashion (47). However at shorter intervals (e.g. less than 2 seconds), there are significant departures from linearity, in that the hemodynamic response to the second stimulus in a pair is reduced in amplitude and increased in latency compared to that evoked by a single stimulus. This phenomenon has been observed in auditory (48), motor (47) and visual cortices (49). The aforementioned studies on nonlinearity of the BOLD hemodynamic response were done on lower level cognitive systems. Gopinath et al. (50) noticed

refractoriness at longer ISIs (3seconds and more) in the hemodynamic response of voxels in the supplementary motor area (SMA) under a higher level cognitive task, a semantic word generation paradigm. Extending on this work Gopinath et al. (51) subsequently found an increase in the nonlinearity of the BOLD hemodynamic response along a functionally connected neural pathway. In this study the change in the linearity of the relationship between stimulus pattern and BOLD response along the receptive and expressive language processing network was observed. Under an overt word repetition task, an increase in the nonlinearity of the BOLD response was observed in the output (motor cortex) of the language processing network compared to the input (auditory cortex).

The above discussion leads one to explore the neural basis of FMRI signal. Questions of importance are *does the FMRI signal reflect axonal firing output as does EEG?* (52) or *does it reflect post- and pre-synaptic signals?* (53, 54). A recent review on this subject (55) suggests that the BOLD effect should be interpreted as a reflection of neuronal signaling and not as a locus of increased energy utilization. Much work needs to be done on this subject to get a clear picture of the neural basis of FMRI signal. Design and analysis of FMRI experiments will clearly benefit from a better understanding of the neurovascular coupling.

FMRI Experiment Design

FMRI is rapidly gaining currency as a preferred method for imaging brain function. FMRI has been used to image brain activation in simple brain functions stimulating the auditory areas of the brain (56), motor areas (57) and visual areas (58). With the success of these experiments FMRI has quickly graduated to imaging higher level cognitive processes in the brain dealing with language (59), pain (60) and perception (61) among a

host of other systems. It has also found application in treatment of pathologies (62) and pre-surgical planning (63). FMRI study designs can be broadly classified into two types: 1) blocked paradigms and 2) event-related paradigms.

Blocked Paradigms

Blocked paradigms were the first approach to be employed in FMRI studies (25, 26). Blocked paradigms involve application of FMRI stimuli for finite durations ranging from ~10 sec to ~ 1 min interspersed with rest intervals of about the same durations. Regions in the brain which show significant signal change between the “active” and rest conditions can be considered “activated”. Blocked paradigms have flexibility, allowing use of multi-factorial designs (64) as well as parametric designs (65). The rest intervals may be of uniform size (boxcar stimulus order) or varied (randomized block designs). Optimization of blocked paradigms has been studied with regard to both neuropsychological and statistical terms (66), though further refinement of the optimization procedures is in order to account for variability in hemodynamic response, brain activation and noise of the associated FMRI signal time-series. With the knowledge at hand (66), one can surmise that the length of the active and rest intervals should be such that the BOLD FMRI signal will be at activation frequencies in the range 0.08-0.15 Hz. This is because the hemodynamic response acts as a low-pass filter and attenuates the signal at frequencies greater than ~ 0.2 Hz and also the FMRI time-series noise has been known to exhibit disproportionate spectral power at frequencies (67) below 0.05 Hz.

Event-Related Paradigms

The blocked paradigms of the previous section offer the highest efficiency among the currently used designs in FMRI (68) in detecting activated areas. However, the inherent characteristics of blocked paradigms prevent them from being able to estimate

the hemodynamic responses of each individual stimulus in a block (69). Also, blocked designs cannot readily accommodate behavioral constraints imposed by some event sequences, such as those occurring infrequently, randomly or discretely, those not having precise time-locking to known stimuli, or mixing of events from fundamentally different tasks (70). Event-related FMRI (ER-FMRI) designs overcome all the above-mentioned obstacles and also provide means of examining questions regarding the dynamics and time course of neural activity as well as neurovascular coupling. Early ventures in ER-FMRI (70, 67) involved application of periodic single-trial stimuli. Subsequent developments in ER-FMRI have demonstrated that pseudo-random ordered single-trial stimulus sequences are more optimal in terms of both detection and estimation efficiency of the signal changes in ER-FMRI (69, 71, 72).

FMRI Data Analysis

The BOLD signal changes in FMRI at 3T are typically 2-10 %. Tasks involving higher level cognitive systems (like language) tend to exhibit a smaller signal change (2-4%) than those involving activation of the primary cortices. The role of FMRI data analysis is to extract this signal from the background noise.

Overview

The data analysis methods can be categorized into 1) hypothesis independent methods and 2) hypothesis driven methods. Hypothesis independent methods such as ICA (73), fuzzy-cluster analysis (74) have yet to be perfected for FMRI and are not widely used. Hypothesis driven methods can be categorized into a) parametric methods and b) nonparametric methods.

Image Registration

Proper image registration (aligning the time series images) is imperative to minimize the effect of motion on the fMRI signal. Image registration is the first step in the post-processing of acquired fMRI images. Image registration is usually performed with image-intensity-based methods (75-77). The guiding principle in all intensity-based image registration methods is the minimization of some quantity related to the voxel-wise image-to-image intensity differences. Conventional intensity-based image registration methods consist of two steps (75-77). The first step is the estimation of the rotation and translation parameters required to align a given image with the base image, usually obtained as best-fit rigid body rotation and translation parameters in the global optimization algorithm used to re-align the images. The second step is the assignment of intensity values to the voxels in the rotated image grid. This resampling is done by means of polynomial (77) or Fourier interpolation (78). Polynomial interpolation is local (band-limited). This can introduce blurring in the resampled images (i.e. correlation between the signal values at nearby pixels). Fourier interpolation is more desirable, albeit slower. In Fourier interpolation the image is resampled globally in the reconstructed k-space, which upon inverse Fourier transform gives the registered image. The blurring introduced is much reduced.

There is a separate class of feature-based registration methods which have been proposed for fMRI (79, 80, 81). These methods segment a known anatomic contour in all the images of the fMRI time-series and use the contour as a reference for tracking and compensating for head motion. Gopinath et al. (80) proposed one such method which is now available in a more refined form (81) to implement a 2D feature-based image registration. This method endeavors to segment an anatomic shape prior (e.g. the corpus

callosum) in each of the images in the fMRI time-series and estimate the motion parameters involved in aligning the prior in all the images in the time-series. These methods are still in their infancy and are not in general use. The main drawback lies in the difficulty in segmentation of low resolution fMRI images.

fMRI Noise Characteristics

The preponderance of fMRI studies in the literature use parametric methods of data analysis. The characterization of the noise structure is critical to parametric analyses of fMRI time-series. The earliest fMRI data analysis methods assumed the underlying noise structure to be wide sense stationary (WSS) Gaussian white noise (43). More detailed inspections have revealed significant colored (67, 82), non-Gaussian (83) as well as non-stationary (84) features in the fMRI noise. Most methods of parametric data analysis handle the fMRI noise in one of the following three ways. Some neuroimaging softwares (85) assume the noise structure to be WSS and Gaussian white. They typically fit a polynomial trend to the baseline to reduce the power of low-frequency noise components in the time-series. This method has some merit in that the fMRI time-series is believed to have a strong white noise component. For example, Purdon et al. (82), using a WSS Gaussian white noise plus a first order auto-regressive (AR(1)) model, estimated a 3:1 ratio for the power of the white noise component to that of the colored noise component in their model for fMRI noise time-series for $TR = 2$ sec. The second prescription for treating the underlying noise structure is called pre-coloring. In this method (86) the fMRI time-series (with unknown intrinsic color) is swamped with a known amount of auto-correlation by smoothing with a Gaussian filter. The time-series is then analyzed with the assumption that it is WSS Gaussian with a pre-determined auto-correlation function (ACF). The third noise-treatment method (82, 87) relies on pre-

whitening the time-series before analysis. This involves estimation of the color by autoregressive moving average (ARMA) time series analysis.

The presence of a dominant white noise component makes estimation of the color of the time-series particularly difficult (88). One can take recourse to the frequency domain and try estimating the color using non-parametric spectral analysis (67, 89). However spectral estimation involves an inherent trade-off between bias and consistency of the power spectrum estimate (88). Gopinath et al. (90) proposed a technique to overcome the obstacles in conventional methods of frequency domain FMRI signal analysis. Using a result from statistical signal processing (91), for broadband signals in noise of unknown power spectral densities (provided WSS), the authors demonstrated that judicious design of event-related FMRI experiments can result in broadband hemodynamic response signals in FMRI time-series. In such a case, only an estimate of the power spectrum is needed to construct a detector for broadband FMRI signals in unknown colored FMRI noise time-series, without the need for exact determination of the color of the noise.

The preceding discussion has focused on the stochastic properties of FMRI noise. In practice, the changes in FMRI signal due to physiological processes like cardiac and respiration are also included in the noise term (92). Techniques have been introduced (93-94) to correct for the noise introduced by physiological processes. For whole-brain FMRI studies with long TR (~ 2 sec) the respiration and cardiac noise components are not very significant (95), especially when the stimulus order is aperiodic and are hence ignored.

The origin of FMRI noise is of interest. If the features in the noise can be ascribable to physical/physiological process(es) the task of FMRI signal analysis would be

simplified. Some groups (44, 87) have suggested that the low frequency features of the fMRI noise are related to physiological sources like resting state neural activity. Others (67, 96) are skeptical, pointing to the fact that disproportionate spectral power at low frequencies has been observed in phantoms and cadavers also. Recently Gopinath et al. (97) showed that some regions in the brain which exhibited “1/f-like” features in the image-magnitude fMRI noise time-series also exhibited similar behavior in the image-phase fMRI noise time-series. These findings would also preclude resting state neural activity as a source of the color in fMRI noise as the neuro-vascular coupling which relates neural activity to the BOLD signal at the capillary level does not leave a signature in the voxel-phase. Gopinath et al. also showed (98) presence of more voxels exhibiting disproportionate spectral at low frequencies ($f < 0.01$ Hz) in diseased brain tissue than intact brain tissue; a finding difficult to reconcile with the resting state neural activity as a source of “1/f” fMRI noise, since there is significantly less neural activity in diseased tissue when compared to healthy brain tissue.

Parametric Methods and General Linear Model

The first attempts at fMRI data analysis utilized parametric methods (43, 44). Most parametric methods can be expressed in the form of General Linear Models (GLMs). The brief review of fMRI signal processing presented here will focus on deconvolution analysis under the framework of a GLM. This is also instructive in that it is the main method of analysis followed throughout this thesis. This method (99, 100) relies on the assumption that the observed fMRI time series, $Z(t)$ is the result of a convolution of the applied task stimulus-impulse time-series, $f(t)$ and the impulse response function (IRF) $h(t)$. This signal is over and above a baseline and is in the

presence of a Gaussian white noise process $\varepsilon(t)$. In the discrete-time domain indexed by n ,

$$Z_n = \beta_0 + \beta_1 n + \sum_{m=0}^p h_m f_{n-m} + \varepsilon_n \quad [2.5]$$

$$n = p, p + 1, \dots, N - 1$$

where β_0 and β_1 are the baseline parameters (corresponding to mean and linear trend) and the summation denotes the discrete-time finite-lag convolution of the $f(t)$ and $h(t)$ over p lags and N is the number of time-points in the time-series. The baseline of FMRI time-series often exhibit a global linear or polynomial drift and have to be included in the model for optimal signal detection and estimation. The constant p is determined by the duration of the anticipated hemodynamic response function (HRF). In matrix formulation [2.5] becomes

$$\mathbf{Z} = \mathbf{X}\boldsymbol{\beta} + \boldsymbol{\varepsilon} \quad [2.6]$$

where \mathbf{Z} is the observed time-series vector, \mathbf{X} is the deconvolution matrix and $\boldsymbol{\varepsilon}$ is the white noise matrix. The linear regression problem expressed by equation [2.6] can be solved for estimates of \mathbf{Z} and $\boldsymbol{\beta}$, $\hat{\mathbf{Z}}$ and $\hat{\boldsymbol{\beta}}$ by minimizing the error sum of squares between the estimated (fitted) time-series and observed time-series:

$$SSE = Q(\hat{\boldsymbol{\beta}}) = \sum_{i=0}^{N-1} (Z_i - \hat{Z}_i)^2 \quad [2.7]$$

which gives the least squares estimate for $\hat{\boldsymbol{\beta}}$ through

$$\hat{\boldsymbol{\beta}} = (\mathbf{X}^T \mathbf{X})^{-1} \mathbf{X}^T \mathbf{Z} \quad [2.8]$$

The parameter vector $\hat{\boldsymbol{\beta}}$ is composed of the estimated parameter for the mean ($\hat{\beta}_0$), linear trend ($\hat{\beta}_1$) and the IRF parameter estimates ($h_0 \dots h_p$).

The significance of the regression can be evaluated by constructing the following hypothesis test,

$$\begin{aligned}
H_0 : Z_n &= \gamma_0 + \gamma_1 n + \varepsilon_n \\
H_a : Z_n &= \beta_0 + \beta_1 n + \sum_{m=0}^p h_m f_{n-m} + \varepsilon_n
\end{aligned} \tag{2.9}$$

where H_0 and H_a are the null and alternate hypothesis (same as equation [2.5]) respectively and γ_0 and γ_1 are the parameters corresponding respectively to the mean and linear trend of the noise (baseline) model. A test of the null hypothesis is made by determining the parameters which yield a least squares fit for the baseline model as well as the parameters that provide the least squares fit for the signal plus noise (full) model of H_a . Next the residual sums of squares between the observed time-series and the fitted time-series for the baseline model, $SSE(B)$ and that of the full model, $SSE(F)$ are evaluated. The null hypothesis can then be tested through the test statistic F^* ,

$$F^* = \frac{MS(\text{regression})}{MS(\text{error})} = \frac{\frac{SSE(B) - SSE(F)}{df_B - df_F}}{\frac{SSE(F)}{df_F}} \tag{2.10}$$

where df_B and df_F are the degrees of freedom of the baseline model and full model respectively given by

$$\begin{aligned}
df_B &= N' - 2 \\
df_F &= N' - 2 - (p + 1) \\
df_B - df_F &= p + 1
\end{aligned} \tag{2.11}$$

where $N' = N - p$ is the number of usable data points. The test statistic F^* has the $F(df_B - df_F, df_F)$ distribution under the null hypothesis. The coefficient of multiple determination, R^2 , can be used as an indicator of the goodness of fit between the full model and the data, as given by

$$R^2 = 1 - \frac{SSE(F)}{SSE(B)} \tag{2.12}$$

and can be regarded as the proportion of the variation in the data that is explained by the full regression model.

Inference

Once a statistical parametric map of voxels in the brain is obtained, the next step is to decide how to threshold the data, in order to be able to say a certain voxel (or area of the brain) is activated at a given level of significance (p -value). This task is complicated by the multiple comparison problem. Typically, for a whole brain fMRI study with resolution $\sim 3\text{ mm}$, a large number of voxels ($\sim 40,000$) are tested simultaneously for rejection of the null hypothesis. Thus, even with a p -value of 0.01, one can end up with a significant number (~ 400) of false positive voxels, which get declared active, assuming all the voxels are independent. The simplest procedure to control for multiple comparisons is the Bonferroni correction (101). Here, for a desired significance threshold, p , the voxels are declared active if they possess p -values less than p/N , where N is the number of voxels in the map. This procedure can be considered overly conservative (102), even in the case where all the voxels are independent (as is not the case in fMRI), and can lead to loss of power (declaring voxels to be inactive when they are active). Recently, some groups (102, 103) have advanced a less conservative procedure for controlling multiple comparison false positives. Instead of correcting the family-wise error rates (FWER), as is done in Bonferroni correction, they control for the false discovery rates (FDR), the proportion of false positives. FDR theory (102,103), also allows for non-independent voxel families, as opposed to the Bonferroni method, where one has to estimate the number of independent voxels.

In practice, a lot of groups do not control for multiple comparisons, opting instead to threshold the data at low p -values. This procedure is surprisingly effective at the individual subject level. The reason can be surmised as follows; at conventional fMRI sites, with $B_0 \sim 1.5\text{-}4\text{T}$, even the relatively small magnitude of BOLD signal changes of 3-

10 % lead can to very low p -values in support of the null hypothesis, in the regions of interest. Thus, the SPMs are thresholded at high levels of significance, erring if anything on the side of specificity. In fact, when estimation of the HRF is also critical to the analysis over and above the detection of activation, one might need to threshold the SPMs at a higher level of significance, in order to eliminate voxels whose estimated IRF (or HRF) is not well defined. Figure 2.2 shows the IRF for a voxel with $F(16,470) = 30$ as well as a voxel with $F(16,470) = 2.5$, for an event-related silent word generation study (90). Although the $F = 2.5$ voxel is significant at $p < 0.001$, the corresponding IRF is not well defined unlike that of the $F = 30$ voxel. The signal in the figure has been normalized to a unit maximum to show the shape better. The voxel IRF on the right has a substantially lower raw amplitude compared to the one on the left. The post stimulus undershoot seems pronounced in the voxel (from the auditory cortex) hemodynamic response on the left. The distribution of the test statistic can vary between subjects and also between different sessions of the same subject (104, 105). Thus, it may be beneficial to threshold each session separately and use procedures like conjunction analyses (106) to make between-session inferences.

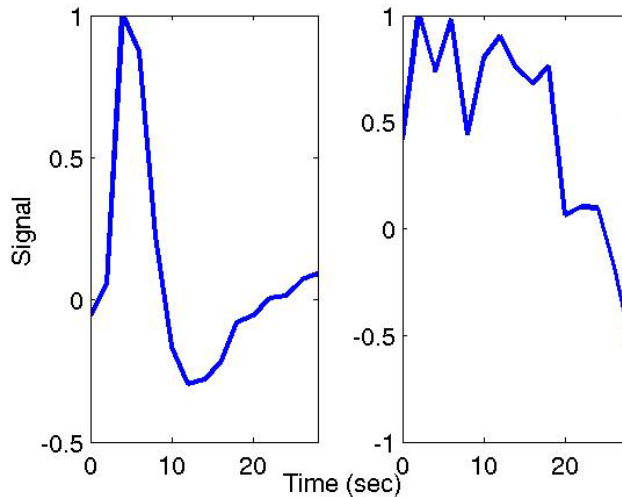


Figure 2.2: The estimated impulse responses for a auditory cortex voxel activated at $F(16,470) = 30$, $p\text{-val} \approx 0$ (left) and a voxel with $F(16,470) = 2.5$ (right). The signal has been normalized to a unit maximum.

ROC Analysis

Receiver operating characteristics (ROC) curves are used to test the performance of a detector, imaging modality, or technique (107). The application of ROC analysis to test different image processing techniques, statistical data analysis methods, preprocessing steps prior to statistical analysis, and experiment design in FMRI has been attempted by a few groups (90, 108, 109, 110, 111). Ventures into ROC analysis have consisted of using synthetic data (90, 110, 111) or real data under test-retest conditions (108, 109). The major drawbacks in using synthetic data are the hitherto incompletely understood nature of the noise structure in FMRI time-series as well as the unpredictability of the BOLD FMRI signal (84, 104, 105). The problem with using test-retest methods is the unpredictable variations between sessions in the BOLD signal (104-105) as well as the multivariate nature, within session, of the BOLD signal change (84).

CHAPTER 3 MOTION AND FMRI

The artifacts produced by subject motion are a major confound in the analysis of functional magnetic resonance imaging (fMRI) time series data. In this chapter the major sources of motion-related artifacts in fMRI time series are described. Some of the existing methods for dealing with motion artifacts in the literature are also reviewed.

Introduction

fMRI signal changes are of the order of 1-8% of the baseline signal intensity in conventional MR systems (1.5T and 3T). As a result, it is very important that the signal changes from sources other than functional activation be eliminated as far as possible. In living subjects, movement is unavoidable. Even small motions can impact the fMRI time series adversely. For instance (75 Cox, et al., 1999), it has been seen that typical T_2^* -weighted brain images show 10-20% intensity changes between adjacent voxels in the parenchyma and 70-80% changes at the edge of the brain. Thus, motions of the order of a tenth of a voxel can produce 1-2% signal changes in the parenchyma and 7-8% signal change at the edges of the brain, of the same size as changes occurring from brain activation that are to be detected. For a 20 cm field of view (FOV) 128 X 128 image the above statement implies that motions of the order of 150 μm can have a significant impact on the fMRI signal. Motion can impair the detection of real functional activation in several ways. Random motions of the subject will appear as additive noise in the voxel time-series and decrease the detectability of functional activation. Stimulus-correlated

motion can mask real activation in cortical regions and also appear as false-positive activation in the brain edges and high-contrast regions of the brain.

Proper image registration (aligning the time series images) is imperative to minimize the effect of motion on the fMRI signal. As mentioned in *Chapter 2*, conventional intensity-based image registration methods consist of two steps (75-77). The first step is the estimation of the rotation and translation parameters required to align a given image with the base image. The second step is the assignment of intensity values to the voxels in the rotated image grid. Motion artifacts can creep into the time-series from errors encountered in both of the above steps, i.e. misalignment or misinterpolation. Grootnik et al. (112) have characterized the artifacts introduced into the time-series by intensity-based image-registration methods using a brain phantom. They attribute these artifacts to interpolation errors introduced by the resampling inherent within realignment. Most intensity-based methods fail when the motion is large - more than a voxel (75). Feature-based methods (80-81) use features in the image as landmarks in the registration method. These methods, however, need the identification (or segmentation) of some feature which is not always possible in low resolution fMRI images.

Often this is the only motion correction step performed in fMRI studies. However, it would be optimal if image registration were but a first step in the treatment of motion artifacts in fMRI. As mentioned before, conventional image registration programs can give rise to unintended errors.

Major Sources of Motion Artifacts and Deterministic Solutions

In fact, even after perfect alignment of the time-series, the deleterious effects of motion on the fMRI time series persist to some extent. These effects can be due to a

number of sources. The following paragraphs will point out the major sources of motion-related artifacts and review the methods that exist in the literature to treat them.

Static Magnetic Field Effects

Head motion in inhomogeneous magnetic field causes local distortions in the static magnetic field (B_0), which are not unwarped in standard image-registration schemes. Ideally, the B_0 field should be homogeneous throughout the sample (head). This is hard to achieve in practice since the head distorts the magnetic field (113). To a certain extent the B_0 field can be made homogeneous by adjusting the current in the shim coils. The shim field will depend on the orientation of the head with respect to the B_0 field. The shim fields are set up before the acquisition of the images. Residual inhomogeneities which exist after the shimming will be modulated by head motion, producing time-dependent magnetic field distortions. Consequently there will be a non-zero field difference between the before-movement and after-movement-after-realignment images, for a given point in the sample. Jezzard et al. (113) demonstrated this by acquiring phase images in addition to magnitude images with an echo planar imaging (EPI) sequence while a controlled flexion of the subject's head was performed. They showed that even after re-alignment a substantial field difference existed between the "before motion" and "after motion" images. Even a 1° rotation will result in local distortions of the order of one pixel. Quantitatively, the resonant frequency of the 2D FMRI image at a point, in the absence of magnetic field inhomogeneities, is given by

$$\omega(x, y) = \omega_0 + \gamma(G_x x + G_y y) \quad [3.1]$$

where $\omega_0 = \gamma B_0$, is the central frequency, γ -being the gyromagnetic ratio (42.575 MHz/T). The presence of magnetic field inhomogeneities leads to introduction of a spatially varying off-resonance (8H, 113, 114) term into equation [3.1] which becomes

$$\omega(x, y) = \omega_0 + \gamma(G_x x + G_y y) + \Delta\omega(x, y) \quad [3.2]$$

where $\Delta\omega(x, y)$ is the off-resonance term. The off-resonance has different effects on different methods of image acquisition used in FMRI. In EPI, where the k-space data is acquired in rectangular fashion, the off-resonance causes geometric distortion. The spatial encoding, which depends on the resonant frequency, is compromised, resulting in pixels being mis-located. In spiral imaging, where the k-space is acquired in a spiral fashion, the off-resonance causes blurring. In FMRI, magnetic field environment at a point can differ from image-to-image due to motion. This time dependence will manifest as apparent noise in the FMRI time-series.

Some remedies have been proposed to ameliorate this effect. Jezzard's group (113), working with EPI data, pointed out that the off-resonance term can be calculated by

$$\Delta\omega(x, y) = \Delta\phi(x, y) / TE \quad [3.3]$$

where $\Delta\omega$ is the field distortion caused by motion and $\Delta\phi$ is the phase difference between the given image and the first image, x and y specify the in-plane Cartesian coordinates of the position and TE is the echo-time. Thus, the pixel-shifts can be calculated from a temporal sequence of phase images and corrected. This method assumes that off-resonance of the first image is either negligible or is corrected by other methods. Also, this method is applicable to EPI FMRI but not to spiral FMRI.

The manifestation of off-resonance related artifacts is different in spiral imaging. The off-resonance leads to blurring in spiral images (114-115). In conventional spiral reconstruction programs the off-resonance due to field inhomogeneity is calculated by constructing a field map for the first image in the time-series. All the images are then reconstructed by incorporating the phase conjugate of the inhomogeneity dependent phase error in the kernel of the Fourier transform. All the images in the time series are deblurred using the off-resonance term of the first image. However, in the case of motion, just like in EPI, an analogous method to perform time dependent off-resonance deblurring in spiral imaging is needed.

It must be stressed that these methods will only correct for geometric distortions (in the case of EPI) and blurring (in the case of spiral) images. The signal loss due to dephasing within voxels cannot be recovered. The extent to which the time-dependent distortions affect the fMRI time series has not been studied. It would be desirable to look at the effects of the distortion correction in order to assess their significance.

Ward and collaborators (116) have looked at the feasibility of real-time auto-shimming, wherein they compute the change in magnetic field due to motion in real-time and correct the shim by applying compensating gradients accordingly. The changes in magnetic field due to motion are measured by a navigator pulse sequence. The advantage of this method is that it compensates for the magnetic field distortions at image acquisition, which is more desirable since this could also alleviate the intravoxel signal dephasing that occurs due to the inhomogeneities. Post-processing methods have to work with the irreversible loss of signal that occurs due to increased inhomogeneity. The main drawback of this method is that it can only compensate for first-order changes in the

field. The susceptibility artifacts which cause the most dephasing involve inhomogeneity gradients of higher order. Thus the need for a post-processing off-resonance compensation method will still exist. There is also the practical difficulty that not all FMRI centers have access to hardware and software needed for pulse-sequence-based correction methods.

Spin History Effects

In conventional 2D multi-slice multi-excitation image acquisitions encountered in FMRI, the signal or magnetization from a small volume of the object will depend on the interaction of the B_0 field with the slice-selective RF electromagnetic field B_1 (117-118) and the recovery of magnetization due to longitudinal relaxation during TR. The electromagnetic field environment will change considerably with small displacements of the sample (head) around the inferior and superior edges of an axial slice, the right and left edges of a sagittal slice and the anterior and posterior edges of a coronal slice. Thus even small motions of the order of a few mm in a plane orthogonal to that of the image will result in a different magnetization from one excitation to the next. This effect will be considerable in cases where the recovery of longitudinal magnetization is incomplete between two excitations (which is the case when the TR is comparable to T_1 as is the case in FMRI). Thus the signal from a given volume is a function of its current position as well as its spin excitation history. It should be noted that post-hoc image registration of the images cannot compensate for intensity anomalies caused by this effect. Retrospective correction for through plane motion effects on signal intensity would require detailed knowledge of a number of physical properties, such as the spatial variation of relaxation times within the head, a seemingly intractable problem at best, unsolvable at worst. Prospective image acquisition correction methods offer the best solution for through-

plane motion. Two such methods have been proposed. One method (119) estimates the motion parameters from one image to the next by conventional image registration schemes. This is done in real-time and the slice gradients are upgraded accordingly such that the measurement coordinate system is kept at a fixed orientation relative to the patient's head during the scan. Thus, in principle, the motion artifacts caused by spin history disruptions can be alleviated. The main drawback of this method is that due to constraints of computing power and gradient hardware requirements, the gradient upgrade interval is currently limited, leading to whole-brain TR of 3-4 seconds or more. Thus, the temporal resolution offered is not sufficient for most current fMRI needs. Another method that has been proposed (120-121) measures the inter-image head motion by employing navigator pulses. The slice gradients are subsequently updated real-time, enabling the relative orientation of the head and the measurement co-ordinate system to remain fixed during the scan. The main drawback of this method is that it takes up to 160 msec per slice, thus requiring a gradient upgrade interval and hence TR of 4 sec or more for a whole-brain study. This is not sufficient for most current fMRI studies. It would be better to use faster methods of encoding motion, such as an optical monitoring device, independent of MR signal acquisition, which would lead to faster update times and improved motion correction.

Inter-Shot Motion

Often, in fMRI studies, it is desirable to use a multi-shot spiral/EPI sequence to have enough spatial resolution to attenuate the signal drop-offs in high susceptibility contrast regions, or to resolve small anatomic features such as cortical columns or to study physiological mechanisms. For whole-brain study, image TR of the order of 2 seconds is the norm. Thus the time between the two shots for a given slice in a 2D-

acquisition sequence is about 2 seconds. In multi-shot spiral imaging, the motion that occurs in between the shots leads to inconsistencies in the collection of the k-space data (115, 19). Inconsistencies in the low spatial frequencies leads to intensity distortions in the image. Inconsistencies in the high spatial frequencies leads to swirl like patterns in the image (Figure 3.1).

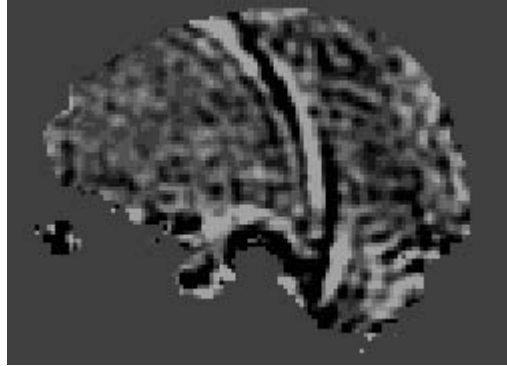


Figure 3.1 Two-shot spiral FMRI time series image of a mid sagittal slice showing swirl-like patterns arising from inter-shot motion. The image has been detrended of its time-series mean to better portray the effects of motion.

In FMRI these motion-induced signal variations may fluctuate from image to image in the time-series, leading to increased variance in the voxel time-series, thereby decreasing the ability to detect brain activation. Low frequency image intensity distortions can be treated by the application of navigator techniques (92-122) or k-space regression (93) to ensure that all the interleaves of a multi-shot spiral image have the $k = 0$ point common. Essentially these methods force the $k = 0$ point in the k-space to have the same magnitude and phase in all the shots. Since low spatial frequencies contain most of the information related to image intensity, these methods succeed in minimizing the image distortions due to motion. These methods are aimed primarily at decreasing the effects of physiological fluctuations, which tend to cause global signal intensity changes.

Higher spatial frequencies do not contain much intensity information. Thus the methods to eliminate low frequency intensity modulations due to physiological fluctuations ignore high k-space inter-shot inconsistencies. However, subject motion between shots does lead to swirl-like patterns in the image due to high k-space fluctuations. These swirls vary from image to image depending on the motion. This manifests as additive noise in the FMRI time series. Oftentimes these motions are also stimulus-correlated, which increases false positives and can also mask real activation. This adds extra constraints in designing FMRI experiments. Researchers are often forced to settle for low-resolution one-shot spiral images for studies like overt word generation, which involve significant motion. In order to attenuate the high frequency artifacts in FMRI images acquired with a 2-shot spiral sequence; it is useful to understand the origins of the artifact. Suppose, in the time TR elapsed between the acquisition of the first and second shots, the image rotates by an angle, θ , about the axis normal to the image plane. Then the image space as well as the k-space of the second shot needs to be rotated by the amount $-\theta$ in order for the two acquisitions to be aligned. If the image space of the second shot is translated by a distance, Δr , given by

$$\Delta \bar{r} = \Delta x \hat{i} + \Delta y \hat{j} \quad [3.4]$$

with respect to that of the first shot (where Δx and Δy are the translations along the two orthogonal axes, denoted by unit vectors, \hat{i} and \hat{j}), then by the Fourier shift theorem, every point on the k-space accrues a phase, ϕ_k given by

$$\phi_k = \bar{k} \cdot \Delta \bar{r} = k_x \Delta x + k_y \Delta y \quad [3.5]$$

Thus, in order to reconstruct the image properly, the data-points in the k-space matrix acquired with the second shot need to be multiplied by a phase term, $e^{ik \cdot \Delta r}$. It is obvious

that the prescribed method is limited to in-plane motion corrections. This is because the image acquisition is in 2D and there is no phase encode along the third cardinal axis. The extent to which the k-space distortions produced by inter-shot motions affect the FMRI time series has not been studied. It would be desirable to look at the effects of the distortion correction in order to assess their significance.

Remarks

The methods mentioned up till now are deterministic in the sense that they isolate the cause of different motion-related artifacts and then correct for them. They are mutually exclusive in that ideally all the three different classes (off-resonance distortion compensation, spin-history correction and inter-shot motion correction) should be performed to properly detrend motion-related noise in the FMRI time series. The order of the execution of the steps is also important. Obviously prospective methods used during image acquisition should be performed before applying retrospective correction methods. The relative importance of these methods depends on the FMRI protocol used. For example, if one-shot imaging methods are used, the high spatial frequency related artifact would hardly be an issue. Also if the task (e.g. overt word generation with coronal/sagittal acquisition) were such that the motion is mainly in-plane, off-resonance correction would be more important than spin-history effects.

Mechanistic Solutions

Another class of methods can be employed to reduce noise associated with motion in the FMRI time-series. These methods are mechanistic in the sense that they do not explicitly attempt to account for the physical processes that relate motion to the artifactual noise produced. They endeavor to phenomenologically model the signal changes in the FMRI time series due to motion and separate out or detrend the motion-

related signal changes from the BOLD signal changes. These artifacts could arise from any of the motion-related sources mentioned in the previous section.

Motion Parameter Regression

Friston and collaborators (117) proposed a method to account for motion artifacts in the fMRI time-series. They posit that the movement related effects can be divided into those that are a function of the position of the object in the frame of reference of the scanner in the current scan and those that are due to movement in the previous scans. The first component is posited to include changes in signal intensity as the position of the voxel changes with respect to inhomogeneous background magnetic field (e.g. susceptibility induced high image contrast boundaries) as well as signal changes due to displacements around the slice boundaries in the slice excitation direction, which result in changes in the RF excitation profile. The second component is theorized to reflect the signal fluctuations due to changes in the spin excitation history, which are caused by movement in the previous scans. Invoking arguments which pin the dependence of motion-related signal changes on first-order perturbations of the longitudinal magnetization arising from movement in present and previous scans, they argue that artifactual motion-related signal changes at a given instant can be modeled with a second order polynomial in the displacements of the object in the present and the preceding scans in the fMRI time-series. The displacements are encoded by the estimated motion parameters in the re-alignment of the present and preceding scans to the last scan of the fMRI time-series. The signal time series can be written as

$$S_t = \sum_{i=1}^6 a_{it} (\delta x_{it}) + b_{it} (\delta x_{it})^2 + \sum_{i=1}^6 a_{it-1} (\delta x_{it-1}) + b_{it-1} (\delta x_{it-1})^2 + Y_t \quad [3.6]$$

where S_t is the signal at time t , δx_{it} is the value of the estimated motion parameter of the x_i^{th} of the six degrees of freedom in the rigid body realignment of the t^{th} scan to the last scan of the fMRI time-series, a_{it} and b_{it} are coefficients to be estimated by ordinary least squares along with the model parameters of Y_t , the part of the fMRI time-series free of motion-related signal changes through a multiple linear regression procedure.

There are some drawbacks to this approach of motion artifact reduction. The model assumes that head motion affects all the voxels in a similar linear fashion. It has been noted that fMRI voxels on brain-edges and high-contrast boundaries are much more sensitive to motion than voxels away from such features (118, 123, 124, 125, 126). Also the model assumes that the movement-related signal changes are independent of hemodynamic brain activation signal changes. Bullmore and collaborators (118) demonstrated that this last assumption is violated by stimulus-correlated motion. In such cases they also demonstrated that Friston's correction (117) can reduce the power of detecting true-positive brain activation voxels.

Finally, equation [3.6] assumes that most of the signal changes due to motion arise from spin-history effects. Stimulus-correlated motion in overt word generation experiments have been shown to cause susceptibility-induced magnetic field changes (123-125). The resulting signal changes in the fMRI time-series are an order of magnitude larger than movement-induced spin-history signal changes and may not be linearly dependent on the motion parameters. Regardless, this method of motion correction enjoys widespread acceptance.

Stimulus-Correlated Motion

Some fMRI paradigms require overt word generation in response to auditory or visual stimuli (127, 128). Speech involves movement of pharyngeal muscles, especially

tongue and jaw, which have been demonstrated to change the susceptibility-induced magnetic field distribution of the brain (124). The greatest magnetic field changes due to speaking occur in the inferior and frontal regions of the brain, decreasing rapidly towards the superior and dorsal edges. The changes in the magnetic field cause pixel shifts in EPI FMRI time-series images (113) and blurring in spiral FMRI time-series images (114). The effects of pixel-shifts (or blurring) are more pronounced at the brain edges and other high image contrast boundaries, where large spatial gradients in image intensity exist. Voxels at these regions may exhibit as much as 100 % stimulus-correlated signal changes. Thus, after statistical signal processing they might show false positive activation with statistical significance similar to or higher, than voxels exhibiting BOLD signal change.

These changes in magnetic field can occur even if the part of the head being imaged is perfectly still. In fact, Yetkin and collaborators (123) found changes in the magnetic field distribution of a homogenous copper sulfate (CuSO_4) solution phantom when a separate CuSO_4 solution phantom was moved in its vicinity but outside the field of view (FOV) of the RF coil. Thus signal changes due to speech-engendered stimulus-correlated motions (SCMs) will not be compensated by conventional image registration algorithms (75-77). Also SCM associated with speech can be dependent on what is generated overtly. For instance, Birn observed (124) that the generation of the word 'one' caused almost double the change in the magnetic field distribution when compared to the word 'two' for a normal human control brain at $B_0 = 1.5T$. Thus methods involving motion-parameter-regression (117) also may not adequately correct for SCM signal changes associated with overt word generation. This is because such methods assume a

linear relationship between motion and corresponding signal changes and are also predicated on the assumption that most of the signal changes due to motion are due to changes in the spin-excitation history and not local magnetic field distribution changes.

SCM-Ignoring Images

The major portion of signal changes due to speech-related SCM occurs in the first 4 or 5 seconds after speech (124-125). The BOLD hemodynamic response to cognitive processes typically exhibit a delay of 3-6 seconds before onset and the peak is reached only after 4-6 seconds after that (30). Thus, assuming one is interested in studying the brain activation signal changes subsequent to overt production, the inherent difference in the time scales of BOLD and SCM-related signal changes can be used to mitigate the effects of SCM. This argument has been used by certain groups (127-128) to ignore (127) or screen using temporal phase (128) signal changes during the first few images after speech. This method may not be optimal if there is a significant overlap between the time-courses of SCM and BOLD related signal changes (125, 129). In FMRI studies involving patients with language deficits, the time lag between stimulus delivery and overt production can be much longer and more unpredictable than in controls (130). For these cases patient response-locked data analyses are more suitable than language-stimulus-cue-locked timing (131). In such cases, ignoring (or screening) images after speech can lead to sub-optimal detection and estimation of BOLD signal changes, especially in brain regions where the cognitive processes start before overt production.

With respect to ignoring a few images after overt word generation, there is also the caveat that for whole-brain FMRI with nearly isotropic voxels, the imaging constraints restrict the minimum allowable TR to between 1.5 and 2 seconds. Consequently the desirability of imaging the complete BOLD HRF might necessitate adoption of a protocol

where only one or two images after enunciation are ignored (screened). This length of time may not be sufficient to eliminate all the effects of SCM.

SCM-Detrending

As mentioned before the voxels most affected by the SCM lie on the brain edges and other high-contrast boundaries. Birn and collaborators (125) performed single event fMRI studies of speaking, swallowing, jaw clenching and tongue movement and found SCM-related signal changes at voxels near the brain edge of similar statistical significance to BOLD activation voxels in the areas of motor cortex involved in the above-mentioned tasks. They found that orthogonalizing all the voxel time-series in the fMRI dataset with respect to SCM signal changes resulted in functional activation maps with reduced SCM artifacts.

This method is sensitive to the time evolution of the SCM-related and hemodynamic responses. If the BOLD HRF and the SCM signal changes are not well resolved, the application of this method has been shown, by our group (129) to result in loss of sensitivity for detecting brain activation. This situation can arise, for example, at voxels in brain areas responsible for preparation for the word generation task. fMRI studies of patients with language deficits require adoption of a data analysis protocol based on patient responses. The time lag between stimulus delivery and patient response is much greater in such patients. Use of a non-selective global detrending procedure as described above (125) can result in loss of information about brain processes related to preparation of the overt response in such cases.

Other Mechanistic Methods

There are a few other methods for dealing with stimulus-correlated motion in fMRI time-series. Some authors have argued that the SCM artifacts can be somewhat

idiosyncratic and vary across individual participants (118, 127). Thus the effects of the SCM will be mitigated if the fMRI data are averaged across a group of participants. This method may not have the generalized applicability it is purported to possess (118, 127).

Salvador and collaborators (126) have suggested that masking all activated voxels which lie on regions of high image intensity gradients. This method can have the effect of eliminating cortical activation along with SCM-related activation since a significant amount of cortical regions in the brain lie near high-contrast boundaries.

CHAPTER 4 TASK CORRELATED MOTION NOISE REDUCTION METHODS

In this chapter a new selective detrending method for reducing noise due to stimulus-correlated motion in FMRI time-series of overt word-generation paradigms is advanced. A framework is introduced to evaluate this method as well as compare its performance with three other methods of SCM-related artifact reduction in event-related overt word-generation FMRI paradigms: 1) motion parameter regression (117, 118), 2) ignoring images during speech (127) and 3) non-selective detrending (125). Since there is generally a significant delay between the presentation of neuronal stimulus and the performance of a overt word generation task among patients, the speech-related artifacts in the FMRI time-series should be more appropriately termed task-correlated (instead of task-correlated). Also, since the patients' and the control subjects' data analysis are presented in the same framework the term task-correlated motion (TCM) will be adopted instead of the term more commonly used in FMRI literature, stimulus-correlated motion (SCM).

Selective Detrending

Task-correlated motion due to movements involved in verbalizing lead to significant changes in the FMRI signal (123-125). These artifactual increases/decreases in signal intensity are manifested as false-positive activations in high contrast boundaries in or outside the brain. Since the origin of signal changes due to speech related TCM is mainly attributed to susceptibility profile fluctuations, the shapes of the time courses of the signal changes in the brain due to speech-related TCM and of the signal evolution at

high-contrast boundaries characteristic of large magnetic susceptibility gradients should have some similarities (123-125). Thus it should be possible to adequately represent most of the TCM-related signal changes in the dataset with the signal changes from a few representative voxels selected from high contrast boundaries outside or on the brain. The signal changes due to speech-related TCM in all affected voxels should be representable as a whole or in part by the selected set of voxels.

The method of Birn et al. (125) detrends all the voxel time-series in the FMRI dataset of components proportional to all the selected TCM voxel time-series, using a linear least-squares method. This has the undesirable effect of detrending brain activation related BOLD MR signal along with TCM-related signal in voxels where the BOLD signal has a significant overlap with net TCM-related signal change of all chosen TCM voxels.

The selective detrending method introduced here endeavors to overcome this drawback by examining voxels for TCM-related signal changes and performing the detrending only if certain criteria (developed to maximize false-positive TCM noise reduction as well as true-positive BOLD signal retention) are satisfied. It would be remunerative to recall that the magnetic field changes due to speech-related TCM are strongest in the inferior-frontal regions of the brain and decrease rapidly along the inferior-superior direction as well as anterior-posterior direction (124). Thus, detrending all voxels, non-selectively, of components proportional to all the representative TCM time-series will tend to be overly conservative. A more attractive approach would be to examine each voxel for presence of significant corruption due to task-correlated motion (as characterized by the representative set of TCM time-series) and detrend selectively.

Both the non-selective detrending method as well as the method of ignoring images have the potential to decrease the significance of activation of true-positive BOLD MR voxels along with the false-positive TCM corrupted voxels. There are two instances when this situation can arise. The first case is encountered in voxels which do not exhibit a significant delay to onset in their hemodynamic response. There is some recent literature citing that voxels exhibiting capillary BOLD activation localized to brain activation sites exhibit smaller delays while voxel HDRs having a significant venous BOLD component tend to have a more delayed and sluggish response (132). The second situation arises in language FMRI paradigms in aphasic patients using subject response-locked stimuli. Since aphasia patients, before therapy, tend to exhibit long pauses of up to 10 seconds before generating a word to a semantic cue, the BOLD signal changes driven by the brain processes involving response preparation may significantly overlap with subject response correlated speech related TCM signal changes.

Thus a good detrending procedure should have the property of decreasing TCM signal changes as much as possible while leaving BOLD MR signal changes largely intact. This can be accomplished by selecting an adequate set of (phase offset) BOLD MR signal change voxels, examining each voxel time-series for presence of BOLD MR signal changes characterized by the representative voxels, and taking care not to decrease the BOLD component in them if and when selective detrending is performed on them. The next section describes the implementation of the detrending procedure.

Selective Detrending: Methods

In this section the methods used in the application of the selective detrending to reduce TCM noise in event-related overt FMRI paradigms in controls as well as patients

will be explained. The paradigm is slightly different for aphasia patients due to their inability to generate words fluently.

Subjects and Task

Two aphasia patients (one female and one male: ages 60 and 70) with left hemisphere stroke were scanned twice, once before rehabilitation therapy and once after therapy. This yielded four fMRI datasets to which the noise reduction methods could be applied. The patients performed an event-related overt word-generation task, for which they were asked to provide single-word responses to semantic category cues. The inter-stimulus interval between category cues was 24.9, 26.6, 28.2 or 29.8 sec, corresponding to 15, 16, 17 or 18 images, assigned in a pseudo-random manner. The patients underwent rehabilitation treatment in between the pre- and post-therapy scans. The rehabilitation treatment was designed to engage right-hemisphere intention mechanisms to facilitate word finding and consisted of patients naming pictures shown on a computer monitor, under the tutelage of therapists.

In addition to the aphasia patients, four healthy control subjects (three female and one male: ages 50-70) were also scanned with a similar event-related overt language fMRI paradigm. The subjects were asked to provide single-word responses to semantic category cues. The inter-stimulus interval between category cues was 16.6, 18.3, 19.9 or 21.6 sec, corresponding to 10, 11, 12 or 13 images, assigned in a pseudo-random manner.

Image Acquisition

For patients, low resolution functional MR images were obtained using a 1-shot forward spiral sequence (18). Thirty-two 4-4.5 mm thick sagittal slices covering the whole brain were acquired. The repetition-time (TR) was 1660 msec, the echo-time (TE) was 18 msec, the flip angle (FA) was 70° and the field of view (FOV) was 200 mm. The

image matrix size after interpolation was 64 x 64 and spatial resolution was 3.1 mm x 3.1 mm x 4-4.5 mm. Five functional runs were acquired with 161 images in each run, 1.66 sec per image. For anatomic reference, a high resolution T1-weighted 3D spoiled gradient recalled (SPGR) sequence was acquired with scanning parameters: 240 mm FOV, 256 x 256 image matrix, 0.9 mm x 0.9 mm x 1.3 mm resolution, TR = 23 msec, TE = 7.7 msec and FA = 25°. For angiographic reference, a 2D SPGR time-of-flight (TOF) MR angiogram was obtained with scanning parameters: 200 mm FOV, 256 x 256 image matrix, 0.78 mm x 0.78 mm x 4-4.5 mm resolution, TR = 170 msec, TE = 4.9 msec and FA = 50°. The subject responses were monitored and coded with *Cool Edit*TM software into two categories, “correct” and “other” responses. The data analysis was performed with *AFNI*TM (85) and *Matlab*TM software.

The image acquisition parameters were the same for the normal subjects, the only change being that the functional runs were each 111 images long. Also, the categorization of the subject overt responses into “correct” or “other” was moot since the patients were able to answer all the semantic queries correctly.

Data Analysis

The five functional runs were registered to a common base-image (the last image of the last run), detrended of linear trends and concatenated to give a 805-image time-series (555-image time-series for controls). To estimate the TCM-related signal changes, all the subject responses (both “correct” and “other”) were pooled together and an overt-response locked stimulus vector was constructed. This vector had 805 (555 for controls) data-points, all zero except the ones corresponding to images in which there was an overt response.

Deconvolution and Regression

For each voxel, the signal was considered to be the result of a convolution of the overt-response locked stimulus vector with the voxel impulse response (IRF) plus a constant baseline and a white-noise term. Fifteen lag impulse responses were deconvolved for each voxel from the knowledge of the observed voxel fMRI time-series and the stimulus vector. The deconvolution analysis was performed as described in Chapter 2. The significance of activation at each voxel was assessed through the use of a General Linear Model (GLM). The details of the GLM are as follows:

$$\begin{aligned} H_0 : Z_n &= \gamma_0 + \varepsilon_n \\ H_a : Z_n &= \beta_0 + \sum_{m=0}^p h_m f_{n-m} + \varepsilon_n \end{aligned} \quad [4.1]$$

where Z_n is the voxel time-series, γ_0 is the constant baseline parameter under the baseline model, β_0 is the constant baseline parameter under the full model, and the summation denotes the discrete-time finite-lag convolution of the $f(t)$, the stimulus vector and $h(t)$, the IRF over $p = 15$ lags ($p = 12$ lags for controls), ε_n is the white noise component and N is the number of time-points in the time-series. The significance of activation (i.e. rejection of the null hypothesis) was assessed through the calculation of the F -statistic for regression. The coefficient of determination R^2 was also calculated. R^2 expresses the goodness of fit and can be thought of as the ratio of the variance in the time-series that can be ascribed to the full model to the total variance of the time-series.

Estimation of the TCM Signal Changes

Speech-related false positive activation due to TCM occurs at/near high contrast boundaries on or outside the brain (124, 125). They are also more pronounced in the inferior and frontal regions of the brain (124) and have some distinct characteristics in

that most of the noise due to TCM occurs in the first few images during and after speech (123-125). The fluctuations are generally a sharp increase/decrease in signal during and just after speech. Thus, examining voxel IRFs on or near high contrast boundaries on or outside the brain, for sudden signal changes, above the threshold selected for inferring brain activation will lead to characterizations of different forms the TCM-related signal changes take. Since signal changes due to TCM have a common origin, it is reasonable to expect that a handful of selected TCM voxels can form an adequate representation of TCM-related signal changes in the brain.

Ten to fifteen (depending on the situation) distinct voxel impulse responses at/near high contrast boundaries, on/outside the brain, showing signal changes above the threshold selected for inferring brain activation, were selected to adequately characterize TCM IRFs in the FMRI dataset. Figure 4.1 illustrates this procedure for the case of a few TCM IRFs. The chosen TCM IRFs were convolved with the overt response-locked event vector to form the corresponding 805-image (555-image for controls) TCM time-series.

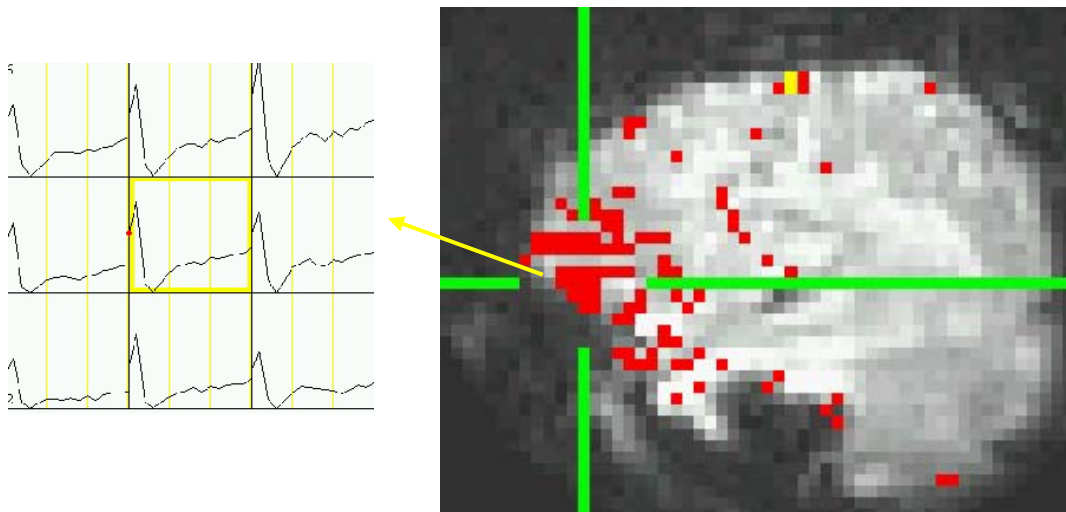


Figure 4.1: Activation map overlaid on a low-resolution spiral FMR image. The red voxels correspond to $R^2 > 0.2$ and the yellow voxels denote $R^2 > 0.3$. The yellow arrow points to the voxel IRFs. The central voxel in the grid shows a selected TCM IRF.

Choosing Representative BOLD HRFs

In order to optimize the ‘retention of true-positives’ capability of the selective detrending method, a few (3 or 4) representative estimated BOLD hemodynamic responses were selected from the FMRI dataset. The chosen BOLD HRFs activated above the threshold selected for inferring brain activation and spanned the possible delays (phase of onset of hemodynamic responses) in the dataset. The criterion used in selecting the voxels for detrending involved computation of cross-correlation coefficients of the voxel IRFs with the selected representative BOLD HRFs. The computed cross-correlation coefficients acted as a test of whether BOLD MR signal was being reduced (as is explained in the next section). Hence 3-4 representative BOLD HRFs were sufficient to characterize true positive BOLD voxels.

Selective Detrending Algorithm

For each 16-image voxel IRF (13-image IRF for controls) in the FMRI dataset, the cross-correlation coefficient CC_{TCM} of the voxel IRF with each of the representative TCM IRFs was calculated. Also the representative TCM IRF for which the absolute value of the CC_{TCM} was a maximum was found. This value was employed as an indicator of false-positive TCM corruption in the voxel time-series. For each 16-image voxel IRF (13-image IRF for controls) in the FMRI dataset, the cross-correlation coefficient CC_{BOLD} of the voxel IRF with each of the representative BOLD HRFs was also calculated. Also the representative BOLD HRF for which the value of the CC_{BOLD} was a maximum was found. This value was employed as an indicator of true positive BOLD MR signal in the voxel time-series. The selective detrending algorithm endeavored to maximize the reduction of false positive TCM signal as well as the retention of true positive BOLD MR signal. To achieve this, each voxel time-series was detrended of components

proportional to the maximally correlated representative TCM time-series in one of three different ways depending on the voxel IRF's correlation with the representative TCM time-series and the selected BOLD time-series:

Case 1: if $\max(\text{abs}(CC_{TCM})) > 0.5$ and $\max(\text{abs}(CC_{TCM})) > CC_{BOLD} + 0.2$

then the voxel time-series was detrended of components proportional to the corresponding representative TCM time-series using linear least-squares fit (100). The implicit assumption is that if the voxel time-series satisfies these criteria most of the task-correlated signal changes in it are TCM-related.

Case 2: if $\max(\text{abs}(CC_{TCM})) > 0.5$ and $CC_{BOLD} + 0.2 > \max(\text{abs}(CC_{TCM})) > CC_{BOLD}$

then the voxel time-series was detrended of components proportional to a corresponding more temporally localized representative TCM time-series formed by considering only the first three images in the representative TCM IRF during construction. The detrending was performed only if the norm of the residuals of the fit of the first three images of the voxel IRF with those of the representative TCM IRF was less than a set value $resnorm_{TCM}$. The implicit assumption here is that if the voxel time-series satisfies these criteria, there is enough likelihood of presence of both BOLD MR signal and TCM signal in it to merit a more localized examination of its epochal signal changes. Since the TCM signal changes occur mostly in the first three images after speech, detrending components proportional to the more localized TCM time-series (given there exists the requisite fit between the voxel IRF and the TCM IRF) is anticipated to reduce the motion corrupted parts of the BOLD MR signal changes in case of presence of both BOLD and TCM signal changes or decrease the major fluctuations in signal due to TCM in case the voxel time-series mainly consist of TCM signal changes. For the datasets studied $resnorm_{TCM} =$

0.15, corresponding to a p-value for the fit more than 0.95 between the voxel IRF and TCM IRF, was adequate in achieving the mentioned goals.

Case 3: if $\max(\text{abs}(CC_{TCM})) > 0.5$ and $\max(\text{abs}(CC_{TCM})) < CC_{BOLD}$

then the voxel time-series was detrended of components proportional to a corresponding more localized representative TCM time-series formed by considering only the first three images in the representative TCM IRF during construction. The detrending was performed only if the norm of the residuals of the fit of the first three images of the voxel IRF with those of the representative TCM IRF was less than a set value $resnorm_{BOLD}$. The assumption here is that if the voxel time-series satisfies these criteria it mainly consists of BOLD signal changes, the retention of which outweighs the need for reduction of TCM signal changes (if they exist). Hence, the criterion for the fit is more stringent. For the datasets studied $resnorm_{BOLD} = 0.003$, corresponding to a p-value of more than 0.999 (133) was adequate to achieve the set goals.

The above criteria were chosen to maximize the elimination of TCM-related signal as well as the retention of BOLD MR signal. They rely on prior empirical observations on BOLD MR signal and TCM-related signal (30,123-125). The first part of the algorithm seeks voxels which are presumably affected by TCM alone. These voxel time-series are detrended of components proportional to the maximally correlated representative TCM time-series. The selection criteria used to detect these voxels require a minimum threshold of 0.5 (corresponding to a p-value of 0.05) for $\max(\text{abs}(CC_{TCM}))$ as well as a degree of separability between $\max(\text{abs}(CC_{TCM}))$ and $\max(CC_{BOLD})$. The choice of 0.5 for the minimum threshold for cross-correlation is conservative. From the datasets studied voxels exhibiting significant TCM corruption generally possess much

higher values for CC_{TCM} . Figure 4.2 shows the activation map formed by $\max(CC_{TCM})$ overlaid on the IRF dataset. It is apparent that voxels exhibiting significant TCM possess high values of $\max(CC_{TCM})$. Most of the activated voxels seem to have a $\max(CC_{TCM}) > 0.7$.

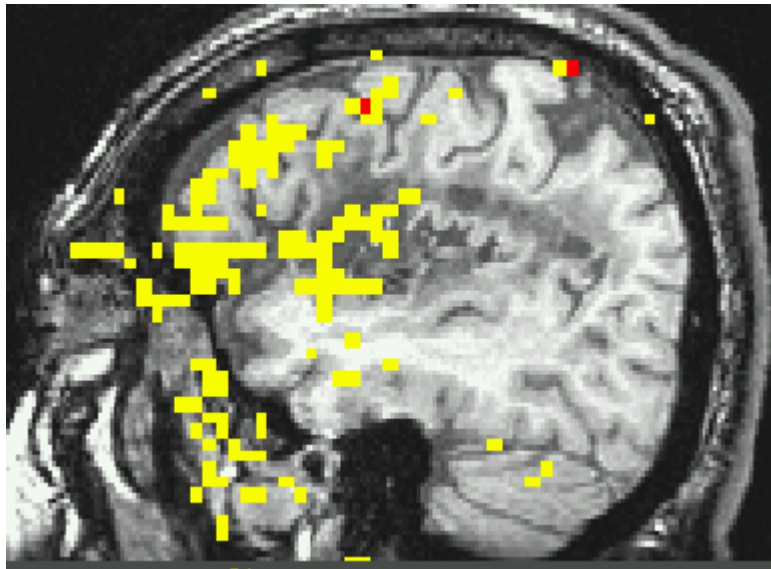


Figure 4.2: Activation map of the maximal absolute cross-correlation coefficient with TCM CC_{TCM} , thresholded by $R^2 > 0.1$. The yellow voxels correspond to $\max(CC_{TCM}) > 0.7$ and the red denotes $\max(CC_{TCM}) > 0.5$.

Case 1 also mentions the requirement of the presence of more correlation between the voxel IRF with the TCM IRF than that with the BOLD HRF. This requirement was introduced to ensure that voxels selected by this criteria possess mainly TCM signal changes even if the $\max(\text{abs}(CC_{TCM}))$ and $\max(CC_{BOLD})$ are both more than 0.5. The choice of 0.2 for separability between CC_{TCM} and CC_{BOLD} was conservative. Figure 4.3 (a) shows the distribution of the ratio of number of voxels undergoing non-selective detrending for a given $\max(CC_{BOLD})$ threshold to the total number of voxels in the dataset activated above the same threshold, for 3 different levels of separability between $\max(\text{abs}(CC_{TCM}))$ and $\max(CC_{BOLD})$; 0.0, 0.1 and 0.2, on top of the criteria that the voxel

be more correlated with the TCM responses than the BOLD responses. Figure 4.3 (b) shows the ratio of number of voxels undergoing non-selective detrending for a given $\max(\text{abs}(CC_{TCM}))$ threshold to the total number of voxels in the dataset activated above the same threshold, for the same levels of separability as Fig 4.3 (a). Examining Figure 4.3 (a), the curve for $\text{separability} = 0.2$ seems to indicate that roughly 10% of the voxels with $\max(CC_{BOLD}) \approx 0.7$ will undergo global detrending, where the voxels will be detrended of components proportional to the maximally correlated TCM time-series. But this corresponds to $\max(\text{abs}(CC_{TCM})) > 0.9$, at which level the voxel has a strong probability to be a TCM false-positive. At this level of separability, the Fig 4.3 (b) shows that around 10% of voxels with $\max(\text{abs}(CC_{TCM})) \approx 1$ are detrended of components to the TCM time-series formed by considering only the first three images of the TCM IRFs. The local detrending is by nature of its conception, less successful in reducing TCM signal changes than the global detrending. Thus, examining the curves, it is apparent that $\text{separability} = 0.2$ condition, if anything enhances the probability of retaining true-positive BOLD signal at the expense of diminished capacity to reduce false-positives. The second criteria regarding temporally localized detrending is expected to compensate for any attenuation in the false-positive reduction capacity. The results in the next chapter support this assertion.

The second part of the algorithm examines voxels that show sufficient correlation between both TCM and BOLD responses. These voxels are detrended only if the fit between the first 3 images of their impulse response and the selected TCM IRFs is lower than a set limit. The set limit is more stringent for those voxels which are sufficiently correlated to both TCM and BOLD responses and in addition show more correlation with

the chosen BOLD HRFs. From the description, it is apparent that the proper characterization of the BOLD and TCM responses is critical to the success of the method.

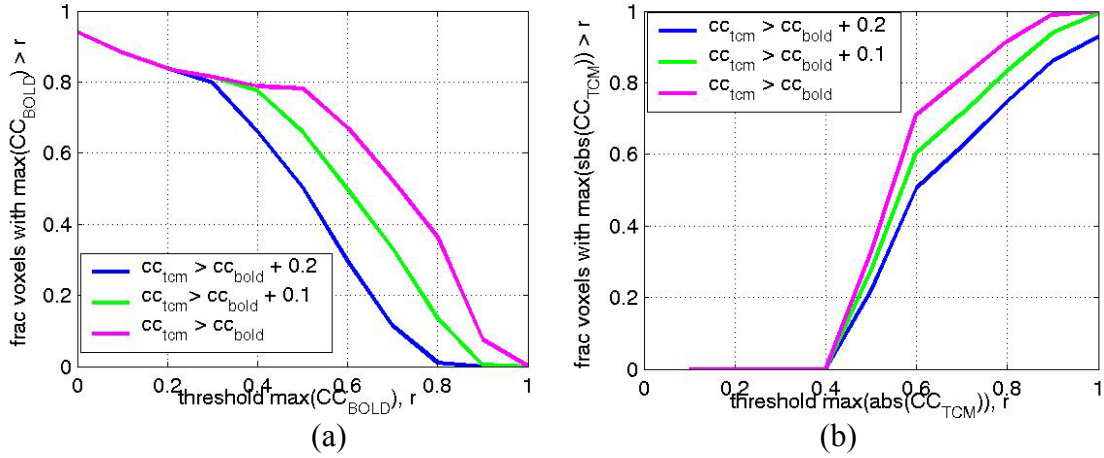


Figure 4.3: Distribution of number of voxels undergoing non-selective detrending for a given $\max(CC_{BOLD})$ as a fraction of the number of voxels at that $\max(CC_{BOLD})$ for three different levels of separability, 0.2 (blue), 0.1 (green) and 0.0 (magenta) (a). Similar distributions for $\max(\text{abs}(CC_{TCM}))$ (b).

Analysis of Detrended Time-Series

The analysis of the detrended time-series proceeded in the same way as the undetrended time-series analysis. For each voxel the signal was considered to be the result of sum of convolutions of the “correct” response-locked stimulus vector and “other” response-locked stimulus vector and their corresponding impulse responses, plus a constant baseline and a white noise component. Fifteen lag impulse responses (12 for normal control subjects) for each of the conditions were estimated from the knowledge of the observed voxel fMRI time-series and the stimulus vectors.

For the GLM, the baseline model was considered to include a constant baseline and the fitted signal due to “other” responses plus white noise, whereas the full model was considered to include a constant baseline, the fitted signal due to “other” responses and

the fitted signal due to the “correct” responses plus white noise. In this way, the test-statistics F and R^2 quantified significance of “correct” response related signal alone.

Implementation of Motion Parameter Regression

Motion parameter regression (MPR) has been introduced in Chapter 3. Here the methods to implement MPR in a GLM based deconvolution analysis framework are described. The motion parameters for each image in the 805-image (555-image for controls) time-series were obtained from the image-registration program. For each voxel, the rigid-motion related signal at each scan was modeled as a quadratic function of the motion parameters in that scan and the preceding scan (117, 118). The motion-related signal was modeled as part of the baseline, along with the “other” response related signal changes, so that the regression statistic reflected the activation due to “correct” responses alone. The regression model (for patients) used is as follows:

$$\begin{aligned}
 H_a : Z_n = & b_0 + \sum_{r=0}^6 M_{r,n} \alpha_r + M_{r,n-1} \beta_r + \sum_{r=0}^6 M_{r,n}^2 \alpha'_r + M_{r,n-1}^2 \beta'_r \\
 & + \sum_{p=0}^{15} s_{n-p}^c h_p^c + \sum_{p=0}^{15} s_{n-p}^o h_p^o + \varepsilon_n \quad [4.2] \\
 H_0 : Z_n = & b_0 + \sum_{r=0}^6 M_{r,n} \alpha_r + M_{r,n-1} \beta_r + \sum_{r=0}^6 M_{r,n}^2 \alpha'_r + M_{r,n-1}^2 \beta'_r \\
 & + \sum_{p=0}^{15} s_{n-p}^o h_p^o + \varepsilon_n
 \end{aligned}$$

where $M_{r,n}$ is the motion parameter for the r^{th} degree of freedom at the n^{th} image, α , β , α' and β' are fitted constants, s^c and s^o are the “correct” and “other” response-locked stimulus vectors and h^c and h^o are the corresponding estimated impulse response functions. The impulse responses are estimated to 12 lags for the normal controls. The regression F and R^2 statistics were calculated for each voxel to quantify the significance of activation related to the “correct” response stimulus.

Implementation of the Screening Images Method

The method of screening images during speech (127) uses the observation (123-125) that most of the signal fluctuations due to speech occur in the first few images during and after speech. This method was implemented in the context of a GLM based deconvolution analysis by ignoring the zeroth and first lags while estimating the voxel IRF. The regression model (for patients) used was as follows:

$$\begin{aligned}
 H_a : Z_n &= b_0 + \sum_{p=2}^{15} s_{n-p}^c h_p^c + \sum_{p=0}^{15} s_{n-p}^o h_p^o + \varepsilon_n \\
 H_0 : Z_n &= b_0 + \sum_{p=0}^{15} s_{n-p}^o h_p^o + \varepsilon_n
 \end{aligned}
 \tag{4.3}$$

The “other” response related signal was modeled as part of the baseline. For the case of normal controls the IRFs were estimated up to 12 lags. The activation statistics R^2 and F , quantify the significance of activation due to “correct” responses. It should be noted that the signal changes occurring during the first two images after overt production do not contribute to the activation statistic in this method, whether it is TCM-related or BOLD-related.

Implementation of Non-Selective Detrending

The non-selective detrending method proposed by Birn et al. (125) also assumes that the TCM-related signal changes are temporally resolved from BOLD MR signal changes. This method has been described in Chapter 3.

In the present context, the implementation of the non-selective detrending method followed that of the selective detrending method up to the part regarding estimation of TCM IRFs. The difference is in the detrending procedure. In the non-selective detrending all the voxels in the fMRI dataset are detrended of components proportional to all the representative TCM time series using a linear least-squares method (100). Since this is

equivalent to detrending all the voxels in the FMRI dataset of components proportional to sum of all the chosen TCM time-series only a few (5-6 as opposed to 10-15) representative TCM time-series suffice. The detrended FMRI datasets were analyzed in exactly the same manner as described in the selective detrending method.

Receiver Operating Characteristics

The difficulties in conducting conventional ROC analysis have been mentioned in Chapter 2. Here the performance of the selective detrending method and its comparison with the other three methods as well as the case of no noise reduction is conducted through a modified ROC analysis procedure. The ROC procedure was used to measure two complementary indications of efficacy 1) the reduction of the false positive voxels outside the brain in the real FMRI datasets and 2) the retention of the true-positive voxels inside the brain, with IRFs satisfying strict criteria for BOLD hemodynamic responses.

Reduction of False Positives

The voxels outside the brain that possess R^2 or F values above the threshold selected to infer brain activation can be trivially considered to be false-positive voxels at that threshold. This is reinforced by considering voxels a sufficient distance outside the brain such that there are no effects due to large veins at the boundaries of the brain. The signal intensities in a low-resolution spiral MR image decrease rapidly away from the brain edge. By constructing signal-intensity histograms, the high intensity intra-cerebral voxels can be separated from the extra-cerebral voxels. Since TCM-related signal changes are accentuated at high contrast boundaries outside the brain created by CSF, cranium, air cavities, and scalp (134), the chosen test-bed can be considered to contain a fair population of TCM voxels. A further reduction of the test-bed, using the knowledge that TCM-corrupted voxels show more fluctuation in the early part of the IRF, can

increase the proportion of TCM-corrupted voxels in the test-bed. Thus, the distribution of number of detected voxels as a function of threshold R^2 or F -statistic can be used to compare the efficacy of motion correction of all the four methods.

For each fMRI dataset, an intensity-based brain mask was created using an iterative outlier-reduction method. This is implemented as a program in the *AFNI*TM software. This program also allows for dilating the brain mask by the requisite number of voxels to include regions just outside the brain which are low-intensity but exhibit venous activation arising from large peripheral veins. Voxel IRFs (a sufficient distance outside the brain to preclude venous effects) exhibiting larger fluctuation in the first 5 images relative to the last 11 (7 for controls) images were chosen to form the test-bed of false-positive activation. The distribution of the number of voxels in the test-bed detected as a function of threshold R^2 was constructed for all the four methods as well as for the case of no motion correction.

An important property of the test-bed of false positives is that the method of obtaining the test-bed is independent of the algorithm to estimate false positive TCM signal changes. An assumption implicit in construction of the test-bed is that TCM signal changes in false-positive voxels outside the brain are representative of the TCM signal changes at high contrast boundaries on the brain. This assumption is valid when the TCM signal changes of voxels in the brain are not corrupted by BOLD signal changes.

Retention of True Positives

The intra-cerebral voxel IRFs, specified by the brain masking method, were fitted to a generic hemodynamic response curve. This curve, which is included as part of the *AFNI*TM software, is parameterized in terms of amplitude, delay-time, rise-time and fall-time. The functional form of the curve is given by

$$\begin{aligned}
h(t) &= \frac{A}{2} \left[\tanh \left[\tan \left(\frac{\pi}{2} \left(\frac{1.6(t-t_D)}{t_R} - 0.8 \right) \right) \right] + 1 \right] & t_D < t \leq t_D + t_R \\
h(t) &= \frac{A}{2} \left[\tanh \left[\tan \left(\frac{\pi}{2} \left(\frac{1.6(t_F + t_R + t_D - t)}{t_F} - 0.8 \right) \right) \right] + 1 \right] & t_D + t_R < t \leq t_D + t_R + t_F \\
h(t) &= 0 & \text{otherwise}
\end{aligned} \quad [4.4]$$

where A is the amplitude, t_D , t_R and t_F are delay-time, rise-time and fall-time of the hemodynamic response respectively. This function is more malleable to be fitted to estimated IRFs than gamma-variate functions (especially at low temporal resolutions). It also has the advantage of being parameterized in terms of temporal aspects of the HRF, a useful feature that comes of use while screening IRFs. The IRF of each voxel was fit to the generic hemodynamic response function (HRF) by means of a nonlinear optimization method using *Matlab*TM.

$$\chi^2 = \|h(t, \mathbf{a}) - I(t)\|^2 = \sum_i (h(t_i, \mathbf{a}) - I(t_i))^2 \quad [4.5]$$

where χ^2 is the cost function that was minimized by varying the parameter set \mathbf{a} which consists of the parameters amplitude, t_D , t_R and t_F , t is time discretized by the index i , h is the generic HDR described in Equation 4.4 and I is the voxel IRF. The parameters were varied iteratively till the cost function was minimized using a large-scale algorithm. This fitting was carried out with the *lsqcurvefit* function of *Matlab*TM. Figure 4.4 shows the estimated hemodynamic response of a true-positive BOLD voxel in the right medial frontal region of patient 1 (pre-therapy) dataset (blue) and the corresponding fit (green) from employing the non-linear optimization method. The graph shows the evolution of

the curves over the first 20 seconds (which is the part of the IRFs relevant to the selection criteria).

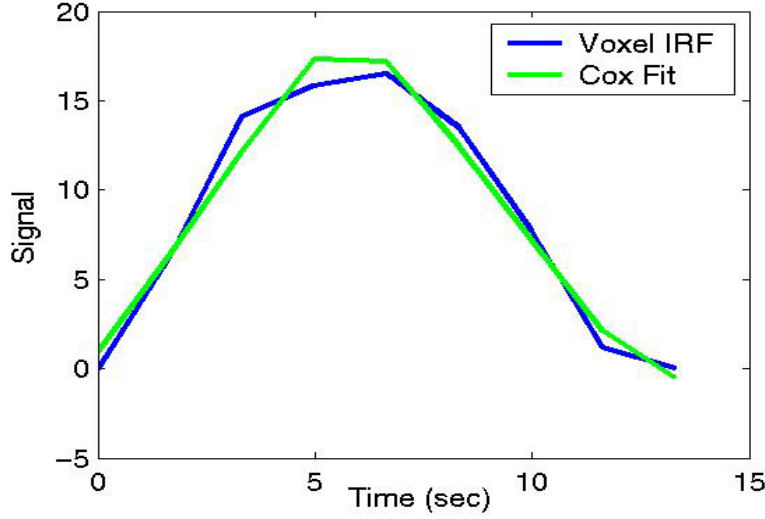


Figure 4.4: Estimated hemodynamic response of a true positive right medial frontal voxel of patient 1 (pre-therapy) dataset (blue) and the corresponding fit to a generic hemodynamic response (green).

The maxima of the first 4 images of each voxel IRF, $\max(IRF_{1-4})$ and the corresponding minima, $\min(IRF_{1-4})$ were also calculated. Intra-cerebral voxel IRFs satisfying the following criteria formed the test-bed for hemodynamic-like voxels.

$$\begin{aligned}
 & A > 0 \\
 & t_D + t_R + t_F > 6 \\
 & t_D + t_R < 11 \\
 & t_R + t_F > 4 \\
 & t_F, t_R > 1 \\
 & t_D < 4 \\
 & \max(IRF_{1-4}) > 1.2 \min(IRF_{1-4})
 \end{aligned} \tag{4.6}$$

where the terms are as defined above. Time is expressed in units of image TR (i.e. $1 \approx 1.66$ sec). The set of criteria relating to amplitude and time were chosen so as to eliminate TCM-related IRFs. The penalty paid in terms of screening some BOLD HRFs was compensated by the fact that the chosen test-bed was devoid of TCM voxels. The

distribution of the number of voxels in the selected test-bed detected as a function of threshold R^2 was constructed for all the four methods as well as for the case of no motion correction. The distributions were constructed to provide a means of comparing the true-positives retention capabilities of the four methods to retain true positive voxels.

CHAPTER 5 RESULTS AND DISCUSSION

In this chapter the results of the application of the selective detrending method as well as the other methods of reducing noise arising from task-correlated motion are presented and compared. The implications of the results on data analysis of event-related overt word-generation FMRI paradigms are discussed.

Results

In the following pages the omnibus results from the application of the four methods of TCM noise reduction reviewed, on FMRI datasets involving event-related overt generation paradigms in four patient datasets (two patients scanned twice, pre and post treatment) and four control subject datasets, are presented in the form of statistical activation maps parameterized by the coefficient of determination, R^2 . The case of no noise correction is also provided for reference. In addition the results from the modified ROC analysis, i.e., the false-positives reduction capacity as well as true-positives retention capacity, examined based on separate voxel test-beds, are also provided for all the four patient datasets and the four control subject datasets. In the figures of the R^2 -activation maps green arrows point to selected BOLD HRF AFNI-grabs and blue arrows point to selected TCM IRF AFNI-grabs. In the graphs for the modified ROC analysis, the symbols ‘ML0’ and ‘ML2’ stand for min-lag (the lowest ‘lag’ to which the impulse response is estimated) set to 0 and 2 respectively. Also all the activated voxels (in red) in the selective detrending activation maps possess BOLD hemodynamic-like responses.

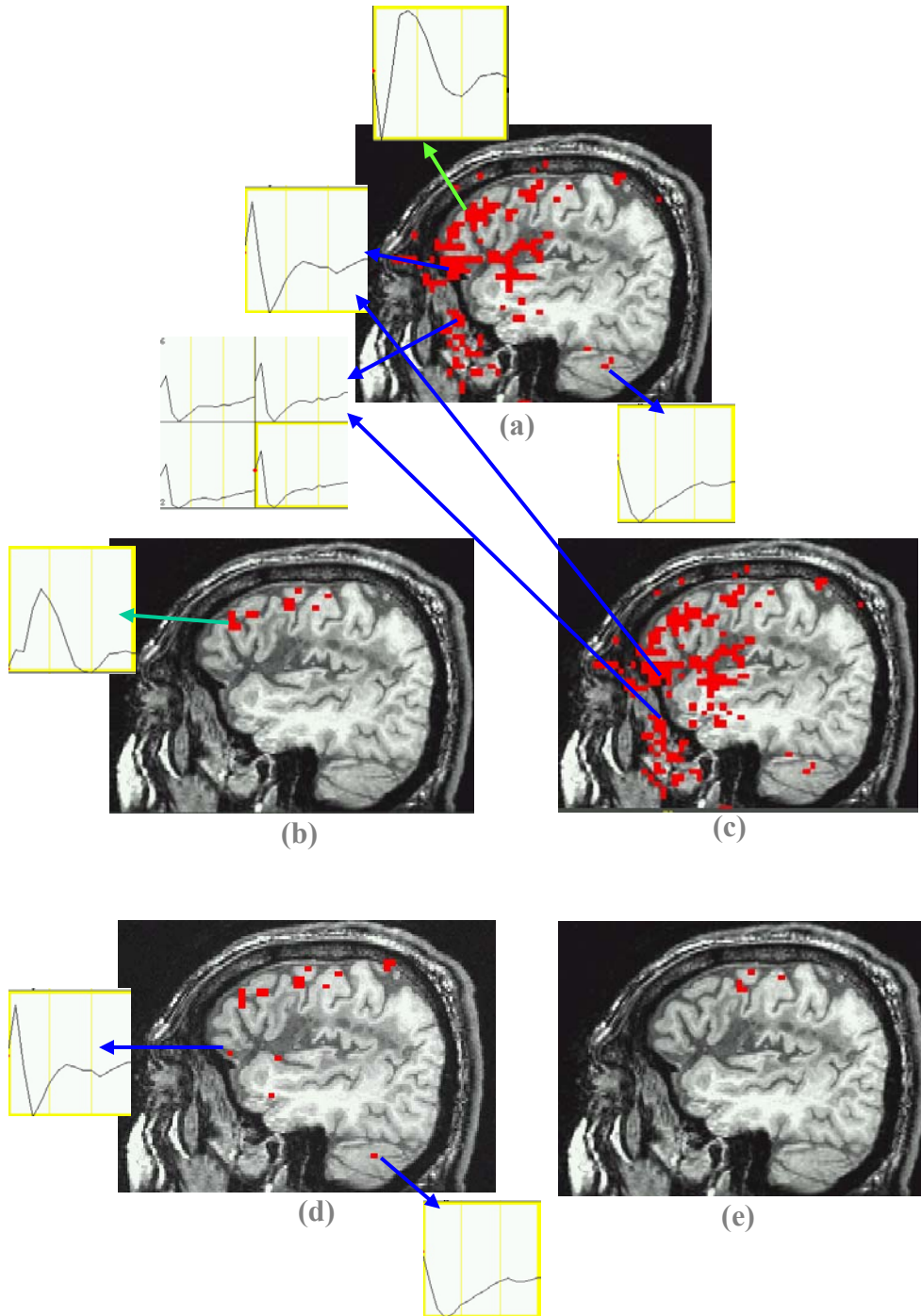


Figure 5.1 Activation maps thresholded at $R^2 > 0.2$ for patient-1 (pre-scan) with no TCM noise-reduction (a), with selective detrending (b), with motion parameter regression (c), with ignoring 2 images after speech (d) and with non-selective detrending (e). The blue arrows indicate TCM voxel IRFs and the green arrows BOLD voxel IRFs.

Patient 1 (Pre-Treatment)

The Figure 5.1(a) shows a lateral sagittal slice of a high-resolution T1-weighted anatomic image with the R^2 -activation map overlay for the aphasia-patient-I (under pre-treatment condition), without TCM noise reduction. Some of the estimated TCM IRFs and BOLD HRF for selected voxels are also shown. Figure 5.1(b) shows the map with selective detrending. All the voxels shown activated in the selective detrending map exhibited BOLD HRF responses. The green arrow in the figure points away from activation at the inferior frontal sulcus (IFS), which is implicated in word-generation. The selective detrending method is able to attenuate the motion-corrupted portion of the IFS hemodynamic response. Figures 5.1 (c-e) show the R^2 -activation map for the same patient under the same scan after motion parameter regression, ignoring two images after speech and non-selective detrending. All the voxels activated above a threshold $R^2 > 0.20$ (corresponding to p-value $< 10^{-20}$) shown in red. All the activated voxels in the selective detrending map (Figure 5.1 (b)) exhibited BOLD HRF similar to the one shown by the green arrow in Figure 5.1 (b). Figure 5.1 (a) shows a lot of TCM corrupted false-positive voxels, particularly in the inferior and frontal regions. A few representative TCM impulse responses are shown by the blue arrows. From the figures (5.1 (a-e)) for the 5 cases it can be noted that for this subject the motion-parameter regression (MPR) method performs poorly with regard to TCM noise reduction.

The method of ignoring the first two images during speech (Figure 5.1 (d)) performs better than the MPR method. However it still exhibits some false-positive TCM voxels as marked by the blue arrows. The non-selective detrending method (Figure 5.1 (e)) is sub-optimal in this case. This method seems to reduce the true-positive BOLD hemodynamic signals in the inferior frontal sulcus.

The selective detrending method performs better than all other techniques. Not only is it able to reduce TCM-related false positive activation, but also it is also able to retain the brain activation voxels corrupted by motion artifacts, and to remove parts of the signal time course originating from motion. Figure 5.1 (b) shows one such example for the case of an inferior frontal sulcus voxel (which is implicated in semantic word generation). The sudden large fluctuation in the signal at the onset of the response caused by task-correlated motion is attenuated to give a more regularized hemodynamic response as shown by the green arrow.

The above statement is quantified in the modified ROC analyses illustrated in Figures 5.2 (a-b). The efficiency of TCM noise reduction of all the four methods as well as for the case of no motion correction is shown in Figure 5.2 (a) for aphasia patient-1 (pre-scan). Ideally, all the voxels in the ‘false-positives’ test-bed should go to zero (or more accurately go towards the null distribution values). The selective detrending method (denoted ‘dtsel’ and represented by the magenta curve) performs almost as well as the non-selective detrending method (denoted ‘dt’ and represented by the red curve) in terms of reducing TCM false-positives. The method of ignoring images (ML2; black) is less optimal whereas the motion-parameter regression method (MPR; green) seems to have very little effect on TCM voxels. The case with no motion correction (ML0; blue) is also shown for reference.

Figure 5.2 (b) shows the effect of each of the TCM noise reduction treatments on the test-bed of the true-positive BOLD HRF-like voxels. Since the criteria for inclusion into the test-bed precludes the occurrence of speech-related TCM voxels, ideally a given treatment should have the same distribution as for the case of no noise correction. There

does not seem to be much difference in the true-positives retention capacity between the MPR, ML2 and selective detrending methods. The non-selective detrending method seems to suffer from a loss of sensitivity to BOLD MR signal. By considering this graph along with the TCM noise reduction graph of Figure 5.2 (a) one can state that the selective detrending method performs the best in terms of TCM noise reduction and true positive BOLD HRF retention.

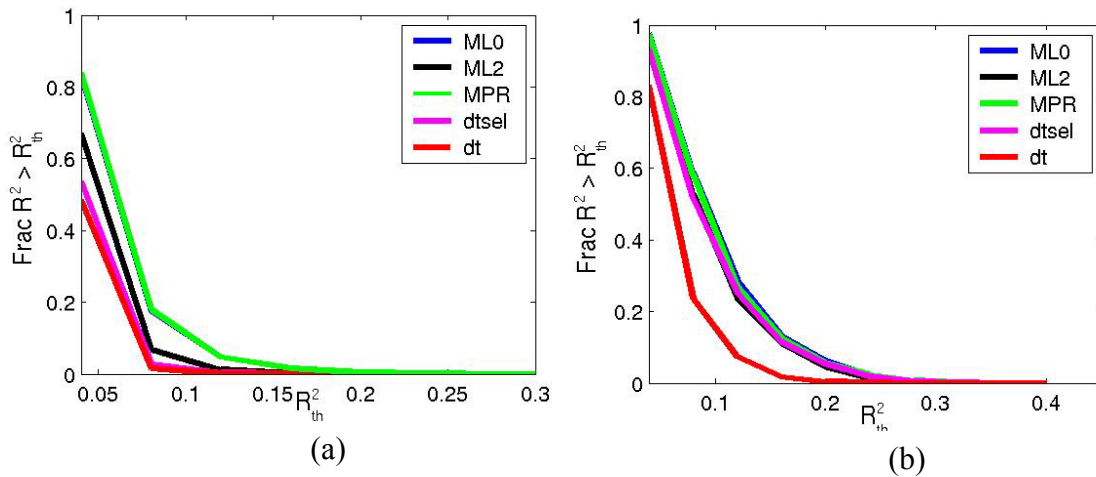


Figure 5.2: Fraction of voxels detected as a function threshold R^2 for (a) the false-positives test-bed and (b) the true-positives test-bed for aphasia patient 1 (pre-therapy scan). The blue curve (ML0) represents the case of no motion correction, the black curve (ML2) represents the method of ignoring the first 2 images after speech, the green curve (MPR) represents the motion-parameter regression method, the magenta curve (dtsel) represents the selective detrending method and the red curve (dt) represents the non-selective detrending method.

The superior performance of the selective detrending method when compared to the method of ignoring images and the non-selective detrending method can be comprehended by examining Figure 5.3. The figure on the left, 5.3 (a), shows some representative TCM corrupted impulse responses chosen from voxels outside the brain for aphasia patient 1 (pre-therapy scan).

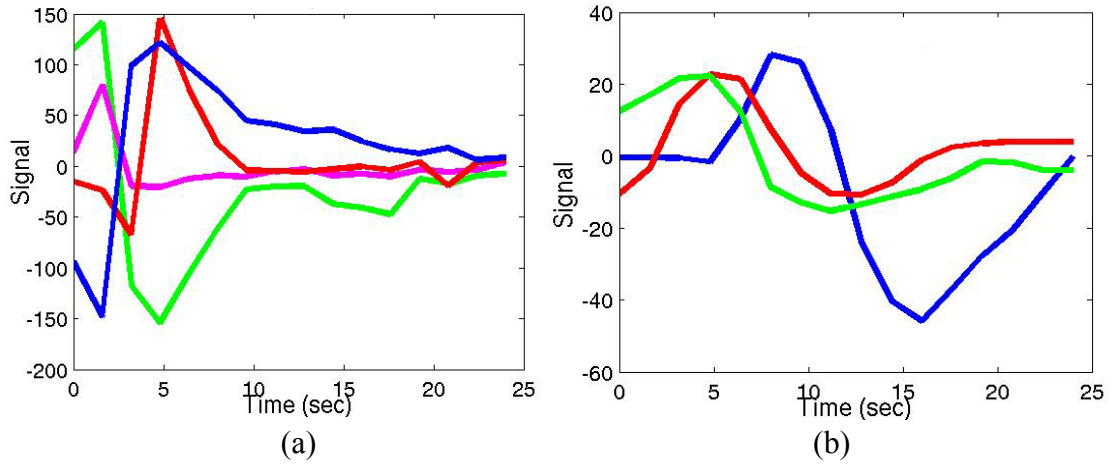


Figure 5.3: Some representative TCM-related voxel IRFs (a); Some representative BOLD HRFs (b) from aphasia patient 1 (pre-therapy scan) data.

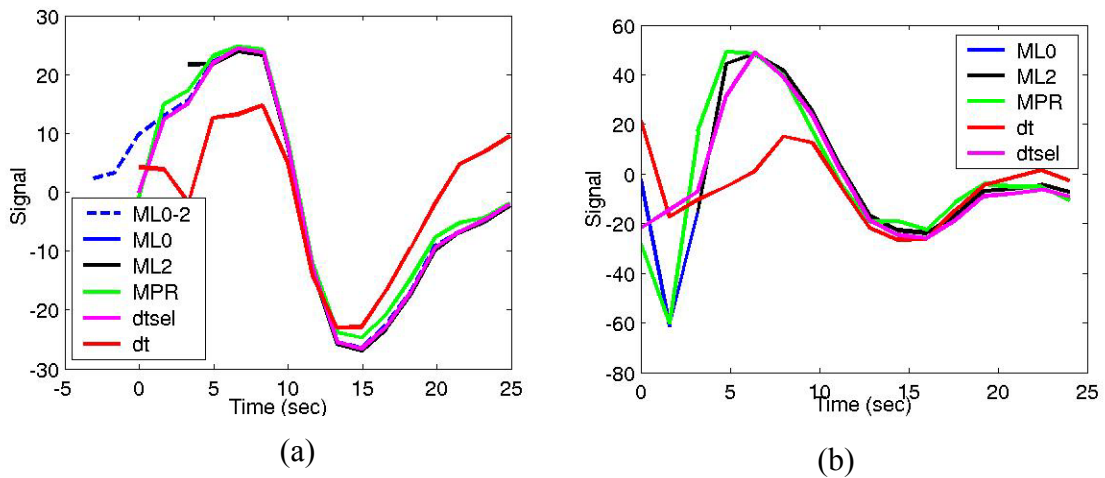


Figure 5.4: The effect of the methods of noise correction on a right medial-frontal voxel BOLD HRF exhibiting an 'early' response for patient 1 pre-therapy scan (a). The effect of the methods of noise correction on a right inferior sulcus voxel, exhibiting both BOLD and TCM signal changes (b) for the same scan. The no-correction curve is hidden by the selective detrending curve in both figures.

Some of the TCM IRFs (e.g. the red curve) are shifted relative to the time of onset. Some of responses (blue) have significant longer lasting effects. Thus the method of ignoring two images after speech may not adequately attenuate the effects of TCM in these voxels and false-positive activation may remain even after the correction algorithm is executed. Increasing the number of ignored images is not an attractive option, in that this may lead to loss of sensitivity to true-positive BOLD responses (as can be inferred from Figure 5.3). In fact one perceives a potential loss of sensitivity to some true-positive BOLD HRFs (especially the green and red curves in Figure 5.3 (b)) even for the ML2 method.

An analogous analysis can be made for the case of the non-selective detrending method. Attenuating the effects of TCM in the voxel IRFs shown in Figure 5.3 (a) may lead to attenuation in true-positive BOLD signal in some voxels as represented by the curves in Figure 5.3 (b). This is the source of the sub-optimal true-positives retention capacity of the non-selective detrending method.

Figure 5.4 (a) shows the effect of applying the reviewed methods of TCM noise reduction on a BOLD activation voxel in the right medial-frontal region of aphasia patient 1 (pre-therapy scan). This voxels hemodynamic response has an ‘early’ onset. This could be due to the overt response-locked stimulus vector used in the analysis. Presumably this voxel covers neuronal sources that activate prior to the overt-response, or the voxel HRF has zero delay to onset and the resolution of the stimulus vector and image acquisition is not sufficient to extract the early response. The blue dashed curve (ML0-2) in Figure 5.4 (a) (which has been generated by shifting the response-locked stimulus vector back by two images) suggests that the HRF has started prior to word-enunciation. It is obvious from the Figure 5.4 (a) that the method of ignoring two images

during speech (ML2, black) suffers from a lack of sensitivity to the early portion of the hemodynamic response, since the method ignores the first two images. The non-selective detrending method (dt, red) removes BOLD MR signal in this voxel and hence is sub-optimal. The selective detrending method (dtsel, magenta) does not perform any detrending on this voxel and leaves the putative “early-onset” BOLD signal intact. The motion parameter regression method (MPR, green) also does not suffer from loss of sensitivity to BOLD MR signal in this case.

An added advantage of the selective detrending method is that it has the capacity to at least partially tease apart TCM and BOLD signal changes in a brain activation voxel that has been affected by both. Figure 5.4 (b) shows the voxel HRFs of an inferior frontal sulcus voxel of patient 1 (pre-therapy scan). (This voxel has been marked by the green arrow in the Figure 5.1 (b)). From the graph, in the curve representing no noise correction (ML0, blue), one perceives a large initial fluctuation in signal (caused by TCM) and a subsequent smooth hemodynamic response (caused by brain activation) The selective detrending method (dtsel, magenta) is able to attenuate the TCM-related signal changes resulting in a more regularized hemodynamic response. The motion parameter regression method (MPR, green) does not have much affect on the voxel IRF. The non-selective detrending method (dt, red) removes a lot of BOLD signal along with the TCM signal. The method of ignoring two images during speech (ML2, black) performs almost as well as the selective detrending method in this case.

Patient 1 (Post-Treatment)

The Figure 5.5 (a) shows a lateral sagittal slice of a high-resolution T1-weighted anatomic image with the R^2 -activation map overlay for the aphasia-patient-I (under post-treatment condition), without TCM noise reduction.

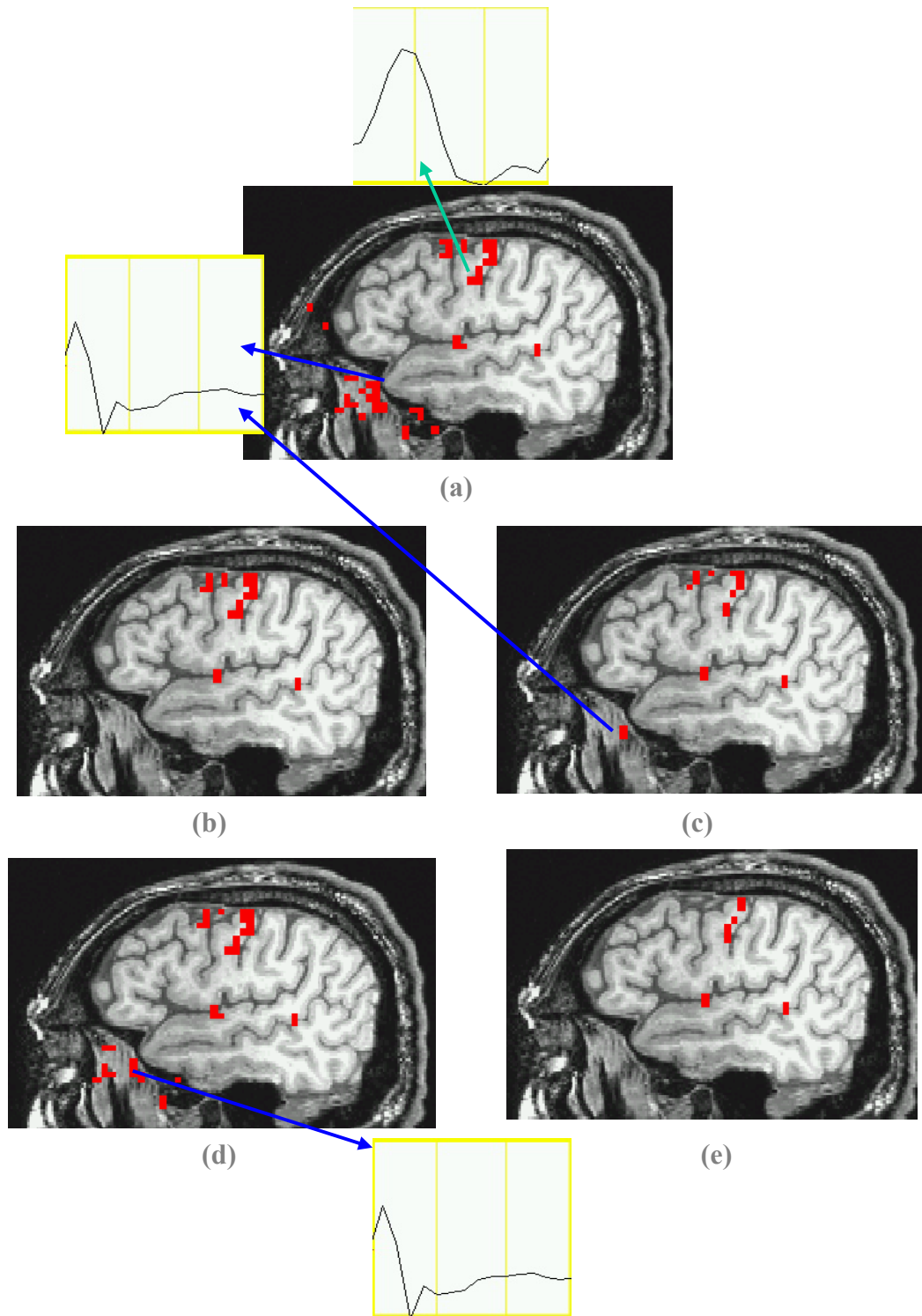


Figure 5.5: Activation maps thresholded at $R^2 > 0.2$ for patient 1 (post-therapy scan) with no TCM noise-reduction (a), with selective detrending (b), with motion parameter regression (c), with ignoring 2 images after speech (d) and with non-selective detrending (e). The blue arrows indicate TCM voxel IRFs and the green arrows BOLD voxel IRFs.

Some of the estimated TCM IRFs and BOLD HRF for selected voxels are also shown. Figure 5.5(b) shows the map with selective detrending. All the voxels shown activated in the selective detrending map exhibited BOLD HRF responses. Figures 5.5 (c-e) show the R^2 -activation map for the same patient under the same scan after motion parameter regression, ignoring two images after speech and non-selective detrending. All the voxels activated above a threshold $R^2 > 0.20$ (corresponding to p-value $< 10^{-20}$) shown in red. All the activated voxels in the selective detrending map (Figure 5.5 (b)) exhibited BOLD HRF similar to the one shown by the green arrow in Figure 5.5 (b) (which shows activation in the motor strip). Figure 5.5 (a) shows a lot of TCM corrupted false-positive voxels, particularly in the inferior and frontal regions. A few representative TCM impulse responses are shown by the blue arrows. From the figures (5.5 (a-e)) for the 5 cases it can be noted that for this subject the motion-parameter regression (MPR) method and the ML2 method do not perform well with regard to TCM noise reduction. The non-selective detrending method seems to reduce true-positive BOLD MR signal along with TCM noise. The selective detrending method seems to work the best in terms of retention of true-positives and reduction of false-positives.

Figure 5.6 (a) shows some representative TCM IRFs extracted from the patient 1 (post-therapy scan) dataset. There are a lot of similarities in the motion responses. Some of the TCM IRFs (e.g. the red curve) are shifted relative to the time of onset. Some of responses (blue) have significant longer lasting effects.

Figure 5.6 (b) shows the effect of applying the reviewed methods of TCM noise reduction on a BOLD activation voxel in the right lateral-frontal region of aphasia patient 1 (post-therapy scan). This voxels hemodynamic response has an ‘early’ onset.

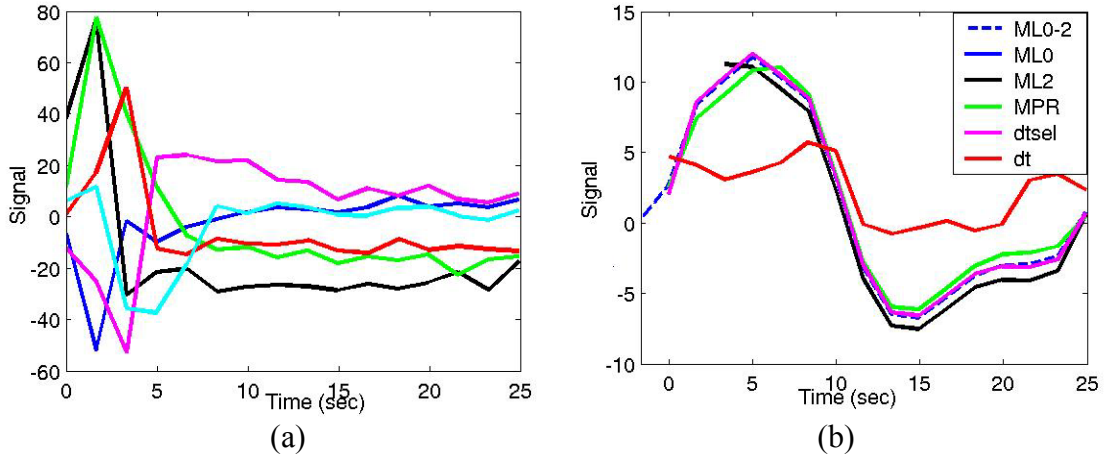


Figure 5.6: Some representative TCM-related voxel IRFs from patient 1 post-therapy scan (a). The effect of the methods of noise correction on a right medial-frontal voxel BOLD HRF exhibiting an ‘early’ response for the same dataset (b). The no-correction curve is hidden by the selective detrending curve.

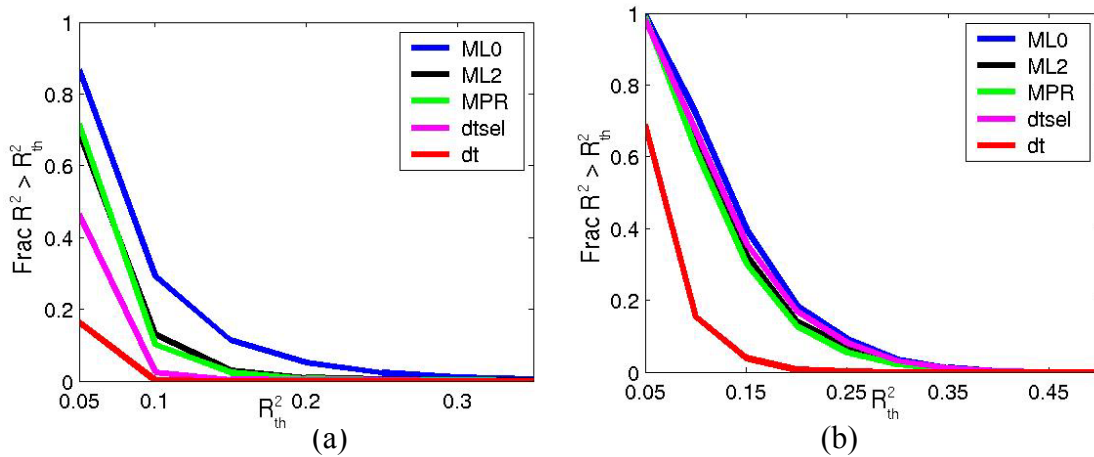


Figure 5.7: Fraction of voxels detected as a function threshold R^2 for (a) the false-positives test-bed and (b) the true-positives test-bed for aphasia patient 1 (post-therapy scan). The blue curve (ML0) represents the case of no motion correction, the black curve (ML2) represents the method of ignoring first 2 images after speech, the green curve (MPR) represents the motion-parameter regression method, the magenta curve (dtsel) represents the selective detrending method and the red curve (dt) represents the non-selective detrending method.

The blue dashed curve (ML0-2) in Figure 5.6 (b) (which has been generated by shifting the response-locked stimulus vector back by two images) suggests that the HRF has started prior to word-enunciation. It is obvious from the Figure 5.6(b) that the method of ignoring two images during speech (ML2, black) suffers from a lack of sensitivity to the early portion of the hemodynamic response, since the method ignores the first two images. The non-selective detrending method (dt, red) removes BOLD MR signal in this voxel and hence is sub-optimal. The selective detrending method (dtsel, magenta) does not perform any detrending on this voxel and leaves the BOLD signal intact. The motion parameter regression method (MPR, green) also seems to leave the BOLD MR signal intact in this voxel.

The modified ROC analyses for this fMRI dataset is illustrated in Figures 5.7 (a-b). The efficiency of TCM noise reduction of all the four methods as well as for the case of no motion correction is shown in Figure 5.7(a) for aphasia patient 2 (post-therapy scan). The non-selective detrending method (dt; red curve) performs the best in terms of reducing TCM false-positives. The selective detrending method (dtsel; magenta) performs better than the method of ignoring images (ML2; black) as well as the motion-parameter regression method (MPR; green). The MPR and ML2 method curves look similar. The case with no motion correction (ML0; blue) is also shown for reference.

Figure 5.7 (b) shows the effect of each of the TCM noise reduction treatments on the test-bed of the true-positive BOLD HRF-like voxels. There does not seem to be much difference in the true-positives retention capacity between the MPR, ML2 and selective detrending methods. The non-selective detrending method seems to suffer from a loss of

sensitivity to BOLD MR signal. By considering this graph along with the TCM noise reduction graph of Figure 5.7 (a) one can state that the selective detrending method performs the best in terms of TCM noise reduction and true positive BOLD HRF retention.

Patient 2 (Pre-Treatment)

The Figure 5.8(a) shows a medial sagittal slice of a high-resolution T1-weighted anatomic image with the R^2 -activation map overlay for the aphasia-patient-2 (under pre-treatment condition), without TCM noise reduction. Some of the estimated TCM IRFs and BOLD HRF for selected voxels are also shown. Figure 5.8(b) shows the map with selective detrending. All the voxels shown activated in the selective detrending map exhibited BOLD HRF responses. The green arrow in the figure points away from activation in the right anterior putamen region, which is implicated in word-generation. The selective detrending method is able to attenuate the motion-corrupted portion of the hemodynamic response. Figures 5.8 (c-e) show the R^2 -activation map for the same patient under the same scan after motion parameter regression, ignoring two images after speech and non-selective detrending. All the voxels activated above a threshold $R^2 > 0.20$ (corresponding to p-value $< 10^{-20}$) shown in red. All the activated voxels in the selective detrending map (Figure 5.8 (b)) exhibited BOLD HRF similar to the one shown by the green arrow in Figure 5.8 (b). Figure 5.8 (a) shows a lot of TCM corrupted false-positive voxels, particularly in the inferior and frontal regions. A few representative TCM impulse responses are shown by the blue arrows. From the figures (5.8 (a-e)) for the 5 cases it can be noted that for this subject the motion-parameter regression (MPR) method as well as the ignoring images method (ML2) show residual TCM-related false-positives event after noise-reduction. The non-selective detrending method seems to reduce true-positive

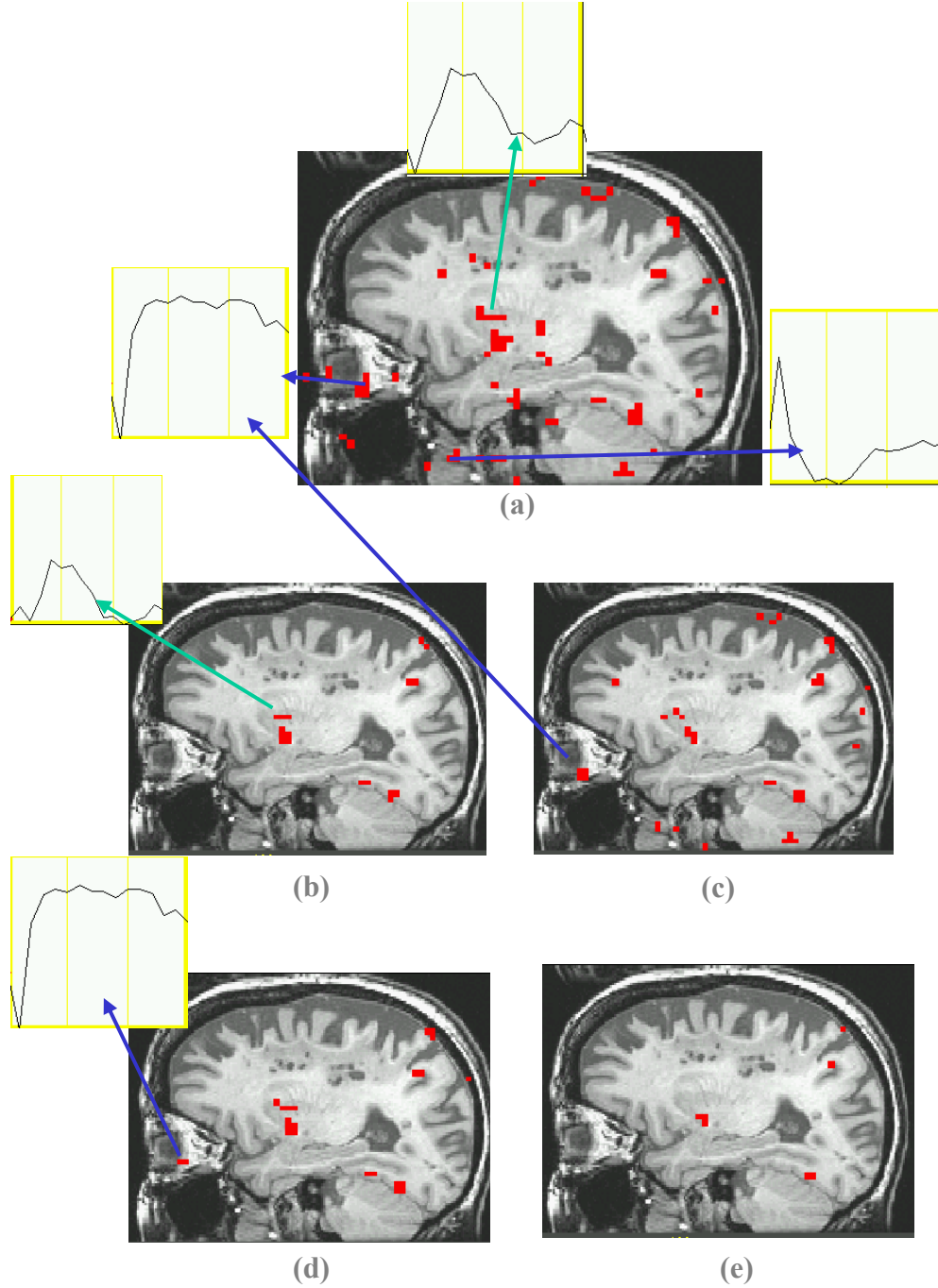


Figure 5.8: Activation maps thresholded at $R^2 > 0.2$ for patient-2 (pre-therapy scan) with no TCM noise-reduction (a), with selective detrending (b), with motion parameter regression (c), with ignoring 2 images after speech (d) and with non-selective detrending (e). The blue arrows indicate TCM voxel IRFs and the green arrows BOLD voxel IRFs.

BOLD MR signal along with TCM noise. The selective detrending method seems to work the best in terms of retention of true-positives and reduction of false-positives.

Figure 5.9 (a) shows some representative TCM IRFs extracted from the patient 2 (pre-therapy scan) dataset. There are a lot of similarities in the TCM responses. Some of the TCM IRFs are shifted relative to the time of onset and some have significant longer lasting effects.

Figure 5.9 (b) shows the effect of applying the reviewed methods of TCM noise reduction on a right medial-frontal BOLD activation voxel in aphasia patient 2 (pre-therapy scan). This voxel's hemodynamic response has an 'early' onset. The blue dashed curve (ML0-2) in Figure 5.9 (b) (which has been generated by shifting the response-locked stimulus vector back by two images) suggests that the HRF has started prior to word-enunciation. It is obvious from the Figure 5.9 (b) that the method of ignoring two images during speech (ML2, black) suffers from a lack of sensitivity to the early portion of the hemodynamic response, since the method ignores the first two images. There also seems to be a slight decrease in the amplitude of the response for the ML2 curve. This could be due to the use of an unbiased estimator in deconvolution analysis. The non-selective detrending method (dt, red) removes BOLD MR signal in this voxel and hence is sub-optimal. The selective detrending method (dtsel, magenta) does not perform any detrending on this voxel and leaves the BOLD signal intact. The motion parameter regression method (MPR, green) also leads to a reduced HRF amplitude.

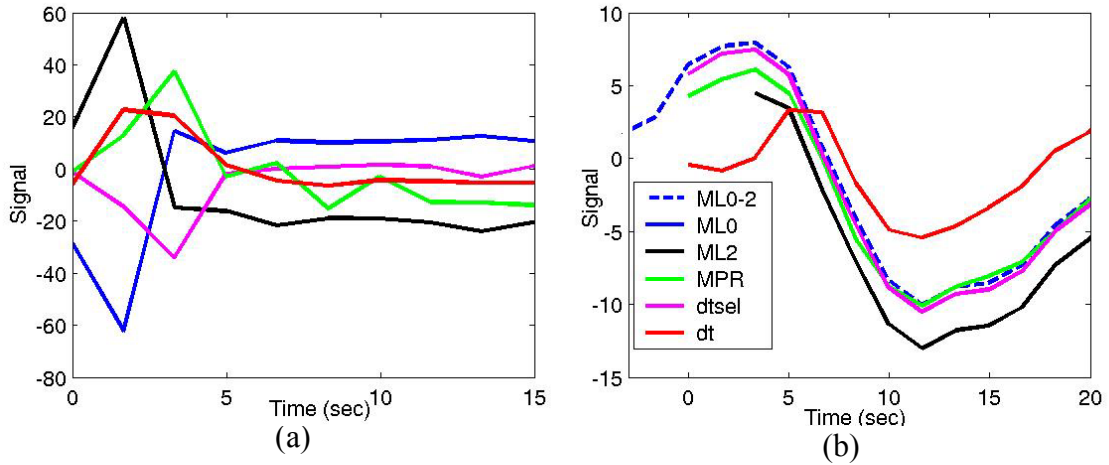


Figure 5.9: Some representative TCM-related voxel IRFs from patient 2 pre-therapy scan (a). The effect of the methods of noise correction on a right medial-frontal voxel BOLD HRF exhibiting an ‘early’ response for the same dataset (b). The no-correction curve is hidden by the selective detrending curve.

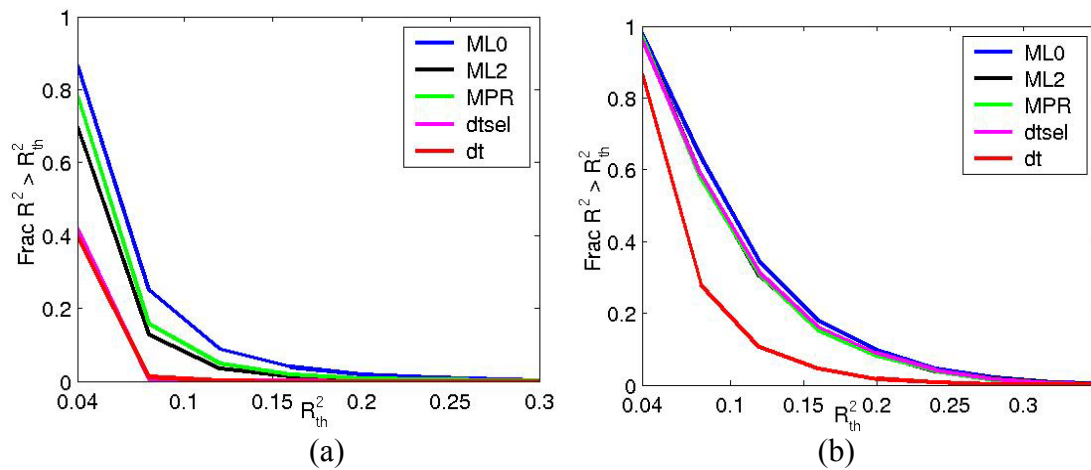


Figure 5.10: Fraction of voxels detected as a function threshold R_2 for (a) the false-positives test-bed and (b) the true-positives test-bed for aphasia patient 2 (pre-therapy scan). The blue curve (ML0) represents the case of no motion correction, the black curve (ML2) represents the method of ignoring first 2 images after speech, the green curve (MPR) represents the motion-parameter regression method, the magenta curve (dtsel) represents the selective detrending method and the red curve (dt) represents the non-selective detrending method.

The modified ROC analyses for this study is illustrated in Figures 5.10 (a-b). The efficiency of TCM noise reduction of all the four methods as well as for the case of no motion correction is shown in Figure 5.10 (a). The selective detrending method (dtsel; magenta) performs almost as well as the non-selective detrending method (dt; red) in terms of reducing TCM false-positives. The method of ignoring images (ML2; black) and the motion-parameter regression method (MPR; green) look similar and are less optimal. The case with no motion correction (ML0; blue) is also shown for reference.

Figure 5.10 (b) shows the effect of each of the TCM noise reduction treatments on the test-bed of the true-positive BOLD HRF-like voxels. The distributions look similar except for the non-selective detrending method. The non-selective detrending method seems to suffer from a loss of sensitivity to BOLD MR signal. By considering this graph along with the TCM noise reduction graph of Figure 5.10 (a) one can state that the selective detrending method performs the best in terms of TCM noise reduction and true positive BOLD HRF retention.

Patient 2 (Post-Treatment)

The Figure 5.11 (a) shows a lateral sagittal slice of a high-resolution T1-weighted anatomic image with the R^2 -activation map overlay for the aphasia-patient-2 (under post-treatment condition), without TCM noise reduction. Some of the estimated TCM IRFs and BOLD HRF for selected voxels are also shown. Figure 5.11(b) shows the map with selective detrending. All the voxels shown activated in the selective detrending map exhibited BOLD HRF responses. The green arrow in the figure points away from activation in the motor strip, which is implicated in word-generation. Figures 5.11 (c-e) show the R^2 -activation map for the same patient under the same scan after motion parameter regression, ignoring two images after speech and non-selective

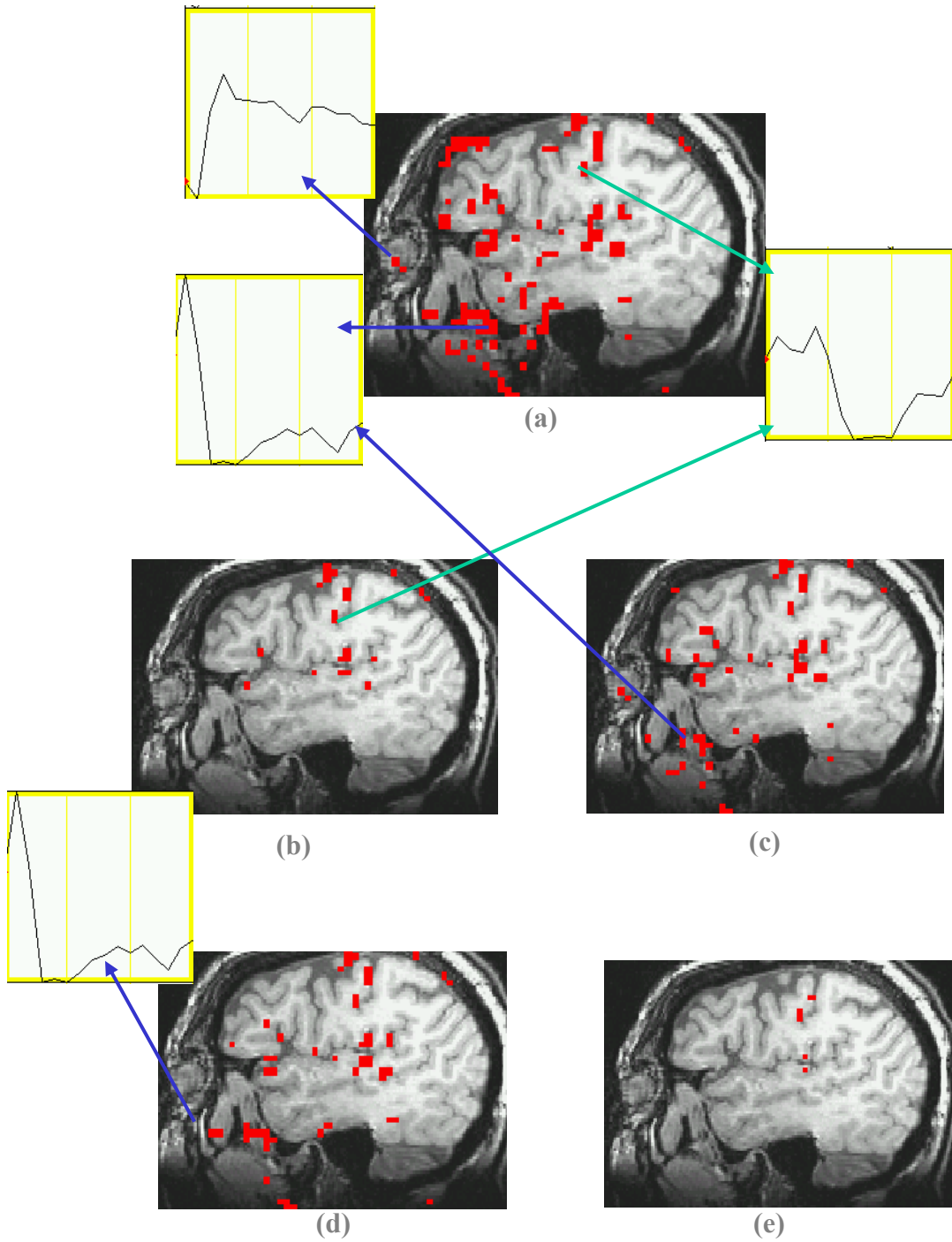


Figure 5.11: Activation maps thresholded at $R^2 > 0.2$ for patient 2 (post-therapy scan) with no TCM noise-reduction (a), with selective detrending (b), with motion parameter regression (c), with ignoring 2 images after speech (d) and with non-selective detrending (e). The blue arrows indicate TCM voxel IRFs and the green arrows BOLD voxel IRFs.

detrending. All the voxels activated above a threshold $R^2 > 0.20$ (corresponding to p-value $< 10^{-20}$) shown in red. All the activated voxels in the selective detrending map (Figure 5.11 (b)) exhibited BOLD HRF similar to the one shown by the green arrow in Figure 5.11 (b). Figure 5.11 (a) shows a lot of TCM corrupted false-positive voxels, particularly in the inferior and frontal regions. A few representative TCM impulse responses are shown by the blue arrows. From the figures (5.11 (a-e)) for the 5 cases it can be noted that for this subject the motion-parameter regression (MPR) method as well as the ignoring images method (ML2) show residual TCM-related false-positives event after noise-reduction. The non-selective detrending method seems to reduce true-positive BOLD MR signal along with TCM noise. The selective detrending method seems to work the best in terms of retention of true-positives and reduction of false-positives.

Figure 5.12 (a) shows some representative TCM IRFs extracted from the patient 2 (pre-therapy scan) dataset. There are a lot of similarities in the TCM responses. Some of the TCM IRFs are shifted relative to the time of onset and some have significant longer lasting effects.

Figure 5.12 (b) shows the effect of applying the reviewed methods of TCM noise reduction on a right medial-frontal BOLD activation voxel in aphasia patient 2 (post-therapy scan). This voxels hemodynamic response has an ‘early’ onset. The blue dashed curve (ML0-2) in Figure 5.12 (b) (which has been generated by shifting the response-locked stimulus vector back by one image) suggests that the HRF has started prior to word-enunciation. It is obvious from the Figure 5.12 (b) that the method of ignoring two images during speech (ML2, black) suffers from a lack of sensitivity to the early portion of the hemodynamic response, since the method ignores the first two images. There also

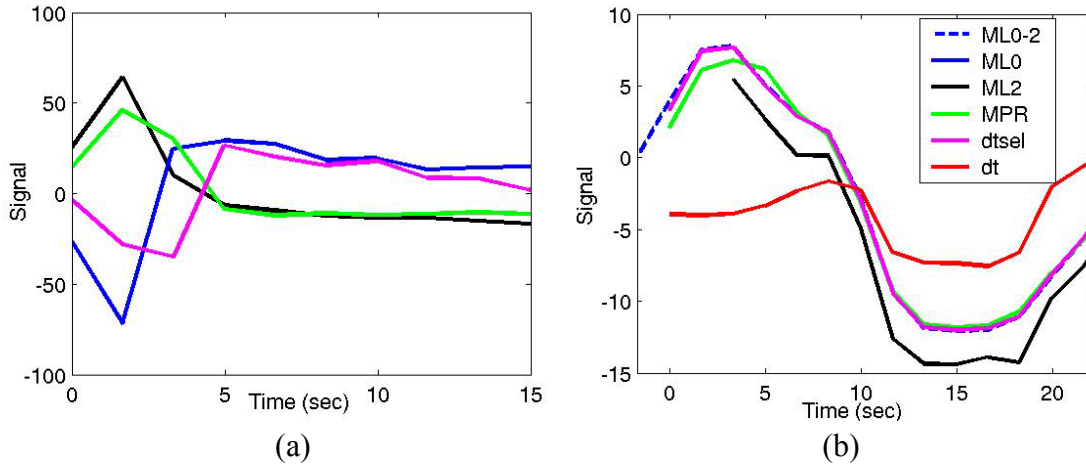


Figure 5.12: Some representative TCM-related voxel IRFs from patient 2 post-therapy scan (a). The effect of the methods of noise correction on a right medial-frontal voxel BOLD HRF exhibiting an ‘early’ response for the same dataset (b). The no-correction curve is hidden by the selective detrending curve.

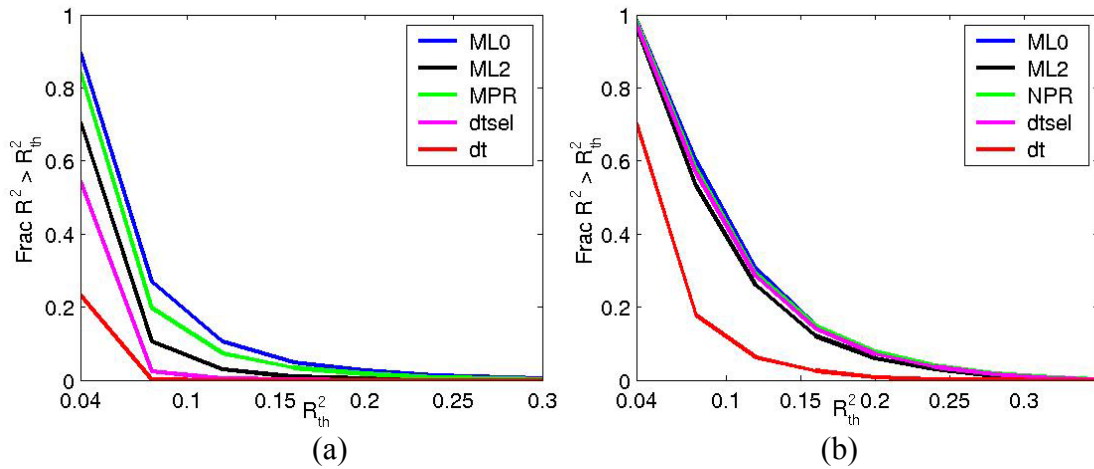


Figure 5.13: Fraction of voxels detected as a function threshold R^2 for (a) the false-positives test-bed and (b) the true-positives test-bed for aphasia patient 2 (post-therapy scan). The blue curve (ML0) represents the case of no motion correction, the black curve (ML2) represents the method of ignoring first 2 images after speech, the green curve (MPR) represents the motion-parameter regression method, the magenta curve (dtsel) represents the selective detrending method and the red curve (dt) represents the non-selective detrending method.

seems to be a slight decrease in the amplitude of the response for the ML2 curve. This could be due to the use of an unbiased estimator in deconvolution analysis. The non-selective detrending method (dt, red) removes BOLD MR signal in this voxel and hence is sub-optimal. The selective detrending method (dtsel, magenta) does not perform any detrending on this voxel and leaves the BOLD signal intact. The motion parameter regression method (MPR, green) also leads to a reduced HRF amplitude.

The modified ROC analyses for the aphasia patient 2 (post-therapy scan) is illustrated in Figures 5.13 (a-b). The efficiency of TCM noise reduction of all the four methods as well as for the case of no motion correction is shown in Figure 5.13 (a). The non-selective detrending method (dt; red curve) performs the best in terms of reducing TCM false-positives. The selective detrending method (dtsel; magenta) performs better than the method of ignoring images (ML2; black) as well as the motion-parameter regression method (MPR; green). The ML2 method performs slightly better than the MPR method. The case with no motion correction (ML0; blue) is also shown for reference.

Figure 5.13 (b) shows the effect of each of the TCM noise reduction treatments on the test-bed of the true-positive BOLD HRF-like voxels. The distributions look similar except for the non-selective detrending method. The non-selective detrending method seems to suffer from a loss of sensitivity to BOLD MR signal. By considering this graph along with the TCM noise reduction graph of Figure 5.13 (a) one can state that the selective detrending method performs the best in terms of TCM noise reduction and true positive BOLD HRF retention.

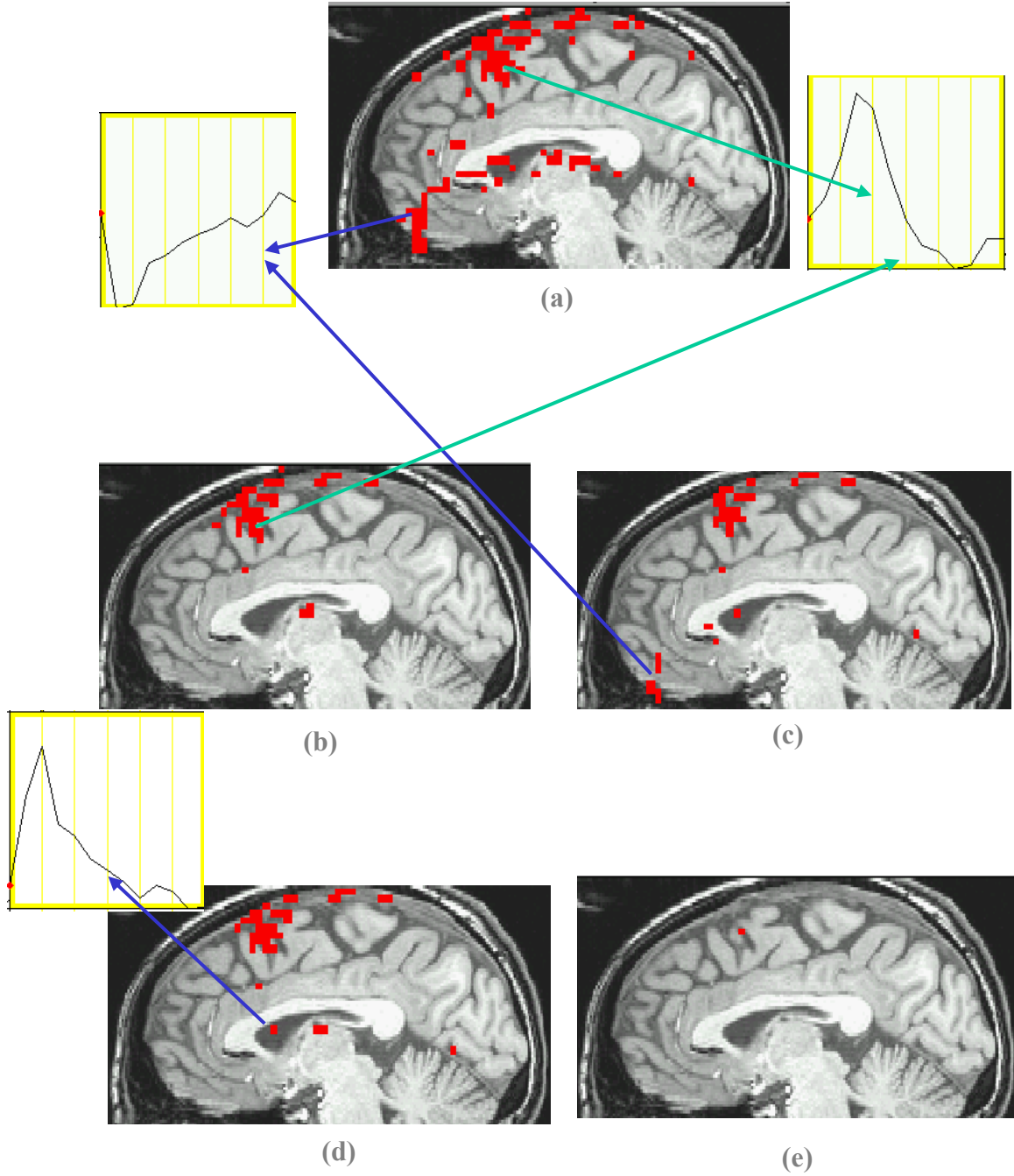


Figure 5.14: Activation maps thresholded at $R^2 > 0.2$ for control subject 1 with no TCM noise-reduction (a), with selective detrending (b), with motion parameter regression (c), with ignoring 2 images after speech (d) and with non-selective detrending (e). The blue arrows indicate TCM voxel IRFs and the green arrows BOLD voxel IRFs.

Control Subject 1

The Figure 5.14 (a) shows a medial sagittal slice of a high-resolution T1-weighted anatomic image with the R^2 -activation map overlay for the control subject 1, without TCM noise reduction. Some of the estimated TCM IRFs and BOLD HRF for selected voxels are also shown. Figure 5.14(b) shows the map with selective detrending. All the voxels shown activated in the selective detrending map exhibited BOLD HRF responses. The green arrow in the figure points away from activation in the right medial frontal region, which is implicated in word-generation. Figures 5.14 (c-e) show the R^2 -activation map for the same subject under the same scan after motion parameter regression, ignoring two images after speech and non-selective detrending. All the voxels activated above a threshold $R^2 > 0.20$ (corresponding to p-value $< 10^{-20}$) shown in red. All the activated voxels in the selective detrending map (Figure 5.14 (b)) exhibited BOLD HRF similar to the one shown by the green arrow in Figure 5.14 (b). Figure 5.14 (a) shows a lot of TCM corrupted false-positive voxels, particularly in the inferior and frontal regions. A few representative TCM impulse responses are shown by the blue arrows. From the figures (5.14 (a-e)) for the 5 cases it can be noted that for this subject the motion-parameter regression (MPR) method as well as the ignoring images method (ML2) show residual TCM-related false-positives event after noise-reduction. The non-selective detrending method seems to reduce true-positive BOLD MR signal along with TCM noise. The selective detrending method seems to work the best in terms of retention of true-positives and reduction of false-positives.

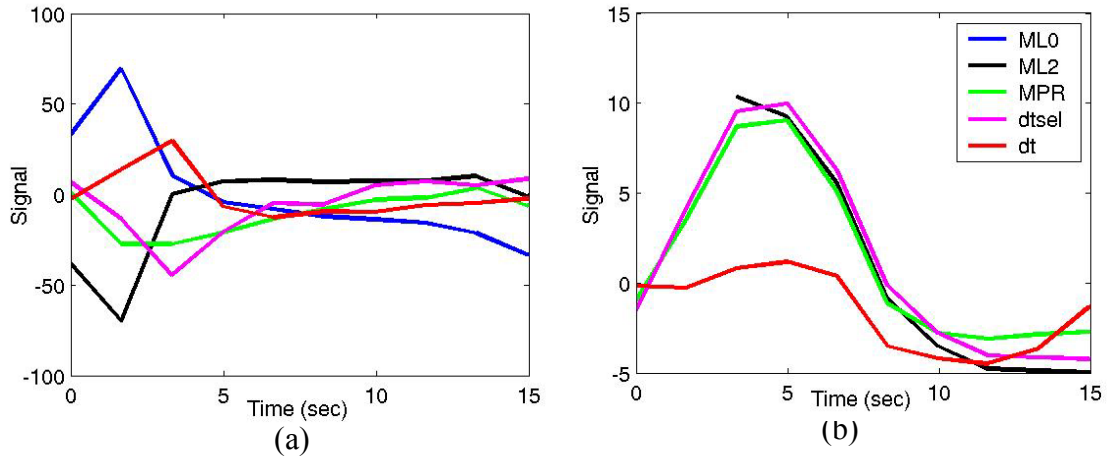


Figure 5.15: Some representative TCM-related voxel IRFs from control subject 1. The effect of the methods of noise correction on a right medial-frontal voxel BOLD HRF exhibiting an 'early' response for the same dataset (b). The no-correction curve is hidden by the selective detrending curve.

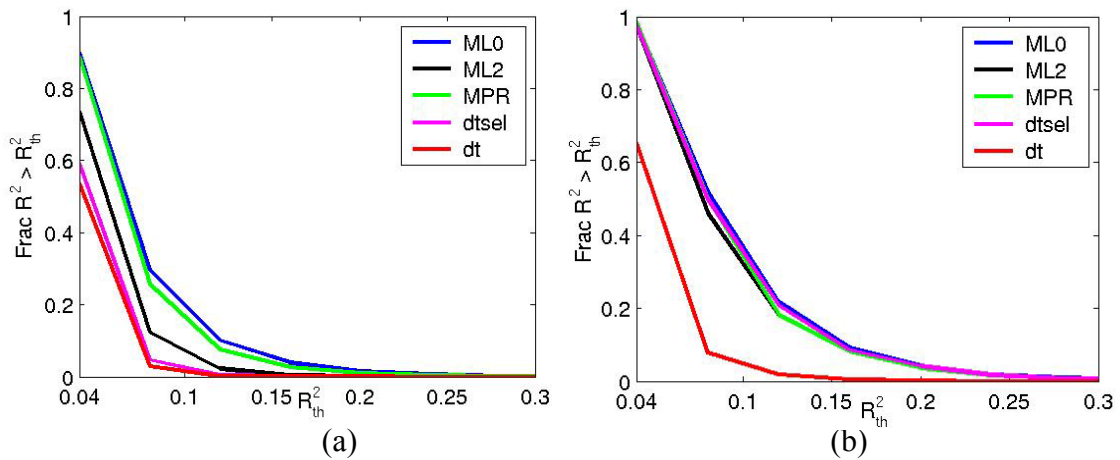


Figure 5.16: Fraction of voxels detected as a function threshold R^2 for (a) the false-positives test-bed and (b) the true-positives test-bed for control subject 1. The blue curve (ML0) represents the case of no motion correction, the black curve (ML2) represents the method of ignoring first 2 images after speech, the green curve (MPR) represents the motion-parameter regression method, the magenta curve (dtsel) represents the selective detrending method and the red curve (dt) represents the non-selective detrending method.

Figure 5.15 (a) shows some representative TCM IRFs extracted from the control subject 1 dataset. There are a lot of similarities in the TCM responses. Some of the TCM IRFs are shifted relative to the time of onset and some have significant longer lasting effects.

Figure 5.15 (b) shows the effect of applying the reviewed methods of TCM noise reduction on a right medial-frontal BOLD activation voxel in control subject 1. This voxels hemodynamic response has an ‘early’ onset. It is obvious from the Figure 5.15 (b) that the method of ignoring two images during speech (ML2, black) suffers from a lack of sensitivity to the early portion of the hemodynamic response, since the method ignores the first two images. The non-selective detrending method (dt, red) removes BOLD MR signal in this voxel and hence is sub-optimal. The selective detrending method (dtsel, magenta) does not perform any detrending on this voxel and leaves the BOLD signal intact. The motion parameter regression method (MPR, green) leads to a slightly reduced HRF amplitude.

The modified ROC analyses for the control subject 1 is illustrated in Figures 5.16 (a-b). The efficiency of TCM noise reduction of all the four methods as well as for the case of no motion correction is shown in Figure 5.16 (a). The selective detrending method (dtsel; magenta) performs almost as well as the non-selective detrending method (dt; red) in terms of reducing TCM false-positives. The method of ignoring images (ML2; black) is less optimal. The motion-parameter-regression method (MPR; green) does not show much improvement over the no-correction case (ML0; blue).

Figure 5.16 (b) shows the effect of each of the TCM noise reduction treatments on the test-bed of the true-positive BOLD HRF-like voxels. The distributions look similar

except for the non-selective detrending method. The non-selective detrending method seems to suffer from a loss of sensitivity to BOLD MR signal. By considering this graph along with the TCM noise reduction graph of Figure 5.16 (a) one can state that the selective detrending method performs the best in terms of TCM noise reduction and true positive BOLD HRF retention.

Control Subject 2

The Figure 5.17 (a) shows a lateral sagittal slice of a high-resolution T1-weighted anatomic image with the R^2 -activation map overlay for the control subject 2, without TCM noise reduction. Some of the estimated TCM IRFs and BOLD HRF for selected voxels are also shown. Figure 5.17(b) shows the map with selective detrending. All the voxels shown activated in the selective detrending map exhibited BOLD HRF responses. The green arrow (pointing right in Figure 5.17 (a)) points away from activation in the right middle frontal region, which is implicated in word-generation. The green arrow in Figure 5.17 (b) points away from a broca's area voxel which exhibits an 'early response'. The activation maps of the other 3 methods do not exhibit this voxel. Figures 5.17 (c-e) show the R^2 -activation map for the same subject under the same scan after motion parameter regression, ignoring two images after speech and non-selective detrending. All the voxels activated above a threshold $R^2 > 0.20$ (corresponding to p-value $< 10^{-20}$) shown in red. All the activated voxels in the selective detrending map (Figure 5.17 (b)) exhibited BOLD HRF similar to the one shown by the green arrow in Figure 5.17 (a). Figure 5.17 (a) shows a lot of TCM corrupted false-positive voxels, particularly in the inferior and frontal regions. A few representative TCM impulse responses are shown by the blue arrows. From the figures (5.17 (a-e)) for the 5 cases it can be noted that for this subject the motion-parameter regression (MPR) method as well

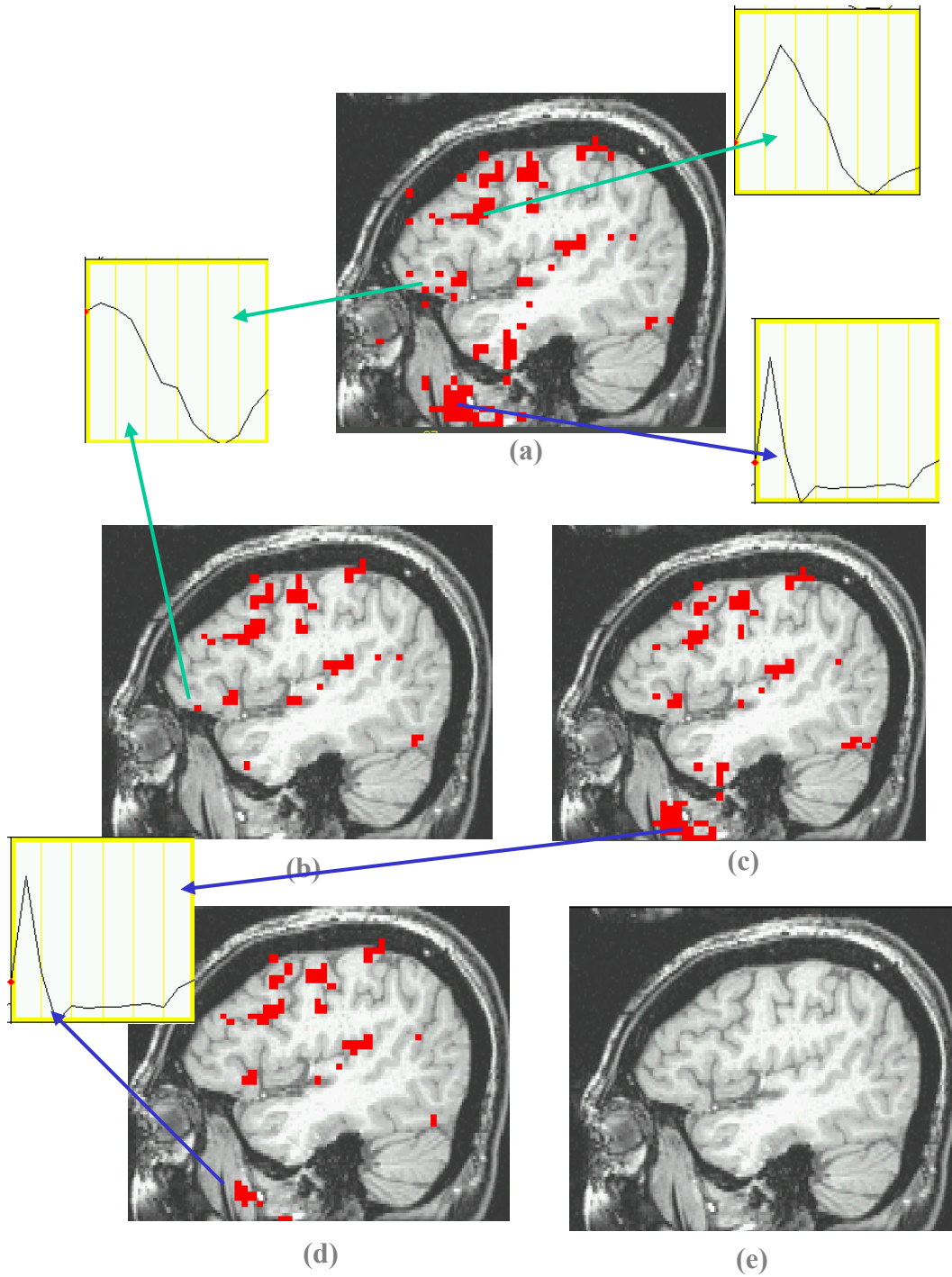


Figure 5.17: Activation maps thresholded at $R^2 > 0.2$ for control subject-2 with no TCM noise-reduction (a), with selective detrending (b), with motion parameter regression (c), with ignoring 2 images after speech (d) and with non-selective detrending (e). The blue arrows indicate TCM voxel IRFs and the green arrows BOLD voxel IRFs.

as the ignoring images method (ML2) show residual TCM-related false-positives event after noise-reduction. The non-selective detrending method seems to reduce true-positive BOLD MR signal along with TCM noise. The selective detrending method seems to work the best in terms of retention of true-positives and reduction of false-positives.

Figure 5.18 (a) shows some representative TCM IRFs extracted from the control subject 2 dataset. There are a lot of similarities in the TCM responses. Some of the TCM IRFs are shifted relative to the time of onset and some have significant longer lasting effects.

Figure 5.18 (b) shows the effect of applying the reviewed methods of TCM noise reduction on a right medial-frontal BOLD activation voxel in control subject 2. This voxels hemodynamic response has an ‘early’ onset. It is obvious from the Figure 5.18 (b) that the method of ignoring two images during speech (ML2, black) suffers from a lack of sensitivity to the early portion of the hemodynamic response, since the method ignores the first two images. There seems to be a slight decrease in the amplitude of the response for the ML2 curve. This could be due to the use of an unbiased estimator in deconvolution analysis. The non-selective detrending method (dt, red) removes BOLD MR signal in this voxel and hence is sub-optimal. The selective detrending method (dtsel, magenta) does not perform any detrending on this voxel and leaves the BOLD signal intact. The motion parameter regression method (MPR, green) also leads to a slightly reduced HRF amplitude.

The modified ROC analyses for the control subject 2 is illustrated in Figures 5.19 (a-b). The efficiency of TCM noise reduction of all the four methods as well as for the case of no motion correction is shown in Figure 5.19 (a). The non-selective detrending

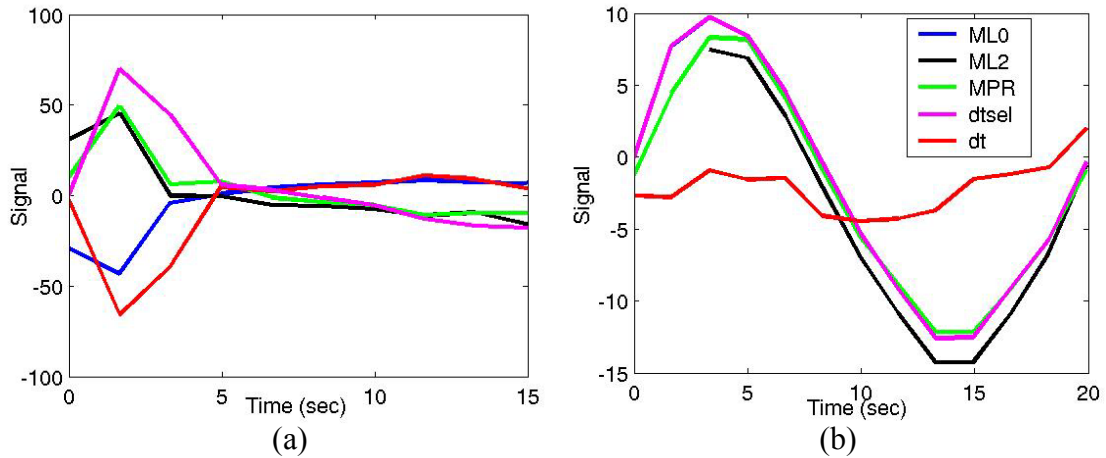


Figure 5.18: Some representative TCM-related voxel IRFs from control subject 2 (a). The effect of the methods of noise correction on a right medial-frontal voxel BOLD HRF exhibiting an ‘early’ response for the same dataset (b). The no-correction curve is hidden by the selective detrending curve.

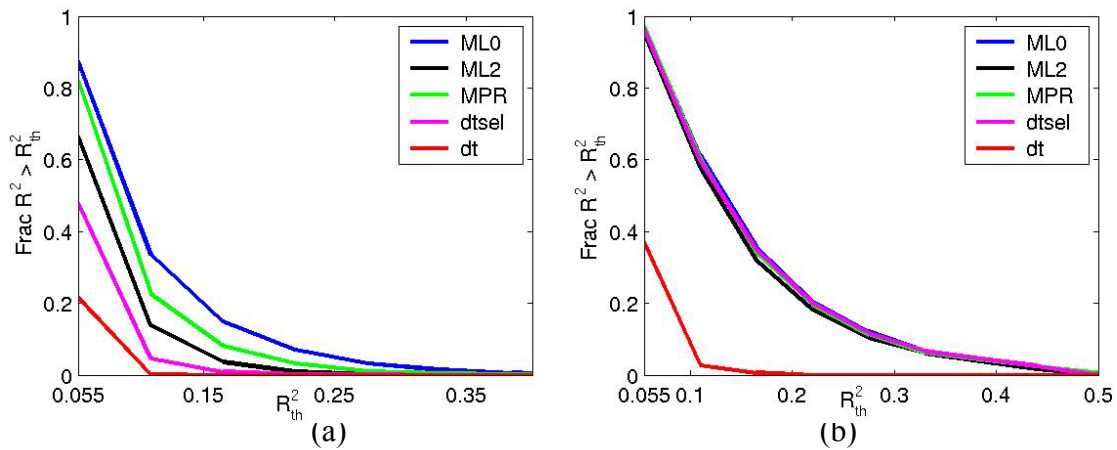


Figure 5.19: Fraction of voxels detected as a function threshold R^2 for (a) the false-positives test-bed and (b) the true-positives test-bed for control subject 2. The blue curve (ML0) represents the case of no motion correction, the black curve (ML2) represents the method of ignoring first 2 images after speech, the green curve (MPR) represents the motion-parameter regression method, the magenta curve (dtsel) represents the selective detrending method and the red curve (dt) represents the non-selective detrending method.

method (dt; red curve) performs the best in terms of reducing TCM false-positives. The selective detrending method (dtsel; magenta) performs better than the method of ignoring images (ML2; black) as well as the motion-parameter regression method (MPR; green). The ML2 method performs slightly better than the MPR method. The no-correction curve (ML0; blue) is also given for reference.

Figure 5.19 (b) shows the effect of each of the TCM noise reduction treatments on the test-bed of the true-positive BOLD HRF-like voxels. The distributions look similar except for the non-selective detrending method. The non-selective detrending method seems to suffer from a loss of sensitivity to BOLD MR signal. By considering this graph along with the TCM noise reduction graph of Figure 5.19 (a) one can state that the selective detrending method performs the best in terms of TCM noise reduction and true positive BOLD HRF retention.

Control Subject 3

The Figure 5.20 (a) shows a lateral sagittal slice of a high-resolution T1-weighted anatomic image with the R^2 -activation map overlay for the control subject 3, without TCM noise reduction. Some of the estimated TCM IRFs and BOLD HRF for selected voxels are also shown. Figure 5.20(b) shows the map with selective detrending. All the voxels shown activated in the selective detrending map exhibited BOLD HRF responses. The green arrow (pointing right in Figure 5.20 (b)) points away from activation in the motor strip, which is implicated in word-generation. The green arrow (pointing left) in Figure 5.20 (b) points away from an inferior frontal sulcus voxel which exhibits an ‘early response’. The activation maps of the other 3 methods do not exhibit this voxel. Figures 5.20 (c-e) show the R^2 -activation map for the same subject under the same scan after motion parameter regression, ignoring two images after speech and non-selective

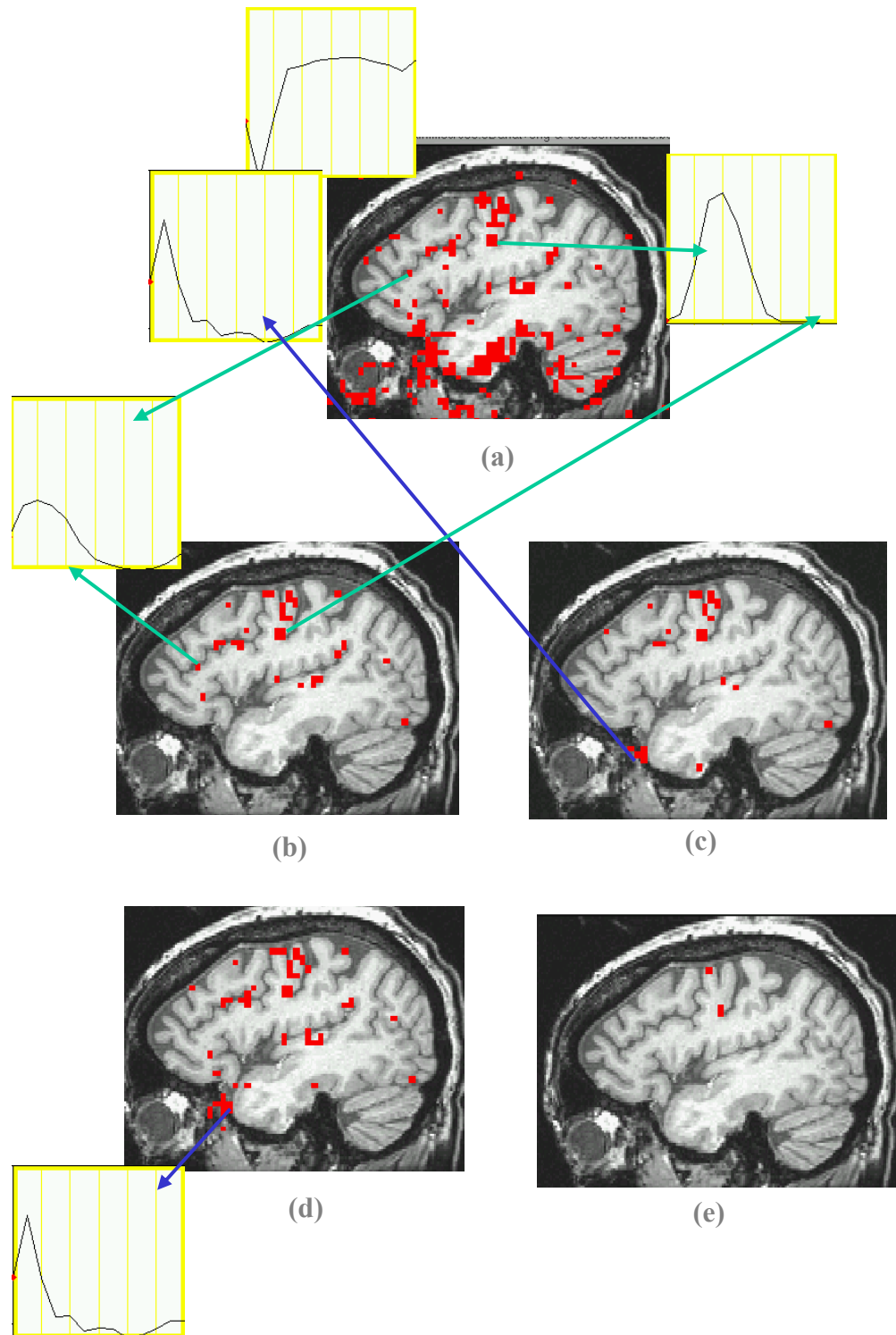


Figure 5.20: Activation maps thresholded at $R^2 > 0.2$ for control subject 3 with no TCM noise-reduction (a), with selective detrending (b), with motion parameter regression (c), with ignoring 2 images after speech (d) and with non-selective detrending (e). The blue arrows indicate TCM voxel IRFs and the green arrows BOLD voxel IRFs.

detrending. All the voxels activated above a threshold $R^2 > 0.20$ (corresponding to p-value $< 10^{-20}$) shown in red. All the activated voxels in the selective detrending map (Figure 5.20 (b)) exhibited BOLD HRF similar to the one shown by the green arrows in Figure 5.20 (a). Figure 5.20 (a) shows a lot of TCM corrupted false-positive voxels, particularly in the inferior and frontal regions. A few representative TCM impulse responses are shown by the blue arrows. From the figures (5.20 (a-e)) for the 5 cases it can be noted that for this subject the motion-parameter regression (MPR) method as well as the ignoring images method (ML2) show residual TCM-related false-positives event after noise-reduction. The non-selective detrending method seems to reduce true-positive BOLD MR signal along with TCM noise. The selective detrending method seems to work the best in terms of retention of true-positives and reduction of false-positives.

Figure 5.21 (a) shows some representative TCM IRFs extracted from the control subject 3 dataset. There are a lot of similarities in the TCM responses. Some of the TCM IRFs are shifted relative to the time of onset and some have significant longer lasting effects.

Figure 5.21 (b) shows the effect of applying the reviewed methods of TCM noise reduction on a right lateral pre-frontal BOLD activation voxel in control subject 3. This voxel is indicated by the green arrow (pointing left) in Figure 5.20 (b). This voxels hemodynamic response has an ‘early’ onset. The blue dashed curve (ML0-2) in Figure 5.21 (b) (which has been generated by shifting the response-locked stimulus vector back by one image) suggests that the HRF has started prior to word-enunciation. It is obvious from the Figure 5.21 (b) that the method of ignoring two images during speech (ML2; black) suffers from a lack of sensitivity to the early portion of the hemodynamic response

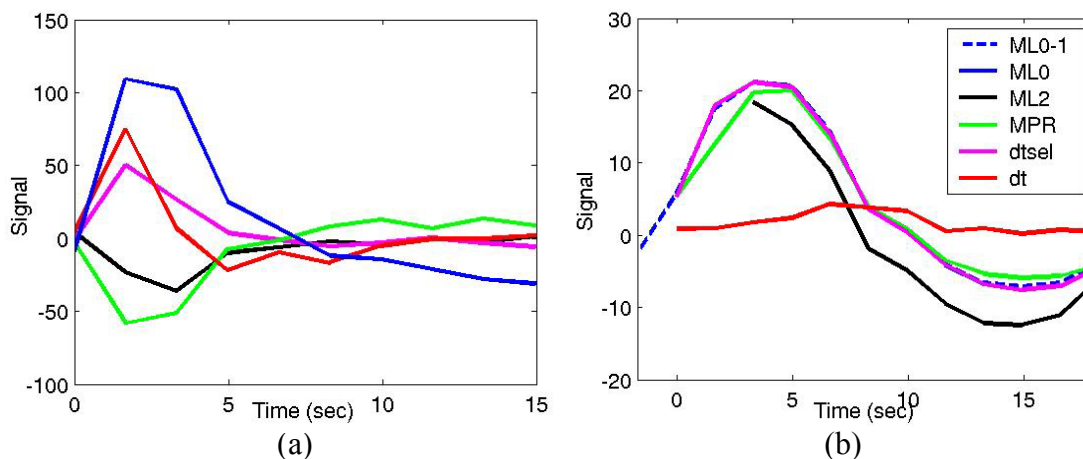


Figure 5.21: Some representative TCM-related voxel IRFs from control subject 3 (a). The effect of the methods of noise correction on a right medial-frontal voxel BOLD HRF exhibiting an ‘early’ response for the same dataset (b). The no-correction curve is hidden by the selective detrending curve.

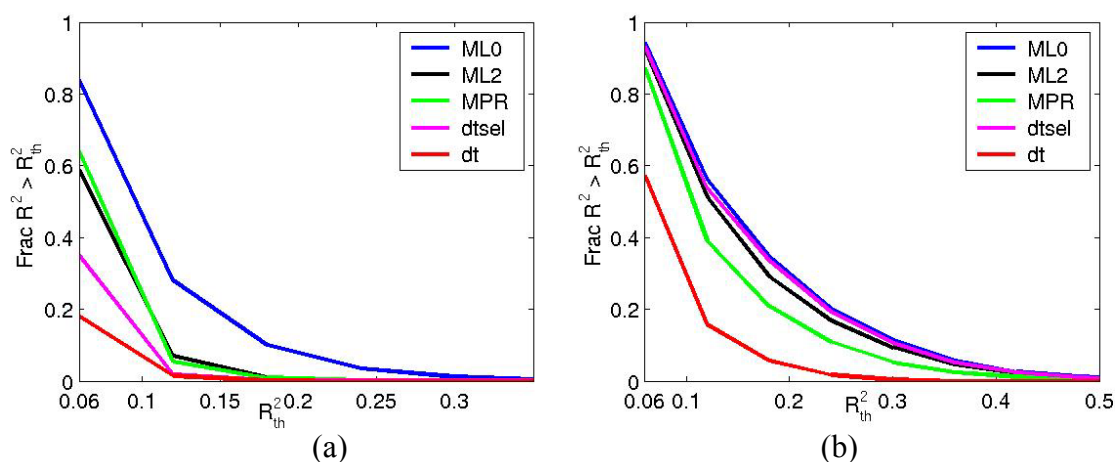


Figure 5.22: Fraction of voxels detected as a function threshold R^2 for (a) the false-positives test-bed and (b) the true-positives test-bed for control subject 3. The blue curve (ML0) represents the case of no motion correction, the black curve (ML2) represents the method of ignoring first 2 images after speech, the green curve (MPR) represents the motion-parameter regression method, the magenta curve (dtsel) represents the selective detrending method and the red curve (dt) represents the non-selective detrending method.

since the method ignores the first two images. There also seems to be a slight decrease in the amplitude of the response for the ML2 curve. This could be due to the use of an unbiased estimator in deconvolution analysis. The non-selective detrending method (dt, red) removes BOLD MR signal in this voxel and hence is sub-optimal. The selective detrending method (dtsel, magenta) does not perform any detrending on this voxel and leaves the BOLD signal intact. The motion parameter regression method (MPR, green) also seems to leave much of the BOLD MR signal intact.

The modified ROC analyses for the control subject 3 is illustrated in Figures 5.22 (a-b). The efficiency of TCM noise reduction of all the four methods as well as for the case of no motion correction is shown in Figure 5.22 (a). The non-selective detrending method (dt; red curve) performs the best in terms of reducing TCM false-positives. The selective detrending method (dtsel; magenta) performs better than the method of ignoring images (ML2; black) as well as the motion-parameter regression method (MPR; green). The curves for the ML2 and the MPR methods look similar. The no-correction curve (ML0; blue) is also given for reference.

Figure 5.22 (b) shows the effect of each of the TCM noise reduction treatments on the test-bed of the true-positive BOLD HRF-like voxels. The distributions for the ML2, selective detrending method and the no-correction case look similar. The non-selective detrending method seems to suffer from a loss of sensitivity to BOLD MR signal. The MPR method too seems to be less sensitive to true-positive BOLD MR signal when compared to the selective detrending and the ML2 methods. By considering this graph along with the TCM noise reduction graph of Figure 5.22 (a) one can state that the

selective detrending method performs the best in terms of TCM noise reduction and true positive BOLD HRF retention.

Control Subject 4

The Figure 5.23 (a) shows a lateral sagittal slice of a high-resolution T1-weighted anatomic image with the R^2 -activation map overlay for the control subject 4, without TCM noise reduction. Some of the estimated TCM IRFs and BOLD HRF for selected voxels are also shown. Figure 5.23(b) shows the map with selective detrending. All the voxels shown activated in the selective detrending map exhibited BOLD HRF responses. The green arrow in Figure 5.23 (a) points away from activation in the inferior parietal region which is implicated in word-generation. The green arrow in Figure 5.23 (b) points away from activation in the primary auditory region. Figures 5.23 (c-e) show the R^2 -activation map for the same subject under the same scan after motion parameter regression, ignoring two images after speech and non-selective detrending. All the voxels activated above a threshold $R^2 > 0.20$ (corresponding to p-value $< 10^{-20}$) shown in red. All the activated voxels in the selective detrending map (Figure 5.23 (b)) exhibited BOLD HRF similar to the one shown by the green arrows in Figure 5.23 (a). Figure 5.23 (a) shows a lot of TCM corrupted false-positive voxels, particularly in the inferior and frontal regions. A few representative TCM impulse responses are shown by the blue arrows. From the figures (5.23 (a-e)) for the 5 cases it can be noted that for this subject the motion-parameter regression (MPR) method performs poorly in reducing noise arising from TCM. The ML2 method performs better than the MPR method, but it also exhibits some residual TCM voxels after TCM noise-reduction. The non-selective detrending method seems to reduce true-positive BOLD MR signal along with TCM

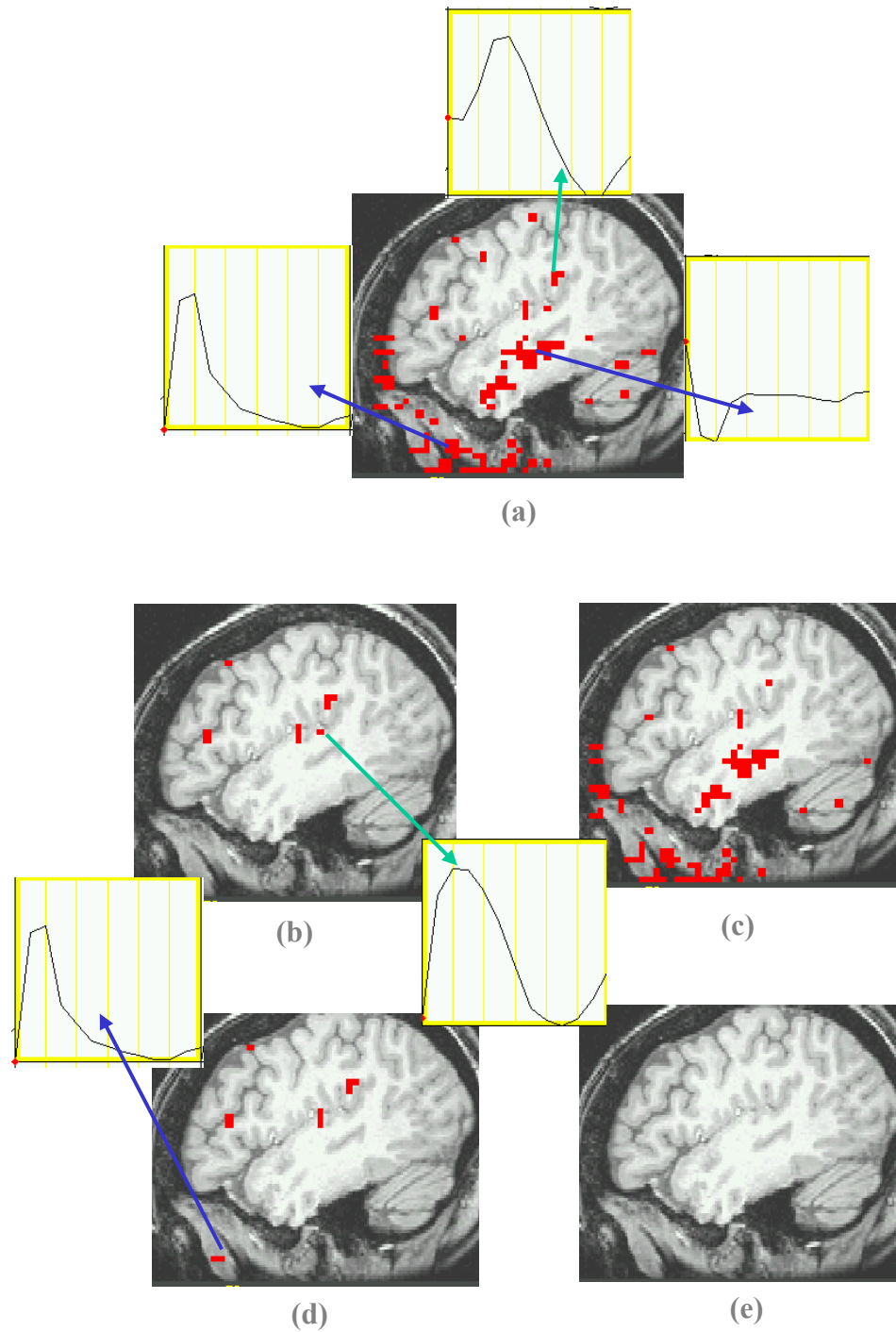


Figure 5.23: Activation maps thresholded at $R^2 > 0.2$ for control subject 4 with no TCM noise-reduction (a), with selective detrending (b), with motion parameter regression (c), with ignoring 2 images after speech (d) and with non-selective detrending (e). The blue arrows indicate TCM voxel IRFs and the green arrows BOLD voxel IRFs.

Figure 5.24 (a) shows some representative extra-cerebral TCM IRFs extracted from the control subject 4 dataset. There are a lot of similarities in the TCM responses. Some of the TCM IRFs are shifted relative to the time of onset and some have significant longer lasting effects.

Figure 5.24 (b) shows the effect of applying the reviewed methods of TCM noise reduction on a right medial-frontal BOLD activation voxel in control subject 4. This voxels hemodynamic response has an ‘early’ onset. It is obvious from the Figure 5.24 (b) that the method of ignoring two images during speech (ML2, black) suffers from a lack of sensitivity to the early portion of the hemodynamic response, since the method ignores the first two images. The non-selective detrending method (dt, red) removes BOLD MR signal in this voxel and hence is sub-optimal. The selective detrending method (dtsel, magenta) does not perform any detrending on this voxel and leaves the BOLD signal intact. The motion parameter regression method (MPR, green) also seems to leave the BOLD MR signal more or less intact.

The modified ROC analyses for the control subject 4 is illustrated in Figures 5.25 (a-b). The efficiency of TCM noise reduction of all the four methods as well as for the case of no motion correction is shown in Figure 5.25 (a). The non-selective detrending method (dt; red curve) performs the best in terms of reducing TCM false-positives. The selective detrending method (dtsel; magenta) performs better than the method of ignoring images (ML2; black) as well as the motion-parameter regression method (MPR; green). The curves for the ML2 and the MPR methods look similar (though the ML2 method seems to perform slightly better). The no-correction curve (ML0; blue) is also given for reference.

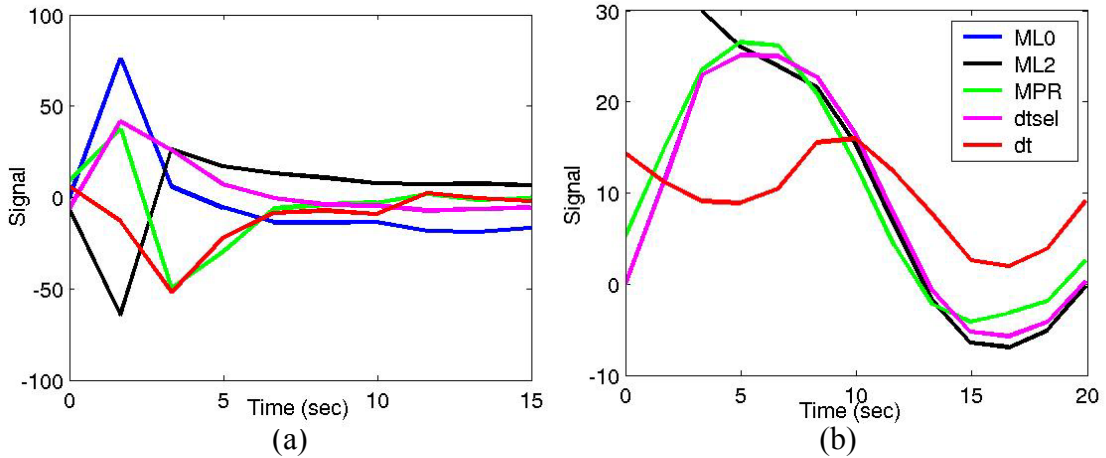


Figure 5.24: Some representative TCM-related voxel IRFs from control subject 4 (a). The effect of the methods of noise correction on a right medial-frontal voxel BOLD HRF exhibiting an ‘early’ response for the same dataset. The no-correction curve is hidden by the selective detrending curve.

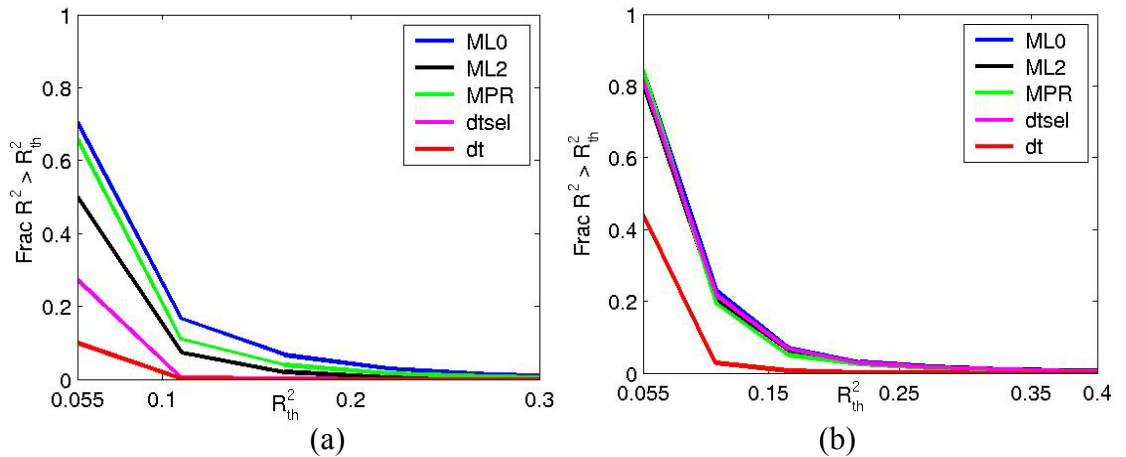


Figure 5.25: Fraction of voxels detected as a function threshold R^2 for (a) the false-positives test-bed and (b) the true-positives test-bed for control subject 4. The blue curve (ML0) represents the case of no motion correction, the black curve (ML2) represents the method of ignoring first 2 images after speech, the green curve (MPR) represents the motion-parameter regression method, the magenta curve (dtssel) represents the selective detrending method and the red curve (dt) represents the non-selective detrending method.

Figure 5.25 (b) shows the effect of each of the TCM noise reduction treatments on the test-bed of the true-positive BOLD HRF-like voxels. The distributions look similar except for the non-selective detrending method. The non-selective detrending method seems to suffer from a loss of sensitivity to BOLD MR signal. By considering this graph along with the TCM noise reduction graph of Figure 5.25 (a) one can state that the selective detrending method performs the best in terms of TCM noise reduction and true positive BOLD HRF retention.

Discussion

From the results shown, the superiority of the selective detrending method is apparent over the other three methods of TCM noise reduction: 1) the motion-parameter regression method (MPR), 2) the method of ignoring 2 images during speech (ML2) and 3) the non-selective detrending method. It would be remunerative to examine the source of this superiority.

The effect of the MPR method (117-118) on the datasets is interesting. Table 1 expresses the average maximum rigid rotation and translation of the head during epochs of speech production. These values have been obtained by considering the first four images after every overt response, finding the absolute maximum of each of the 6 motion parameters during those four images and constructing a mean of all the epochal maxima. Thus, the values in the table refer to the rigid-body TCM during speech. It should be noted that the maximum rotation consistently through all the epochs is less than a third of a degree for the most motion-prone dataset (patient 2 pre-therapy scan), corresponding to less than 3 Hz disturbance in background magnetic field, and leading to less than a sixth of a pixel shift consistently through all the epochs. The maximal TCM rigid-rotation in other datasets is much less. Contrast to that the jaw movement TCM related changes in

background field can be up to 10 Hz. Thus for the datasets examined, the rigid movement of the head is probably not a major contributing factor in the TCM related signal changes. Examining the modified MPR ROC curves of all the subjects reveals that, the cases in which the MPR method leads to attenuation TCM false-positives (e.g. control subject 3) also reflect loss of sensitivity to true-positives. This illustrates the ‘throwing the baby with the bath water’ effect of the MPR method which has been observed in the literature (117-118).

Subject	roll (deg)	pitch (deg)	yaw (deg)	dS (mm)	dL (mm)	dP (mm)
Pat 1 pre-tx	0.0617	0.0777	0.0856	0.1462	0.0795	0.0633
Pat 1 post-tx	0.1136	0.1448	0.1466	0.2820	0.0968	0.0992
Pat 2 pre-tx	0.0880	0.1581	0.2486	0.4188	0.1783	0.0576
Pat 2 post-tx	0.0972	0.1472	0.2914	0.2674	0.1557	0.0804
Control 1	0.0666	0.1910	0.0683	0.1310	0.0609	0.0663
Control 2	0.0523	0.1619	0.1281	0.2005	0.0680	0.0555
Control 3	0.0506	0.1763	0.1467	0.2312	0.1066	0.1053
Control 4	0.0346	0.0915	0.0812	0.1151	0.0704	0.0588

Table 1: The mean of the epochal maxima of the 3 rigid rotational motion parameters, roll, pitch and yaw (degrees) and of the 3 rigid translational motion parameters, displacements towards the superior direction, to the left and towards the posterior (mm). Each epoch represents the motion during the first 4 images after each overt response.

The method of ignoring first two images during and after speech (ML2) has been put forward as a potential means to reduce TCM false-positives (127). This method assumes that all the TCM signal changes occur in the first 2 images after speech. Also it works when the BOLD hemodynamic signal changes are temporally resolvable from the TCM signal changes. All the datasets exhibit some TCM responses which are shifted (i.e. start after the first couple of images) as well as some longer lasting ones. The basis of the delay to onset of the TCM IRF could lie in the constraints of whole-brain image

acquisition. In multi-slice whole-brain studies, the latter acquired slices are temporally shifted with respect to the slices imaged first. Thus, the IRFs of voxels in the latter slices will be shifted in time with respect to the voxels in the first acquired slices. The longer lasting TCM responses could be due to slow magnetic field changes, like during swallowing (125) or due to relaxation to steady state effects. The ML2 method will not be able to sufficiently attenuate such shifted and longer lasting TCM signal changes. The dataset from patient 1 (post-therapy scan) seems especially corrupted by shifted and longer lasting TCM signal changes. The ML2 method does not perform well in such conditions. The selective detrending method outperforms the ML2 method in terms of TCM false-positives reduction in all cases studied. The ML2 method may also suffer from loss of sensitivity to true-positive BOLD signal changes which do not exhibit a delay to onset or start prior to word-enunciation. The results section illustrates examples of such voxels for all the eight datasets.

The non-selective detrending method (125) assumes that the TCM signal changes are temporally resolvable from the BOLD signal changes. Application of this method involves detrending all the voxels in the fMRI dataset of components proportional to the chosen TCM time-series. From the results section, it is apparent that there is a good deal of similarities between the TCM time-series (within a dataset and even between datasets). In addition since the non-selective detrending method detrends components proportional to all the TCM time-series from a given voxel (which is effectively the same as detrending components proportional to the modulus sum of all the chosen TCM time-series) a handful would suffice for an adequate representation. The selective detrending method on the other hand only detrends components proportional to the maximally

correlated TCM time-series (given the detrending criteria are satisfied) from a given voxel. Thus it requires more representative TCM time-series to adequately characterize the effects of TCM.

The magnetic field disturbances due speech-related TCM are more pronounced at the inferior and frontal regions of the brain (124). The field disturbances rapidly fall off in the inferior-to-superior and anterior-to-posterior direction. Thus, the effects of TCM are not uniform throughout the brain. The activation maps of the no-correction cases in the datasets examined illustrate this point. There is more false-positive extra-cerebral TCM voxels in the frontal and inferior regions of the head. Thus, the non-selective detrending of all the voxels in the dataset of components proportional to all the TCM time-series may be superfluous. More importantly, if there is an overlap between the BOLD hemodynamic response of a given voxel and the TCM IRF being detrended from the voxel, the non-selective detrending method reduces true-positive BOLD MR signal. Such a case arises in situations analogous to the ones mentioned in the discussion of the ML2 method. The results section illustrates examples of voxels in which the non-selective detrending method results in substantial attenuation of true-positive BOLD MR signal for all the eight datasets. Thus, though the non-selective detrending method performs the best in terms of reduction of TCM false-positives in all the datasets examined, it is also the least optimal in terms of true-positives retention. The selective detrending method performs as well as (or comparable to) the non-selective method in terms of false-positives reduction.

The results also indicate that the three TCM noise reduction methods: ignoring images (ML2), non-selective detrending and selective detrending would benefit from

increased temporal resolution. The ML2 method would benefit from the greater flexibility afforded in choosing the number of images screened with increased temporal resolution. The selective detrending method would benefit from the increased number of images available in the fitting/detrending procedure allowing for a more robust fit. The process of selecting which voxels to detrend will also benefit from increased temporal resolution. The attendant additional images available will make the cross-correlation as well as the χ^2 -norm estimates more robust. In this context, it must be mentioned that values for $resnorm_{TCM}$ and $resnorm_{BOLD}$ chosen for the selective detrending method should be viewed more as a prescription than a rule. The values used in this thesis were arrived at by examining what was optimal for the first two datasets. These chosen values of $resnorm_{TCM}$ and $resnorm_{BOLD}$ were found to perform adequately in the subsequent six datasets studied. These values may not have general application and it would be remunerative to find the optimal limits for each dataset studied on an individual basis.

The argument regarding the scope for improvement of the fitting/detrending procedure with increased temporal resolution, mentioned above, is also applicable for the non-selective detrending procedure. The influence on temporal resolution on the motion parameter regression method is less certain. Regression estimates' robustness scale with the number of data-points available. However, our results indicate that there does not seem to be a direct benefit in using the MPR method in TCM noise reduction in the first place.

Motion in FMRI is idiosyncratic in nature. It can affect different subjects differently. Even the same subject scanned under different conditions can be affected differently by motion. From Table 1 it may be noticed that the average epochal maxima

of the rigid-motion parameters in the post-treatment scan for aphasia patient-1 is almost double that of the pre-scan. The effects of TCM are also different between pre- and post-therapy scans for patient 1. The post-therapy scan seems less responsive to the ML2 method of TCM noise-reduction, indicating more shifted and longer lasting TCM signal changes in the post-therapy scan.

Finally it would be remunerative to examine the similarities and the differences between the aphasia patients and normal control subjects with regards to task-correlated motion. It can be noted from examining Table 1 that, in general the control subjects exhibited less task-correlated rigid-body motion when compared to the patient datasets. This is understandable as the controls are more motivated and also understand and follow the instructions better. The ischemic stroke which causes broca's aphasia in the patients also may lead to impairment of motor function. The patients thus have less control over their movements and speech. The results show a little more TCM corrupted voxels in patients compared to controls. The TCM responses, in general, look similar across different subjects, indicating that the TCM signal changes have a similar physical origin.

CHAPTER 6 CONCLUSION AND FUTURE WORK

In this chapter the conclusions reached after analysis of the data presented in the previous chapter are discussed. Improvements on the method and future directions of TCM noise-reduction research are conjectured.

Conclusion

Event-related overt word generation paradigms play an important role in the understanding of brain function (127, 130). The necessity for monitoring the subject responses in fMRI of patients (130) requires use of overt word generation paradigms. Task-correlated motion acts as a major confound in the analysis of overt word-generation paradigms (125). TCM artifacts in event-related overt word generation paradigms have been treated with three main methods: motion parameter regression (117), ignoring/screening signal changes during speech (127, 128) and detrending fMRI datasets of components proportional to the TCM time-series chosen from false-positive TCM voxels (125). In Chapter 4, a new selective detrending method was introduced.

The results from the Chapter 5 indicate that the selective detrending method performs better than the other three main methods of TCM noise reduction in vogue. The selective detrending method performs almost as well as the non-selective detrending method in terms of TCM noise reduction and better than all other methods in terms of capacity to retain BOLD MR signals. Moreover, the results of the previous chapter point out the inadequacies of using the motion parameter regression method (MPR), the

ignoring images during speech method (ML2) and the non-selective detrending method in whole-brain event-related overt word generation paradigms.

The MPR method assumes a linear relationship between the rigid motion parameters and related fMRI signal changes and tries to eliminate motion-related signal changes by regressing out components of the fMRI time-series proportional the motion parameter time-series. Depending upon the regression fit between the motion parameter time-series and the fMRI time-series, this method may either have little effect on TCM noise reduction or might have a deleterious effect on BOLD MR signal along with TCM noise.

The method of ignoring the first two images (ML12) after speech assumes that the TCM signal changes are temporally resolvable from BOLD MR signal changes. The ML2 method fails to attenuate TCM signals which are shifted relative to the overt response stimulus. This can be a significant issue in whole-brain fMRI, where the slices acquired last are delayed by about an image TR off with respect to the stimulus vector. The ML2 method also suffers from a loss of sensitivity to ‘early’ hemodynamic responses that either start before the overt-response stimulus or exhibit minimal delay to onset.

The non-selective detrending method makes the same assumption regarding temporal resolvability of BOLD and TCM signal changes as the ML2 method. Since this method effectively detrends the components of all the voxel time-series in the fMRI dataset proportional to the sum of the selected TCM time-series, the penalty of temporally unresolved BOLD and TCM signal changes is the loss of sensitivity to true-positive brain activation. The selective detrending method is to some extent able to

overcome these and other confounds by examining for TCM related signal changes and detrending accordingly. The success of the selective detrending method is critically dependent on the proper and adequate characterization of the TCM and BOLD signal changes in the dataset. This can be accomplished with a good deal of certainty for voxels activated above the threshold selected for inferring brain activation through visual inspection. In fact the efficacy of all the methods used can be determined for voxels activated above the selected threshold by visual inspection. Although, in theory data driven/modeled methods of inspection are more objective, in fact proper modeling of the TCM and BOLD responses can be difficult and sensitive to modeling error. Visual inspection can however be time consuming. It is also subjective (though not entirely so in that TCM and BOLD patterns can oftentimes be more easily told apart by visual inspection than data modeling). All the phenomenological methods of TCM noise reduction suffer to an extent from subjective inferences and interpretation of data. This situation is unappealing to the Physicist's mind which is always looking for elegant solutions.

One other conclusion that can be generalized to all overt word-generation studies is the finding that magnetic field disturbances that produce signal fluctuations during speech seem to act as the main source of TCM signal changes. This is borne out by Table 1 in Chapter 5 which suggests that with proper padding rigid-rotation can be restricted to less than a third of a degree leading to less than a sixth of pixel-shifts. Speech-related field disturbances are an order of magnitude higher. Since the field disturbances are known to propagate from inferior to superior regions of the brain (124, 125) use of sagittal or coronal acquisitions will by and large keep the field shifts in-plane and the

resulting artifacts can be attenuated by distortion correction methods (113). Use of axial slices will result in the added confound of non-uniform slice excitation from image to image as well as through-plane dephasing, neither of which is easily treatable.

Future Work

The selective detrending method introduced in this study works in a univariate general linear model framework. Whenever detrending is executed it essentially removes a fixed amount of TCM signal at each epoch (formed by overt response and located in time by the stimulus vector). Thus since the overall GLM statistic, whether it be F -statistic or the coefficient of determination, R^2 , relies on the convolution (with the stimulus vector) of the estimated IRF, which can be considered as an average across the epochs, the detrended time-series results in a TCM denoised estimate of the test-statistic. To perform a more thorough TCM detrending one could examine for the presence of TCM related signal changes at each epoch and detrend selectively in a time-dependent manner. Such a detrended time-series would be amenable to more probing forms of analysis like randomization tests and paradigm independent methods. The time and hardware penalty in conducting this detrending scales linearly as the number of epochs. Thus for the present study which had up to 45 epochs, this proposed detrending of each individual stimulus presentation could take 45 times longer (which comes out to about one day per dataset) than the current implementation.

A different approach to TCM noise reduction would be to utilize the correlated changes in voxel phase during speech. Essentially, background magnetic field disturbances during speech will leave a signature in the image-phase of the voxels. Changes in voxel phase can be utilized to undistort the attendant pixel shifts (113) in a time-dependent fashion. Real-time auto-shimming methods which do first-order linear

distortion correction already exist (116). Alternately phase-correlated magnitude signal changes can be regressed out of the FMRI time-series (38). One major difficulty in distortion correction using voxel phase is that the unwarp is a first order correction and the magnitude TCM related field disturbances will probably lead to non-linear distortions in the image. This confound will also affect the voxel-phase regression method as the relation between phase changes and the resultant signal changes maybe nonlinear. However these difficulties may not be insurmountable and there is hope that more elegant solutions to TCM related noise in FMRI time-series will be found.

APPENDIX
SELECTED PUBLICATIONS

In this appendix a few selected publications of Kaundinya S. Gopinath are listed.

Conference Abstracts

ISMRM Proceedings: Oral Sessions

K.S. Gopinath, K.K. Peck, D.A. Soltysik, B.A. Crosson, and R.W. Briggs, "A Selective Detrending Method to Reduce Noise Due to Event-Related Motion in fMRI Time-Series for an Event-Related Overt Word Generation Paradigm," Proc. Intl. Soc. Mag. Res. Med. 11, 388(2003). 11th ISMRM (International Society for Magnetic Resonance in Medicine) meeting, Toronto, Ontario, Canada, May 10-16, 2003.

K.S. Gopinath and R.W. Briggs, "Fourier Method for Detection of FMRI Signal in Noise of Unknown Power Spectral Density," Proc. Intl. Soc. Mag. Res. Med. 10, Vol. 1, abstract 750 (2002). 10th ISMRM (International Society for Magnetic Resonance in Medicine) meeting, Honolulu, Hawaii, May 18-24, 2002.

Kaundinya Gopinath, Richard W. Briggs, David Soltysik, Nathan Himes, and Bruce A. Crosson, "Reduction of Noise Associated With Stimulus Correlated Motion in Event Related Overt Word Production fMRI Studies," Proc. Intl. Soc. Mag. Res. Med. 9, 297 (2001). 9th ISMRM (International Society for Magnetic Resonance in Medicine) meeting, Glasgow, Scotland, April 21 27, 2001.

Nathan C. Himes, Richard W. Briggs, Kaundinya S. Gopinath, Michael E. Robinson, Donald D. Price, and G. Nicholas Verne, "fMRI Studies of Visceral and Cutaneous Pain in IBS Patients and Normal Subjects," Proc. Intl. Soc. Mag. Res. Med. 9, 530 (2001). 9th ISMRM (International Society for Magnetic Resonance in Medicine) meeting, Glasgow, Scotland, April 21 27, 2001.

ISMRM Proceedings: Poster Sessions

K.S. Gopinath, K.K. Peck, D.A. Soltysik, and R.W. Briggs, "Similarities in the Low Frequency Noise Characteristics between the Magnitude and Phase Time-Series," Proc. Intl. Soc. Mag. Res. Med. 11, 1890 (2003). 11th ISMRM (International Society for Magnetic Resonance in Medicine) meeting, Toronto, Ontario, Canada, May 10-16, 2003.

K.S. Gopinath, K.K. Peck, D.A. Soltysik, B.A. Crosson, and R.W. Briggs, "Comparison of the Low Frequency Noise Characteristics between Diseased and Healthy Brain Regions," Proc. Intl. Soc. Mag. Res. Med. 11, 1892 (2003). 11th ISMRM (International Society for Magnetic Resonance in Medicine) meeting, Toronto, Ontario, Canada, May 10-16, 2003.

D.A. Soltysik, K. Gopinath, K.K. Peck, B.A. Crosson, and R.W. Briggs, "A Quantitative Analysis of the Nonlinearity of the BOLD Response in Different Cortices," Proc. Intl. Soc. Mag. Res. Med. 11, 1887 (2003). 11th ISMRM (International Society for Magnetic Resonance in Medicine) meeting, Toronto, Ontario, Canada, May 10-16, 2003.

K. Peck, A. Bacon Moore, B. Crosson, K. Gopinath, D. Soltysik, and R.W. Briggs, "Reduction in Time to Peak of Hemodynamic Response Functions After Therapy Demonstrated by BOLD fMRI Studies of Aphasia Patients," Proc. Intl. Soc. Mag. Res. Med. 11, 2025 (2003). 11th ISMRM (International Society for Magnetic Resonance in Medicine) meeting, Toronto, Ontario, Canada, May 10-16, 2003.

K.S. Gopinath, K.K. Peck, T.W. Conway, and R.W. Briggs, "Increase in Linearity of the BOLD Response Along a Functionally Connected Neural Pathway," Proc. Intl. Soc. Mag. Res. Med. 10, Vol. 2, abstract 1388 (2002). 10th ISMRM (International Society for Magnetic Resonance in Medicine) meeting, Honolulu, Hawaii, May 18-24, 2002.

Kyung K. Peck, Kaundinya Gopinath, David Soltysik, Anna Moore, Christina Wierenga, Bruce Crosson, and Richard W. Briggs, "Comparison of Functional Time Course Patterns in Broca's Area and Supplementary Motor Area during Silent Sentence Generation Task in fMRI," Proc. Intl. Soc. Mag. Res. Med. 10, Vol. 2, abstract 1491 (2002). 10th ISMRM (International Society for Magnetic Resonance in Medicine) meeting, Honolulu, Hawaii, May 18-24, 2002.

Kaundinya Gopinath, Yunmei Chen, Richard W. Briggs, Feng Huang, and T. Sheshadri, "Feature Based Image Registration for FMR Images," Proc. Intl. Soc. Mag. Res. Med. 9, 1201 (2001). 9th ISMRM (International Society for Magnetic Resonance in Medicine) meeting, Glasgow, Scotland, April 21-27, 2001.

Kaundinya Gopinath, Richard W. Briggs, and Nathan Himes, "Examination of the Linearity of BOLD FMRI Responses in a Higher Level Cognitive System," Proc. Intl. Soc. Mag. Res. Med. 9, 1189 (2001). 9th ISMRM (International Society for Magnetic Resonance in Medicine) meeting, Glasgow, Scotland, April 21-27, 2001.

Richard W. Briggs, Iona Dy-Liacco, Kaundinya S. Gopinath, Nathan C. Himes, David A. Soltysik, Paul Browne, and Roger Tran-Son-Tay, "A New Vibrotactile Device for fMRI," *Proc. Intl. Soc. Mag. Res. Med.* 9, 1227 (2001). 9th ISMRM (International Society for Magnetic Resonance in Medicine) meeting, Glasgow, Scotland, April 21-27, 2001.

J.M. Anderson, R.W. Briggs, B. Crosson, K.S. Gopinath, D. Gokcay, J.R. Sadek, L.J. Gonzalez Rothi, E.J. Auerbach, D.A. Soltysik and K.M. Heilman, "Evidence of Right Hemisphere Engagement during the Production of Overt Emotional Prosody: An Event Related fMRI Study," Abstract 899, 8th ISMRM (International Society for Magnetic Resonance in Medicine) meeting, Denver, Colorado, April 1-7, 2000.

R.W. Briggs, J.M. Anderson, B. Crosson, L.M. Maher, H.L. Roth, K.S. Gopinath, D. Gokcay, L.J. Gonzalez Rothi, E.J. Auerbach, and D.A. Soltysik, "Preliminary Evidence of Language Reorganization After Left Hemispheric Injury: A Whole Brain, Event Related fMRI Study of Sentence Production," Abstract 862, 8th ISMRM (International Society for Magnetic Resonance in Medicine) meeting, Denver, Colorado, April 1-7, 2000.

R.W. Briggs, K.S. Gopinath, M.A. Cato, and B.A. Crosson, "Deconvolution Analysis in Emotional Word Generation Monitored by Random Block and Event Related fMRI," Abstract 836, 8th ISMRM (International Society for Magnetic Resonance in Medicine) meeting, Denver, Colorado, April 1-7, 2000.

Full Papers

M.A. Cato, B. Crosson, D. Gokcay, D. Soltysik, C. Wierenga, K. Gopinath, N. Himes, H. Belanger, R.M. Bauer, I.S. Fischler, L. Gonzalez-Rothi, and R.W. Briggs, *J. Cog. Neuroscience* (accepted for publication). "Processing Emotional Connotation during Word Generation: Laterality and Effects on Rostral Frontal and Retrosplenial Cortices."

G. N. Verne, N.C. Himes, M.E. Robinson, K.S. Gopinath, R.W. Briggs, B.A. Crosson, and D.D. Price, *Pain* (in press). "Central Representation of Visceral and Cutaneous Hypersensitivity in the Irritable Bowel Syndrome."

B. Crosson, H. Benefield, M.A. Cato, J.R. Sadek, A.B. Moore, C.E. Wierenga, K. Gopinath, D. Soltysik, R.M. Bauer, E.J. Auerbach, D. Gökçay, C.M. Leonard, and R.W. Briggs, *J. Intl. Neurophysch. Soc.* (in press). "Left and Right Basal Ganglia and Frontal Activity during Word Generation: The Nature of Lexical-Semantic Retrieval."

B. Crosson, M.A. Cato, J.R. Sadek, D. Gokcay, R.M. Bauer, I.S. Fischler, L. Maron, K.S. Gopinath, E.J. Auerbach, S.R. Browd, and R.W. Briggs, *J. Intl. Neurophysch. Soc.*, 8,

607-622 (2002). "Semantic Monitoring of Words with Emotional Connotation during fMRI: Contribution of Anterior Left Frontal Cortex."

Y. Chen, H.D. Tagare, S. Thiruvankadam, F. Huang, D. Wilson, K.S. Gopinath, R.W. Briggs, and E.A. Geiser, *Intl. J. Computer Vision*, 50(3), 315-328 (2002). "Using Prior Shapes in Geometric Active Contours in a Variational Framework."

J.M. Gelb, K.S. Gopinath, D.C. Kennedy, *International Journal of Modern Physics D*, 8(2), 229-250 (1999). "Relativistic electrons on a rotating spherical magnetic dipole: surface orbitals."

J.M. Gelb, K.S. Gopinath, D.C. Kennedy, *International Journal of Modern Physics D*, 8(2), 251-270 (1999). "Relativistic electrons on a rotating spherical magnetic dipole: localized three-dimensional states."

K.S. Gopinath, D.C. Kennedy, Technical Report, UFIFT-HEP-97-06 (1997). "Relativistic charged particle in magnetic dipole-spherical geometry : II. general tiled surface orbits."

K.S. Gopinath, D.C. Kennedy, J.M. Gelb, Technical Report, UFIFT-HEP-97-11 (1997). "Relativistic charged particle in magnetic dipole-spherical geometry :III. Local three-dimensional states."

K.S. Gopinath, Thesis (M.S.)--University of Florida, (1997), "Relativistic charged particle in dipole-sphere configuration."

K.S. Gopinath, Thesis (M.Sc)—University of Poona (1993), "Large-Scale Structures in the Universe."

Y. Chen, S. Thiruvankadam, F. Huang, K.S. Gopinath, and R.W. Briggs, in preparation for submission to *IEEE Trans. Med. Imaging*. "Feature Based Image Registration for Functional MR Images."

R.W. Briggs, I. Dy-Liacco, M.P. Malcolm, H. Lee, K.K. Peck, K.S. Gopinath, N.C. Himes, D.A. Soltysik, P. Browne, and R. Tran-Son-Tay, *Magn. Reson. Med.* (under revision) "A Pneumatic Vibrotactile Stimulation Device for fMRI."

K.S. Gopinath, Thesis (Ph.D) University of Florida (expected August 2003). "Reduction of Noise Associated with Stimulus-Related Motion in fMRI time-series."

K.S. Gopinath, K.K. Peck, D.A. Soltysik, B.A. Crosson, and R.W. Briggs, in preparation, "A Selective Detrending Method to Reduce Noise Due to Event-Related Motion in fMRI Time-Series for an Event-Related Overt Word Generation Paradigm."

K.S. Gopinath, K.K. Peck, D.A. Soltysik, K. D. White, B.A. Crosson, and R.W. Briggs, in preparation, "Sensitivity Compensation Analysis for Comparison of Pre- and Post-treatment Scans of Aphasia Patients Under a Language fMRI Paradigm."

LIST OF REFERENCES

1. Stern O, Gerlach W. Ueber die Richtungsquantelung im Magnetfeld. *Ann Phys* 1924;74: 673-678.
2. Rabi II, Zacharias JR, Millman S, Kusch P. A new method of measuring nuclear magnetic moments. *Phys Rev* 1938;53: 318-327.
3. Bloch F. Nuclear induction. *Phys Rev* 1946;70: 460-466.
4. Purcell EM, Torrey HC, Pound RV. Resonance absorption by nuclear magnetic moments in a solid. *Phys Rev* 1946;69: 37-45.
5. Mansfield P, Grannell PK. NMR “diffraction” in solids? *J Phys C: Solid State Phys* 1973; 6: L422-L426.
6. Lauterbur PC. Image formation by induced local interactions: Examples employing NMR. *Nature* 1973;243:190-191.
7. Sakurai A. *Modern quantum mechanics*. Reading: Addison-Wesley; 1994.
8. Rabi II, Ramsey NF, Schwinger J. Rotating co-ordinates in magnetic resonance problems. *Rev Modern Phys* 1954;26:167-189.
9. Abragam A. *The principles of nuclear magnetism*. New York:Clarendon; 1961.
10. Haacke EM, Brown RW, Venkatesan R. *Magnetic resonance imaging: Physical principles and sequence design*. New York: Wiley; 1999.
11. Wehrli FW. Principles of Magnetic Resonance. In: Stark DD, Bradley WG (eds) pp 44-70. *Magnetic resonance imaging*. St. Louis. C.V.Mosby Co; 1988.
12. Oxridge RJ, Coxon R, Howseman A, Chapman B, Turber R, Stehling M, Mansfield P. Snapshot head imaging at 0.5 T using echo planar imaging technique. *Magn Reson Med* 1988;8:110-115.
13. Mansfield P. Multi-planar image formation using NMR spin-echoes. *J Phys C* 1977;10:L55-L58.
14. Ahn CB, Kim JH, Cho ZH. High speed spiral echo-planar NMR imaging. *IEEE Trans Med Imag* 1986;MI-5:2.

15. Macovski A, Meyer CH. A novel fast-scanning system. *Proc Soc Magn Reson Med* 1986;5:156
16. Stehling MK, Turner R, Mansfield P. Echo-planar imaging: Magnetic resonance imaging in a fraction of a second. *Science* 1991;245:43-50.
17. Meyer CH, Macovski A, Nishimura DG. Fast spiral coronary artery imaging. *Magn Reson Med* 1992;28:202-213
18. Noll DC, Cohen JD, Meyer CH, Schneider W. Spiral k-space MR imaging of cortical activation. *J Magn Reson Imag* 1995;5:49-56.
19. Noll DC, Stenger VA, Vazquez AL, Peltier S. Spiral scanning in fMRI. In: Moonen CTW, Bandettini PA (eds) pp 149-160. *Functional MRI*. Springer. 1998.
20. Villringer A. Contrast agent perfusion in rat brain. *Proc Soc Magn Reson Med* 1982;1:32
21. Belliveau JW, Kennedy DN, McKinstry RC, Buchbinder BR, Weiskoff RM, Cohen MS, Vevea JM, Brady TJ, Rosen BR. Functional mapping of human visual cortex by magnetic resonance imaging. *Science* 1991;254:716-719.
22. Ogawa S, Lee TM, Nayak AS, Glynn P. Oxygenation sensitive contrast in magnetic resonance image of rodent brain at high magnetic fields. *Magn Reson Med* 1990;14:68-78.
23. Pauling L, Coryell CD. Magnetic properties and structure of hemoglobin, oxyhemoglobin and carbon monoxy hemoglobin. *Proc Natl Acad Sci USA* 1936;22:210-216.
24. Kwong KK, Belliveau JW, Chesler DA, Goldberg IE, Weiskoff RM, Poncelet BP, Kennedy DN, Hoppel BE, Cohen MS, Turner R. Dynamic magnetic resonance imaging of human brain activity during primary sensory stimulation. *Proc Natl Acad Sci USA* 1992;89:5675-5679.
25. Ogawa S, Tank DW, Menon R, Ellerman JM, Kim SG, Merkle H, Ugurbil K. Intrinsic signal changes accompanying sensory stimulation: functional brain mapping with magnetic resonance imaging. *Proc Natl Acad Sci USA* 1992;89:5951-5955.
26. Williams DS, Detre JA, Leigh JS, Koretsky AP. Magnetic resonance imaging of perfusion using spin inversion of artificial water. *Proc Natl Acad Sci USA* 1992;89:212-216.
27. Raichle ME. Circulatory and metabolic correlates of brain function in normal humans. In: Mountcastle VB, Plum F, Geiger SR (eds) pp 103-118. *Handbook of physiology-the nervous system*. American Physiological Society. Bethesda. 1987.

28. Malonek D, Grinvald A. Interactions between electrical activity and cortical micro-circulation revealed by imaging spectroscopy-implications for functional brain mapping. *Science* 1996;272:551-554.
29. Chen W, Ogawa S. Principles of BOLD functional MRI. In: Moonen CTW, Bandettini PA (eds) pp 103-114. *Functional MRI*. Springer. 1998.
30. Hogue RD, Pike GB. Quantitative measurement using fMRI. In: Jezzard P, Matthews PM, Smith SM (eds) pp 159-174. *Functional MRI: An introduction to methods*. Oxford University Press. Oxford. 2001.
31. Hu X, Yacoub E, Le TH, Cohen ER, Ugurbil K. Functional MRI signal decrease at the onset of stimulation. In: Moonen CTW, Bandettini PA (eds) pp 243-252. *Functional MRI*. Springer. 1998.
32. Cohen MS. Parametric analysis of fMRI data using linear system methods. *Neuroimage* 1997;6:93-103.
33. Mandeville JB, Marota JJA, Ayata C, Moskowitz MA, Weiskoff RM. MRI measurement of the temporal evolution of relative CMRO₂ during rat forepaw stimulation. *Magn Reson Med* 1999;42:944-951.
34. Buxton RB, Wong EC, Frank LR. Dynamics of blood flow and oxygenation changes during brain activation: the balloon model. *Magn Reson Med* 1998;39:855-864.
35. Kim SG, Hendrich K, Hu X, Merkle H, Ugurbil K. Potential pitfalls of functional MRI using conventional gradient recalled echo techniques. *NMR Biomed* 1994;7:69-74.
36. Lai S, Hopkins AL, Haacke EM, Li D, Wasserman BA, Buckley P, Friedman L, Meltzer H, Hedera P, Friedland R. Identification of vascular structures as a major source of signal contrast in high resolution 2D and 3D functional activation imaging of the motor cortex at 1.5 T: preliminary results. *Magn Reson Med* 1993;30:387-392.
37. Duong TQ, Kim DS, Ugurbil K, Kim SG. Spatiotemporal dynamics of BOLD fMRI signals: towards mapping sub-millimeter cortical columns using early negative response. *Magn Reson Med* 2000;44:231-242.
38. Menon RS. Postacquisition suppression of large-vessel BOLD signals in high-resolution fMRI. *Magn Reson Med* 2002;47:1-9.
39. Lin W, Mukherjee P, An H, Yu Y, Wang Y, Wo K, Lee B, Kido D, Haacke EM. Improving high-resolution MR BOLD venographic imaging using a T1 reducing contrast agent. *J Magn Reson Imag* 1999;10:110-123.

40. Posner MI. Chronometric explorations of mind. Oxford University Press, New York. 1978.
41. Ogawa S, Lee TM, Stepnowski R, Chen W, Zhu XH, Ugurbil K. Proc Natl Acad Sci USA 2000;11026-11031.
42. Dale AM, Liu AK, Fischl B, Lewine JD, Buckner RL, Belliveau, JW, Halgren E. Dynamic statistical parametric mapping: combining fMRI and MEG to produce high resolution imaging of cortical activity. Neuron 2000;26:55-67.
43. Bandettini PA, Jesmanowicz, A, Wong EC, Hyde JS. Processing strategies for time-course datasets in functional MRI of human brain. Magn Reson Med 1993;30-161-173.
44. Friston KJ, Jezzard P, Turner P. Analysis of functional MRI time-series. Human Brain Mapping 1994;1:153-171.
45. Boynton GM, Engel SA, Glover GH, Heeger DJ. Linear systems analysis of functional magnetic resonance imaging in human V1. J Neurosci 1996;16:4207-4221.
46. Vazquez AL, Noll DC. Nonlinear aspects of the BOLD response in functional MRI. Neuroimage 1998;7:108-118.
47. Miezin FM, Maccotta L, Ollinger JM, Peteresen SE, Buckner RL. Characterizing the hemodynamic response: effects presentation rate, sampling procedure and the possibility of ordering brain activity based on relative timing. Neuroimage 2000;11:735-759.
48. Friston KJ, Josephs O, Rees G, Turner R. Nonlinear event-related responses in fMRI. Magn Reson Med 1998;39:41-52.
49. Huettel SA, McCarthy G. Evidence of a refractory period in the hemodynamic response to visual stimuli as measured by MRI. Neuroimage 2000;11:547-553.
50. Gopinath KS, Briggs RW, Himes N. Examination of the linearity of BOLD FMRI responses in a higher level cognitive system. Proc Intl Soc Magn Reson Med 2001;9:1189.
51. Gopinath KS, Peck KK, Conway TW, Briggs RW. Increase in linearity of the BOLD response along a functionally connected neural pathway. Proc Intl Soc Magn Reson Med 2002;10:1388.
52. Rees G, Friston KJ, Koch C. A direct quantitative relationship between functional properties of human and macaque V5. Nature Neurosci 2000;3:716-723.
53. Logothetis NK, Pauls J, Augath M, Trinath T, Oeltermann A. Neurophysiological investigation of the basis of the fMRI signal. Nature 2001;412:150-157.

54. Lauritzen M. Relationship of spikes, synaptic activity and local changes of cerebral blood flow. *J Cereb Blood Flow Metab* 2001;21:1367-1383.
55. Attwell D, Iadecola C. The neural basis of functional brain imaging signals. *Trends Neurosci* 2002;25:621-625.
56. Moncrief, D., Briggs, RW, Gopinath, K, Schmalfuss I, Peacock, J, Byrd D, Conway T, Musiek F. fMRI activation differences in children with dichotic words. *Proc OHBM* 2003;9:479.
57. Hallet M, Sadato N, Honda M, Nishi K, Waldvogel D, Bushara K. Functional MRI of sensorimotor system. In: Moonen CTW, Bandettini PA (eds) pp 381-392. *Functional MRI*. Springer. 1998.
58. Cox RW, Savoy RL. Functional magnetic resonance imaging (fMRI) “brain reading”: detecting and classifying distributed patterns of fMRI activity in human visual cortex. *Neuroimage* 2003;19:261-270.
59. Crosson B, Benefield H, Cato MA, Sadek JR, Moore AB, Wierenga CE, Gopinath K, Soltysik D, Bauer RM, Auerbach EJ, Gökçay D, Leonard CM, Briggs RW. Left and right basal ganglia and frontal activity during word generation: The nature of lexical-semantic retrieval. *J Intl Neurophysch Soc* (in press).
60. Verne GN, Himes NC, Robinson ME, Gopinath Briggs RW, Crosson BA, Price DD. Central representation of visceral and cutaneous hypersensitivity in the irritable bowel syndrome.
61. Ress D, Heeger DJ. Neuronal correlates of perception in early visual cortex. *Nat Neurosci* 2003;4:414-420.
62. Moore AB, Crosson BA, Gaiefsky M, Wierenga CE, Peck KK, Gopinath K, White K, Soltysik D, Rothi LJG, Briggs RW. Right-hemisphere mobilization by treatment of intention in aphasia: An fMRI study. *Proc J Intl Neurophysch Soc* 2003;9:192.
63. Jack CR, Lee CC, Ward HA, Riederer SJ. The role of functional MRI in planning peritrochlear surgery. In: Moonen CTW, Bandettini PA (eds) pp 539-550. *Functional MRI*. Springer. 1998.
64. Cato MA, Crosson BA, Gokcay D, Soltysik D, Wierenga CE, Gopinath KS, Himes N, Belanger H, Bauer RM, Fischler IS, Gonzalez-Rothi L, Briggs RW. Processing emotional connotation during word generation: Laterality and effects on rostral frontal and retrosplenial cortices. *J Cogn Neurosci* (in press).
65. Engel S, Zhang X, Wandell B. Color tuning in human visual cortex measured with functional magnetic resonance imaging. *Nature* 1997;388:68-71.

66. Aguirre GK, D'Esposito M. Experimental design for brain fMRI. In: Moonen CTW, Bandettini PA (eds) pp 369-380. *Functional MRI*. Springer. 1998.
67. Zarahan E, Aguirre GK, D'Esposito M. Empirical analyses of BOLD fMRI statistics. I. Spatially unsmoothed data collected under null hypothesis conditions. *Neuroimage* 1997;5:179-197.
68. Friston KJ, Zarahan E, Josephs O, Henson RNA, Dale AM. Stochastic designs in event-related fMRI. *Neuroimage* 1999;10:607-619.
69. Liu TT, Frank L, Wong EC, Buxton RB. Detection power, Estimation efficiency, and probability in event-related fMRI. *Neuroimage* 2001;13:759-773.
70. Dale AM, Buckner RL. Selective averaging of individual trials using fMRI. *Hum Brain Mapp* 1997;5:329-340.
71. Dale AM. Optimal experiment design for event-related fMRI. *Hum Brain Mapp* 1999;8:109-114.
72. Hagberg GE, Zito G, Patria F, Sanes JN. Improved detection of event-related functional MRI signals using probability functions. *Neuroimage* 2001;14:1193-1205.
73. McKeown MJ, Makeig S, Brown GG, Jung T, Kindermann S, Bell A, Sejnowski T. Analysis of fMRI data by blind separation into independent spatial components. *Hum Brain Mapp* 1998;6:160-188.
74. Moser E, Diemling N, Baumgartner R. Fuzzy clustering of gradient-echo functional MRI in the human visual cortex. Part I: Quantification. *J Magn Reson Imag* 1997;6:1102-1108.
75. Cox RW, Jesmanowicz A. Real-time image registration for functional MRI. *Magn Reson Med* 1999;42:1014-1018.
76. Friston KJ, Ashburner J, Frith CD, Poline JB, Heather JD, Frackowiak RSJ. Spatial registration and normalization of images. *Hum Brain Mapp* 1995;3:165-189.
77. Woods RP, Grafton ST, Holmes CJ, Cherry SR, Mazziotta JC. Automated image registration: I. General methods and intrasubject, intramodality validation. *J Comput Assist Tomogr* 1998;22:139-152.
78. Eddy WF, Fitzgerald M, Noll DC. Improved image registration using Fourier interpolation. *Magn Reson Med* 1996;36:923-931.
79. Biswal BB, Hyde JS. Contour-based registration technique to differentiate between task-activation and head motion induced signal variations in fMRI. *Magn Reson Med* 1997;38:470-476.

80. Gopinath KS, Briggs RW, Chen Y, Huang F, Thiruvankadam S. Feature based image registration for fMRI. *Proc Intl Soc Mag Reson Med* 2001;9:1201.
81. Chen Y, Tagare HD, Thiruvankadam S, Huang F, Wilson D, Gopinath KS, Briggs RW, Geiser EA. Using prior shapes in geometric active contours in a variational framework. *Int J Computer Vision* 2002;50:315-328.
82. Purdon PL, Weisskoff RM. Effects of temporal autocorrelation due to physiological noise and stimulus paradigm on voxel-level false-positive rates in fMRI. *Hum Brain Mapp* 1998;6:239-249.
83. Fadili MJ, Bullmore ET. Wavelet-generalized least-squares: A new BLU estimator of linear regression models with 1/f errors. *Neuroimage* 2002;15:217-232.
84. Gossel C, Auer DP, Fahrmeir L. Dynamic models in fMRI. *Magn Reson Med* 2000;43:72-81.
85. Cox RW. AFNI: software for analysis and visualization of functional magnetic resonance imaging, *Comput Biomed Res* 1996;29:162-173.
86. Friston KJ, Holmes AP, Worsley KJ, Poline J, Frith CD, Frackowiak RSJ. Statistical parametric maps in functional magnetic resonance imaging: a general linear approach. *Hum Brain Mapp* 1995;2:189-210.
87. LoacisioJJ, Jennings PJ, Moore CI, Corkin S. Time-series analysis in the time domain and resampling methods for studies of functional magnetic resonance brain imaging. *Hum Brain Mapp* 1997;5:168-193.
88. Kay SM. *Modern spectral estimation: Theory and application*. Englewood Cliffs: Prentice Hall; 1988.
89. Marchini JL, Ripley BD. A new statistical approach to detecting significant activation in functional MRI. *Neuroimage* 2000;12:366-380.
90. Gopinath KS, Briggs RW. Fourier method for detection of FMRI signal in noise of unknown power spectral density. *Proc Intl Soc Magn Reson Med* 2002;10:750.
91. Kay S. Adaptive detection for unknown noise power spectral densities. *IEEE Trans Sig Proc* 1999;47:10-21.
92. Noll DC, Schneider W. Theory, simulation and compensation of physiological motion artifacts in functional MRI. *IEEE Int Conf Image Proc* 1994;3:40-44.
93. Hu X, Le TH, Parrish T, Erhard P. Retrospective estimation and correction of physiological fluctuation in functional magnetic resonance imaging. *Magn Reson Med* 1995;34:201-212.

94. Chuang K, Chen J. IMPACT: Image-based physiological artifact estimation and correction technique for functional MRI. *Magn Reson Med* 2001;46:344-353.
95. Zhao X, Bodurka J, Jesmanowicz A, Li S. B_0 -induced temporal variation in EPI images series due to disturbance of steady-state free precession. *Magn Reson Med* 2000;44:758-765.
96. Smith AM, Lewis BK, Ruttimann UE, Ye FQ, Sinnwell TM, Yang Y, Duyn JH, Frank JA. Investigation of low-frequency drift in fMRI signal. *Neuroimage* 1999;9:526-533.
97. Gopinath KS, Peck KK, Soltysik DA, Briggs RW. Similarities in the low frequency noise characteristics between the magnitude and phase time-series. *Proc Intl Soc Magn Reson Med* 2003;11:1890.
98. Gopinath KS, Peck KK, Soltysik DA, Briggs RW. Comparison of the low frequency noise characteristics between diseased and healthy brain regions. *Proc Intl Soc Magn Reson Med* 2003;11:1892.
99. Ward BD. Deconvolution analysis of fMRI time-series. AFNI documentation; 2003.
100. Neter J, Wasserman W, Kutner MH. *Applied linear statistical models*. Homewood:Irwin 1985.
101. Miller RG. *Simultaneous statistical inference*. New York: Springer-Verlag;1981.
102. Benjamini Y, Hochberg Y. Controlling the false discovery rate: A practical and powerful approach to multiple testing. *J R Stat Soc Ser B* 1995;57:289-300.
103. Genovese CR, Lazar NA, Nichols T. Thresholding of statistical maps in functional neuroimaging using the false discovery rate. *Neuroimage* 2002;15:870-878.
104. Ogawa S, Menon RS, Kim SG, Ugurbil K. On the characteristics of functional magnetic resonance imaging of the brain. *Annu Rev Biophys Biomol Struct* 1998;27:447-474.
105. McGonigle DJ, Howseman AM, Athwal BS, Friston KJ, Frackowiak RSJ, Holmes AP. Variability in fMRI: An examination of intersession differences. *Neuroimage* 2000;11:708-734.
106. Friston KJ, Holmes AP, Price CJ, Buchel C, Worsley KJ. Multisubject fMRI studies and conjunction analyses. *Neuroimage* 1999;10:385-396.
107. Metz CE, Shen JH, Wang PL, Kronman HB. *ROC analysis programs*. Chicago:University of Chicago 1978.

108. Constable RT, Skudlarski P, Gore JC. An ROC approach for evaluating functional brain MR imaging and postprocessing protocols. *Magn Reson Med* 1995;34:57-64.
109. Skudlarski P, Constable RT, Gore JC. ROC analysis of statistical methods used in functional MRI: individual subjects. *Neuroimage* 1999;9:311-329.
110. Le TH, Hu X. Methods for assessing accuracy and reliability in functional MRI. *NMR Biomed* 1997;10:160-164.
111. Genovese CR, Noll DC, Eddy WF. Estimating test-retest reliability in functional MR imaging I: statistical methodology. *Magn Reson Med* 1997;38:497-507.
112. Grootnik S, Hutton C, Ashburner J, Howseman AM, Josephs O, Rees G, Friston KJ, Turner R. Characterization and correction of interpolation effects in the realignment of fMRI time-series. *Neuroimage* 2000;11:49-57.
113. Jezzard P, Clare S. Sources of distortion in functional MRI data. *Hum Brain Mapp* 1999;8:80-85.
114. Noll DC. Reconstruction techniques for magnetic imaging. PhD thesis Paolo Alto: Stanford University;1991.
115. Glover GH, Lai S. Self-navigated spiral fMRI: Interleaving versus single-shot. *Magn Reson Med* 1998;39:361-368.
116. Ward HA, Riederer SJ, Jack CR. Real-time autoshimming for echo planar timecourse imaging. *Magn Reson Med* 2002;48:771-780.
117. Friston KJ, Williams S, Howard R, Frackowiak RSJ, Turner R. Movement-related effects in fMRI time-series. *Magn Reson Med* 1996;35:346-355.
118. Bullmore ET, Brammer MJ, Rebe-Hesketh S, Curtis VA, Morris RG, Williams SCR, Sharma T, McGuire PK. Methods for diagnosis and treatment of stimulus-correlated motion in generic brain activation studies using fMRI. *Hum Brain Mapp* 1999;7:38-48.
119. Thesen S, Heid O, Mueller E, Schad LR. Prospective acquisition correction for head motion with image-based tracking for real-time fMRI. *Magn Reson Med* 2000;44:457-465.
120. Ward HA, Riederer SJ, Grim RC, Ehman RL, Felmlee JP, Jack CR. Prospective multi-axial motion correction for fMRI. *Magn Reson Med* 2000;43:459-469.
121. Lee CC, Grim RC, Manduca A, Riederer SJ, Ehman RL, Felmlee JP, Jack CR. A prospective approach to correct for inter-image head motion in fMRI. *Magn Reson Med* 1998;39:234-243.

122. Hu X, Kim SG. Reduction of signal fluctuations in fMRI using navigator echoes. *Magn Reson Med* 1994;31:495-503.
123. Yetkin FZ, Haughton VM, Cox RW, Hyde JS, Birn RM, Wong EC, Prost R. Effects of motion outside the field of view on functional MR. *Am J Neuroradiol* 1996;17:1005-1009.
124. Birn RM, Bandettini PA, Cox RW, Jesmanowicz, A, Shaker R. Magnetic field changes in the human brain due to swallowing or speaking. *Magn Reson Med* 1998;40:55-60.
125. Birn RM, Bandettini PA, Cox RW, Shaker R. Event-related fMRI of tasks involving brief motion. *Hum Brain Mapp* 1999;7:106-114.
126. Salvador S, Brovelli A, Longo R. A simple fast technique for on-line fMRI data analysis. *Magn Reson Imag* 2002;20:207-213.
127. Barch DM, Sabb FW, Carter CS, Braver TS, Noll DC. Overt verbal responding during fMRI scanning: empirical investigations of problems and potential solutions. *Neuroimage* 1999;10:642-657.
128. Huang J, Carr T, Cao Y. Comparing cortical activations for silent and overt speech using event-related fMRI. *Hum Brain Mapp* 2001;15:39-53.
129. Gopinath KS, Peck KK, Soltysik DA, Crosson BA, and Briggs RW. A selective detrending method to reduce noise due to event-correlated motion in fMRI time-series for an event-related overt word generation paradigm. *Proc Intl Soc Magn Reson Med* 2003;11:388.
130. Gaiefsky ME, Crosson B, White KD, Peck KK, Moore AB, Wierenga C, Gopinath KS, Soltysik DA, Briggs R. Imaging overt language production in aphasia using FMRI. *Soc Neurosci* 2002;vol:pp
131. Maccotta L, Zacks JM, Buckner RL. Rapid self-paced event-related functional MRI: feasibility and implications of stimulus- versus response-locked timing.
132. de Zwart J, van Gelderen P, Kellman P, Chu R, Duyn J. Latency and duration of hemodynamic response correlate with anatomy. *Proc OHBM* 2003;9:657.
133. Press WH, Teukolsky SA, Vetterling WT, Flannery BP. *Numerical Recipes in C, the art of scientific computing*, New York: Cambridge University Press; 1992.
134. Gopinath KS, Briggs RW, Soltysik D, Himes N, Crosson BA. Reduction of noise associated with stimulus correlated motion in event related overt word production fMRI studies. *Proc Int. Soc Magn Reson Med* 2001;9:297

BIOGRAPHICAL SKETCH

Kaundinya Srinivasan Gopinath was born on “Valentine’s Day,” 1969. He had his early schooling in Jabalpur and Madras. He graduated from Ramnarain Ruia College, Bombay University, with a B.Sc. in physics. He subsequently attended the University of Poona and the Inter-University Center for Astronomy and Astrophysics, Poona, under a Universities Grants Commission Scholarship. After graduating in 1993 with a M. Sc. in physics and astrophysics he joined the Department of Physics, University of Florida. After graduating in 1998 with a MS in physics he joined the Department of Nuclear and Radiological Engineering, University of Florida. Currently he is a doctoral candidate in medical physics at the University of Florida.